HELSINGIN YLIOPISTO
HELSINGFORS UNIVERSITET
UNIVERSITY OF HELSINKI

Master`s thesis
Department
Subject

The lithogeochemistry of the Cu-rich disseminated ore and further geochemical characterization of the massive ore, Sakatti Cu-Ni-Co-PGE deposit, Central Lapland Greenstone Belt, Finland

Pelayo Barrón Francisco
Date 06/06/20

HELSINGIN YLIOPISTO
MATEMAATTIS-LUONNONTIETEELLINEN TIEDEKUNTA

PL 64 (Gustaf Hällströmin katu 2)
00014 Helsingin yliopisto

HELSINGIN YLIOPISTO
HELSINGFORS UNIVERSITET
UNIVERSITY OF HELSINKI

Tiedekunta/Osasto Fakultet/Sektion – Faculty Faculty of science	Laitos/Institution– Department Geoscience and geography	
Tekijä/Författare – Author Pelayo Barrón Francisco		
Työn nimi / Arbetets titel – Title The Lithogeochemistry of the Cu-rich disseminated ore and further geochemical characterization of the massive ore, Sakatti Cu-Ni-Co-PGE deposit, Central Lapland Greenstone Belt, Finland.		
Oppiaine /Läroämne – Subject Lithogeochemistry		
Työn laji/Arbetets art – Level Master thesis	Aika/Datum – Month and year 06/2020	Sivumäärä/ Sidoantal – Number of pages

Tiivistelmä/Referat – Abstract

Sakatti is one of the most significant magmatic Ni-Cu-PGE deposits discovered in the last decade. With a reported 44.4 Mt resource, is a polymetallic deposit with grades of: 1.90 % Cu, 0.96 % Ni, 1.40 g/t PGE; Anglo American ltd. report (2019).

Sakatti is located within the Early Proterozoic Central Lapland Greenstone Belt (CLGB), Finland. The deposit is hosted by three ultramafic magma–derived olivine cumulate bodies: Main body, North-East body and South-West body. Very distinctive ore types can be recognized according to several academic studies: **A)** Massive ore containing an average 3.04 % Ni and 7 % Cu and showing a wide range in Ni/Cu (average of 1.42) and Pt/Pd of 0.98 (Ahvenjärvi 2015); **B)** Stockwork ore that is extremely copper-rich containing an average 0.68 % Ni and 26.17 % Cu, with Ni/Cu of 0.03 and Pt/Pd of 0.85 (Fröhlich 2016); **C)** Disseminated ore, where sulfides form a wide halo around the massive and stockwork ores, again being highly copper-dominated containing an average 0.07 % Ni and 0.61 % Cu. Ni/Cu and Pt/Pd values for disseminated ore are 0.13 and 1.83 respectively. The aim of this study is to shed some light on the genesis of the Sakatti´s disseminated ore and the massive sulfides from the NE and SW bodies. The disseminated mineralization was studied more in depth. Moreover, a comparison with other major Ni-Cu-(PGE) magmatic deposits in the world was done.

Overall the disseminated ore seems to be dominated by a patchy texture with low connectivity but high wettability. Chalcopyrite is the predominant sulfide mineral and forms intergrowths with the texturally earlier pyrrhotite and pentlandite. These primary phases are widely altered to secondary phases like marcasite, millerite, violarite, pyrite, bornite, covellite and magnetite. Only a few platinum-group minerals (PGM) were found. They all are tellurides or bismuth-tellurides of which the merenskyite-moncheite-melonite series minerals are the most abundant.

The chemical composition of the disseminated ore revealed compositional and fractionation similarities with both the massive and stockwork ores. When recalculated to 100 % sulfides and normalized to mantle values, the disseminated ore showed a moderate content in Ni, Co, IPGE and Rh close to the massive mineralization, and a higher enrichment in PPGE, Au and Cu with similar evolution patterns as the stockwork vein sulfides. This led to a fractionation path of the disseminated sulfide phase that seemed to be a mixture of the other two main ore types. Thus, it is suggested that the disseminated ore is formed by a combination of monosulfide solid solution (MSS) and intermediate solid solution (ISS), which originated from a sulfide melt genetically linked to the one that gave rise to the massive and stockwork ores. The massive sulfides from the NE and SW bodies show compositional similarities with the massive ore from the Main body that suggest a share origin and genesis. The Oktabr'sky, Noril'sk-Talnakh, disseminated ore, when normalized to mantle values, shows similar Ni, Co, PGE, Au and Cu distribution as the Sakatti´s disseminated sulfides. Moreover, the Oktabr'sky deposit seems to have similar S/Se vs Pt+Pd evolution trend to the one from Sakatti deposit.

Avainsanat – Nyckelord – Keywords

Säilytyspaikka – Förvaringställe – Where deposited

Muita tietoja – Övriga uppgifter – Additional information

CONTENTS

1. INTRODUCTION

1.1. The Sakatti Deposit

The Sakatti Cu-Ni-PGE deposit is one of only a handful of significant Ni-Cu-PGE magmatic deposits discovered globally in the past decade (Brownscombe et al. 2015). As implied by the grades reported for its 44.4 Mt mineral resource (Measured + Indicated + Inferred), 1.90 % Cu, 0.96 % Ni, 1.40 g/t PGE (Anglo American ltd. report, 2019), it seems to be unusually copper rich, considering that it is hosted by ultramafic cumulates. It is located 16 km NNE of the municipality of Sodankylä and halfway between Sodankylä and the active Kevitsa Ni-Cu-(PGE) mine (Figure 1). The major ore types of Sakatti deposit are disseminated, massive and stockwork ores. The deposit is hosted by a tubular conduit-shaped olivine cumulate main body and two smaller satellite bodies. There is no natural outcrop of the cumulates since Sakatti is completely covered by the Viiankiaapa swamp (Figure 1). The sulfide mineralization is generally Cu-dominated; however, a transition to more Ni-rich sulfide mineralization has been observed towards the deeper parts of the deposit (Brownscombe et al. 2013, Brownscombe et al. 2015, Halkoaho 2014).

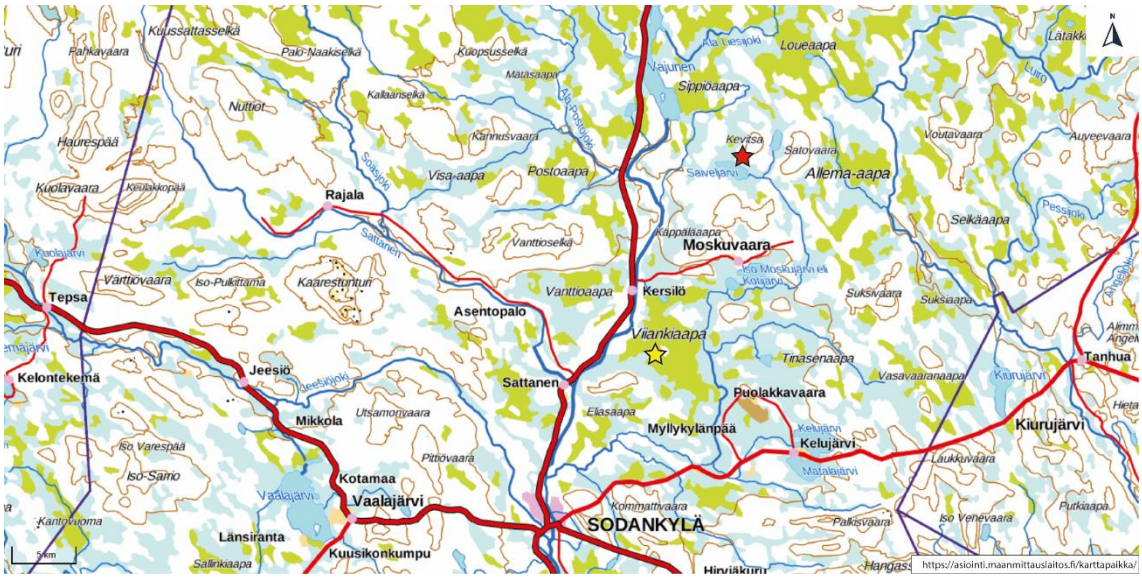

Figure 1. Geographical location of the Sakatti deposit marked in yellow. Kevitsa mine marked in red. Extracted from the National Land Survey of Finland (NLS)

1.1.1. Discovery of the Sakatti deposit

Exploration work across Fennoscandia was started by Anglo American plc in 2002. The first stages involved the use of the aeromagnetic and frequency electromagnetic (AMFEM) dataset previously produced by the Geological Survey of Finland (GTK) (Brownscombe et al. 2015). After the initial selection of several targets, of which Sakatti was target number 8 (MOS8, Coppard 2014), ground geophysical surveys and soil geochemistry were applied. With the help of base of till (BOT) geochemistry, a coherent Ni-Cu-PGE geochemical anomaly was discovered in the eastern section of the Sakatti target. Consequently, three exploration holes were drilled, of which hole 06MOS08003 yielded short intervals with high Cu-PGE-Au tenors but minor Ni. This led to downgrade of the Sakatti target in 2006, and the end of all exploration (Coppard 2014). Nevertheless, in 2007 Anglo American reviewed the exploration results, and consequently decided to carry out a detailed BOT geochemistry sampling program. This produced promising results (up to 0.70 wt. % Cu, 0.56 wt. % Ni, 0.74 g/t Pt in till samples) (Brownscombe et al. 2015, Coppard 2014). Encouraged by these results, The study of the Sakatti project was continued. In 2008, the discovery hole 09MOS08007 was drilled and disseminated and vein-related mineralization was discovered. In 2009, a significant mineralization was discovered by drill hole 09MOS08013 with an intersection of 1.01 wt. % Cu, 0.23 wt. % Ni, 0.43 g/t Pt, 0.24 g/t Pd and 0.29 g/t Au (Coppard 2014). A later airborne survey highlighted the two satellite cumulate bodies (Brownscombe et al. 2015).

1.2. Geological setting

To enable a comprehensive understanding of the Sakatti deposit, a geological setting overview from the regional to local scale will be presented in the following section.

1.2.1. Finnish regional geology

The Finnish bedrock belongs to the East European Precambrian craton, which extends to north-western parts of Russia and northern and eastern Europe (Lehtinen et al. 2005). Precambrian crystalline bedrock only outcrops in the northern and south-western parts of the craton which forms the Fennoscandian Shield (Lehtinen et al. 2005). The Fennoscandian Shield covers Finland, Sweden, Norway and North-western Russia

(Lehtinen et al. 2005, Maier et al. 2015). A geological map showing the main bedrock units in the eastern part of the Fennoscandian Shield is in Figure 2 and a general description of the principal units is provided below.

The Precambrian rocks in the central and eastern parts of the Fennoscandian Shield can be divided into three major crustal units: the Archean basement, the Paleoproterozoic sedimentary-volcanic cover and the Svecofennian orogenic belt (Lehtinen et al. 2005, Maier et al. 2015, Weihed et al. 2005). However, considering the stratigraphic level in which the Sakatti deposit is emplaced, the focus of this study will lie on the Archean and Paleoproterozoic rocks of the Fennoscandian Shield.

The Archean basement was formed in the northern and eastern parts of the shield from approximately 3.5 to 2.5 Ga and has been subdivided into the Kola and Karelian craton (Figure 2a). The majority of the Finnish Archean basement belongs to the Karelian craton, comprising a granitoid-greenstone terrane with a complex tectono-magmatic history (Lehtinen et al. 2005, Maier et al. 2015). The Central Lapland Greenstone Belt (CLGB), within which the Sakatti deposit is hosted, was formed on top of the Karelian craton (Makkonen et al. 2017) (Figure 2b).

The Paleoproterozoic sedimentary-volcanic cover (Figure 2b) was deposited on top of the Archean basement, and its age ranges from 2.5 to 1.9 Ga (Lehtinen et al. 2005, Maier et al. 2015). An intense magmatism occurred during the deposition of this unit and is evidenced by several generations of mafic dyke swarms in the Archean basement (Vuollo and Huhma, 2005). Many layered intrusions in Finland are dated 2.4 Ga. During the period from 2.2. to 1.97 Ga, several extensional phases occurred, leading to further large mafic intrusions and dyke swarms (e.g. Kevitsa at 2.05 Ga) (Vuollo and Huhma, 2005). Moreover, this period is also characterized by intense weathering that produced large amounts of quartz sands and also by volcanic activity manifested as lava flows (Lehtinen et al. 2005).

1.2.2. Central Lapland Greenstone Belt (CLGB)

With an area of 100 by 200 km the CLGB runs in SE-NW direction in northern Finland, crossing to Norway and Russia (Figure 3)(Hanski and Huhma, 2005). This greenstone

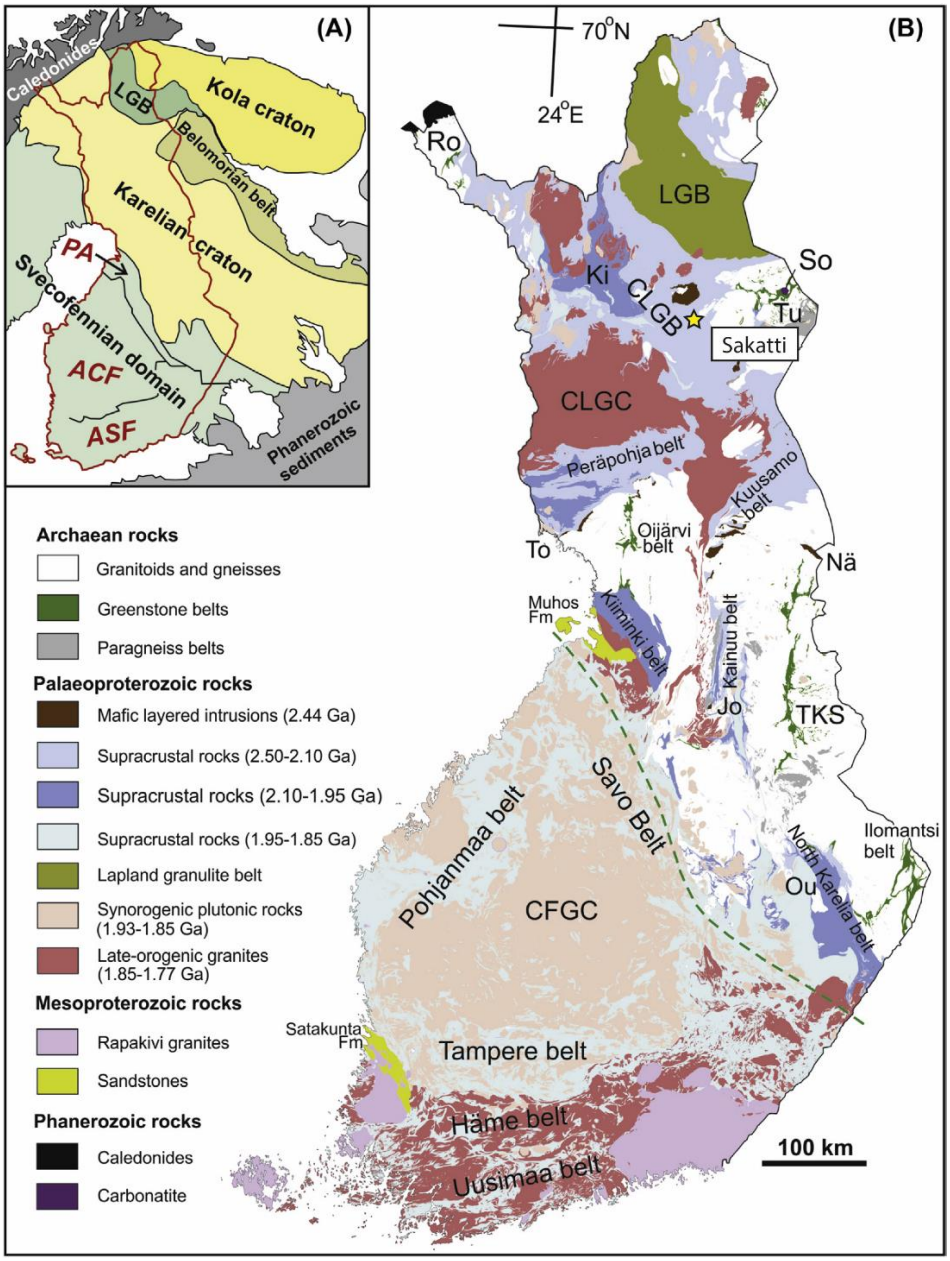

Figure 2. Finnish regional geological setting. (a) Main units that form the eastern side of the Fennoscandian shield. (b) Geological map of Finland that comprises the main lithostratigraphic units, belts and complexes. The Sakatti deposit appears marked in yellow star.
Abbreviations: LGB = Lapland granulite belt, CLGB = Central Lapland greenstone belt, CLGC = Central Lapland granulite belt, Central Finland granitoid complex. PA = Primitive arc complex of central Finland, ACF = Accretionary arc complex of central and western Finland, ASF = Accretionary arc complex of southern Finland. Jo = Jormua ophiolite, Ki = Kittilä greenstone complex, Nä = Näränkävaara, Ou = Outokumpu ophiolite, Ro = Rommaeno complex, So = Sokli carbonatite, TKS = Tipasjärvi-Kuhmo Suomussalmi belt, To = Tornio, Tu = Tulppio. Modified after Maier et al. (2015).

belt is delimited on the north by the Lapland Granulite Belt (LGB), on the south and south-west by the Central Lapland Granitoid Complex (CLGC). In the west and east, the CLGB is confined by Archean granite-gneiss terrains. The CLGB started forming ~2.45 Ga ago with the eruption of rhyolitic and komatiitic lavas on top of the Archean basement and endedat ~1.88 Ga ago with the sedimentation of coarse-clastic, molasse-type sediments of synorogenic plutonism. The degree of metamorphism ranges from greenschist facies in the central areas and increases to amphibolite facies towards the margins of the belt, mainly due to the influence of the Svecofennian orogeny at 1.91 – 1.81 Ga (Simonen 1971).

The Central Lapland Greenstone Belt has been divided by Lehtonen (1998) into the following seven lithostratigraphic groups (Figure 4) ranging from oldest to the youngest: Salla Group, Onkamo Group, Sodankylä Group, Savukoski Group, Kittilä Group, Lainio Group and Kumpu Group.

The Salla and Onkamo groups formed during the intracratonic rifting of the Archean basement ~2.5 – 2.4 Ga ago. These groups are characterized by shallow water volcanics that range in composition from komatiitic to rhyolitic with variable degrees of crustal contamination. Approximately 2.44 Ga ago, extensive mafic plutonism occurred, giving rise to several well-known layered intrusions like Kemi or Mustavaara (Hanski and Huhma, 2005).

The Sodankylä group deposited on top of the Onkamo group > 2.2 Ga ago within a cratonic or craton margin setting. It is mainly comprised of quartzites and minor mafic to felsic metavolcanics.

The Savukoski group formed between 2.2 and 2.0 Ga ago during the deepening of the depositional basin and is characterized by fine-grained sediments and mafic to ultramafic volcanic rocks. Within this group, the first sulfide and graphite-bearing black schists in the CLGB were deposited (Hanski and Huhma, 2005, Lehtonen 1998). These schists are overlain by komatiitic and picritic flows. The source of these magmas is thought to have originated deep in the mantle (Lehtonen 1998). During the deposition of the Savukoski

group, several mafic intrusions were emplaced with an age of 2.05 Ga, including the Kevitsa intrusion (Figure 1) (Rastas et al. 2001).

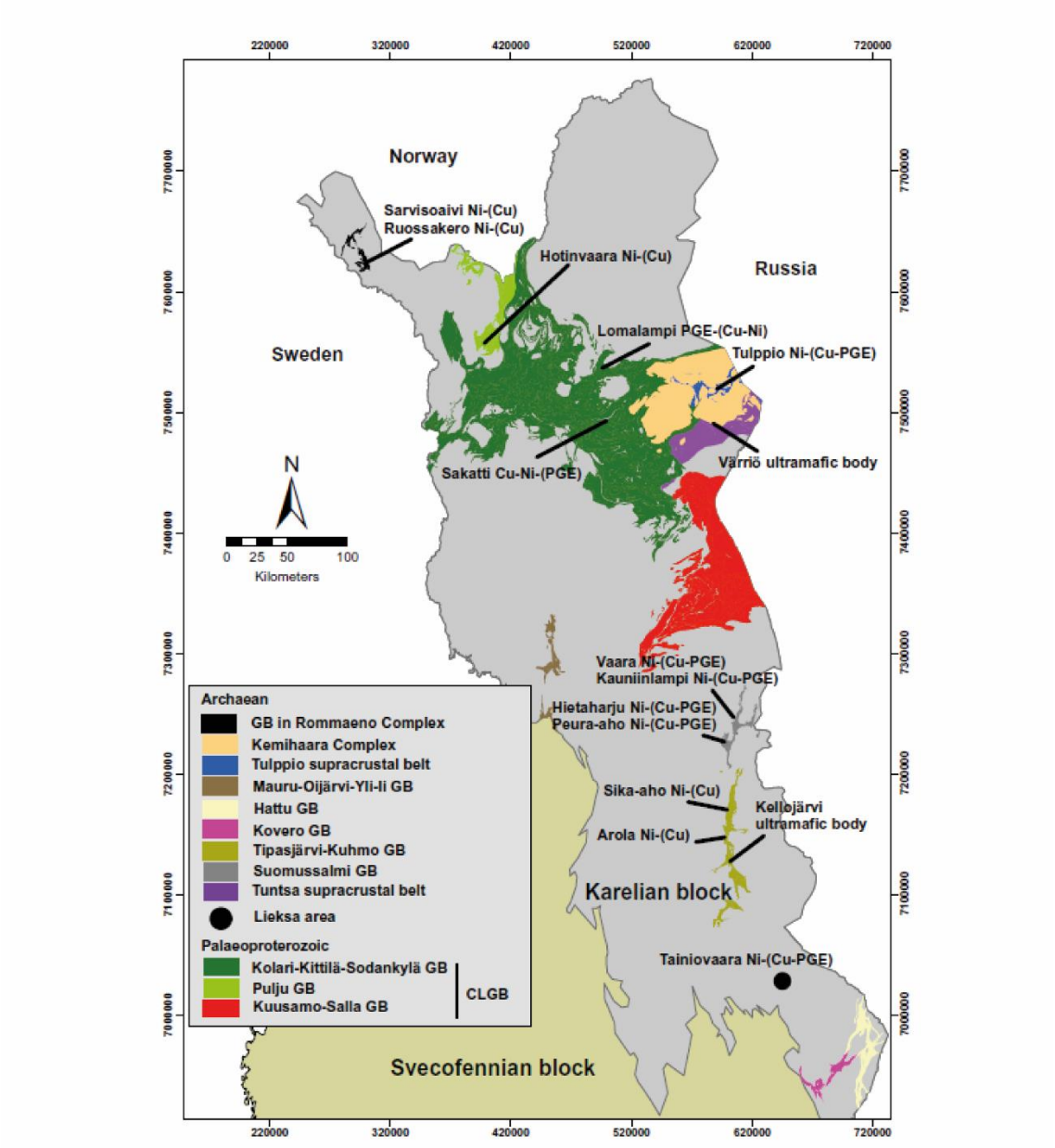

Figure 3. Most significant komatiite-bearing Archean and Paleoproterozoic greenstone belts and Ni-Cu-(PGE) deposits in northern and eastern Finland. Abbreviations: GB = Greenstone belt, CLGB = Central Lapland greenstone belt. After Makkonen et al. (2017)

The Kittilä group originated due to the opening of an oceanic basin c. 2.0 Ga ago, and it comprises two volcanogenic units separated by a banded iron formation (BIF) and overlain by a pelitic metasedimentary unit. The geochemistry of these volcanic units denotes a progression from a continental to oceanic geotectonic setting. Geophysical studies suggest a maximum thickness of 6 km for this group. During the Svecokarelian

orogeny (~1.89 Ga ago) the Kittilä group was obducted onto older formations, and the boundary between them is marked by serpentine lenses of an ophiolitic nature.

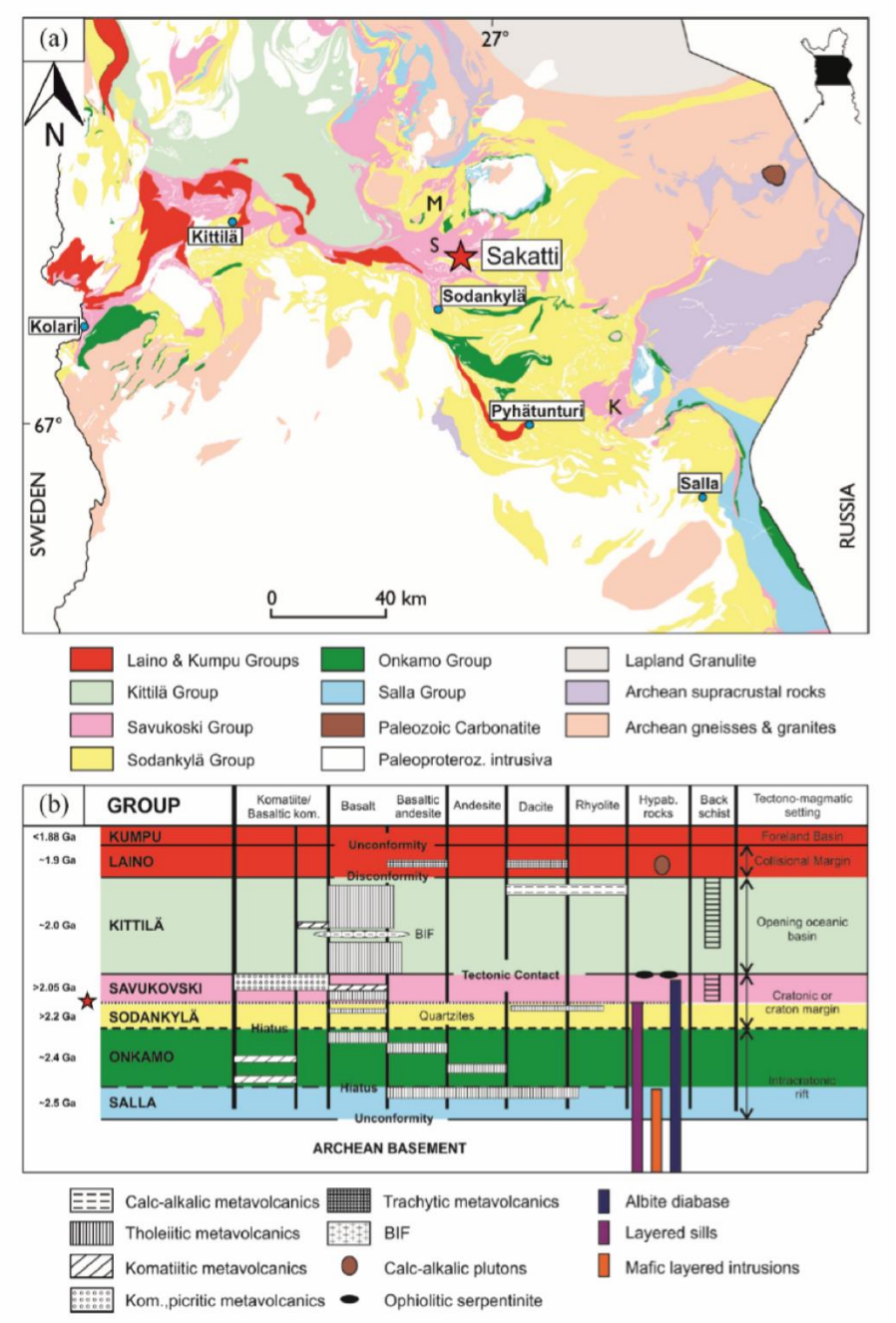

Figure 4. (a) Geological map with the lithostratigraphic units of central Finnish Lapland with the Sakatti deposit marked with a red star. Modified after Hanski & Huhma (2005). (b) Stratigraphhy of the Central Lapland Greenstone Belt. Stratigraphic position of the Sakatti deposit is marked with a red star. Modified after Lehtonen et al. (1998).

The Lainio group was deposited on top of the Kittilä group. It is characterized by mafic to felsic rocks and arkosic sediments. When the main deformation phase ended, molasse-

type sediments were deposited on the Lainio group in a foreland basin setting giving rise to the Kumpu group (Hanski and Huhma, 2005, Lehtonen 1998).

The CLGB is characterized by several mineralization events which resulted in formation of magmatic Ni-Cu-PGE, iron-oxide-copper-gold (IOCG), volcanic-hosted massive sulfide (VMS) and orogenic gold deposits. Nearly all of these mineralization events occurred between 2.06 and 1.78 Ga ago, which indicates a period of rapid accretion of island arcs and several continent-microcontinent collisions leading to a succession of intense and short lived orogenies. However, the Ni-Cu-PGE deposits, developed in connection to mafic volcanism in rift basins that occurred between 2.2 Ga and 2.05 Ga ago (Weihed et al. 2005). The Sakatti likely deposited during this time interval (Brownscombe et al. 2015, Halkoaho 2014). The IOCG and VMS and orogenic gold deposits are classified as the youngest within the greenstone belt, between 1.97 and 1.79 Ga old. The IOCG deposits are linked to continental arcs or magmatism inboard of active arcs. The VMS formed during basin inversion and accretion.

1.2.3. Geology of the Sakatti deposit

The Sakatti deposit consists of three mineralized bodies: The Main body, being the largest, and the NE and SW satellite bodies, named according to their geographical position in relation to the Main body (Figure 5). The sulfide ores are predominantly hosted by peridotites (Brownscombe et al. 2015), which emplaced approximately along the contact between the Sodankylä and Savukoski groups (Figure 4). These ultramafic rocks are spatially associated to mafic volcanic rocks of the Ruukinvaara formation (Sodankylä group), meta-silt stone, meta-arkose and skarn of the Orajärvi formation (Sodankylä group) and meta-pelites of the Matarakoski formation (Savukoski group).

With the help of constraints from regional geology and drill core logging data, a lithological model of the Sakatti deposit was created, which is defined by a stratigraphic succession that moderately dips and decreases in age towards the north. The base of this sequence is marked by a major thrust fault that separates the deposit in the hanging wall from the older Sodankylä group in the foot wall. Thus, a general description of each of the rock units hosting the Sakatti deposit will be given based on the work of

Brownscombe et al. 2013, Brownscombe et al. 2015, Halkoaho 2014 and Impala 2017. An oblique view of the bedrock lithology model for the Main and NE bodies is provided in Figure 6a below. A typical cross-section through the Main body is presented in Figure 6b.

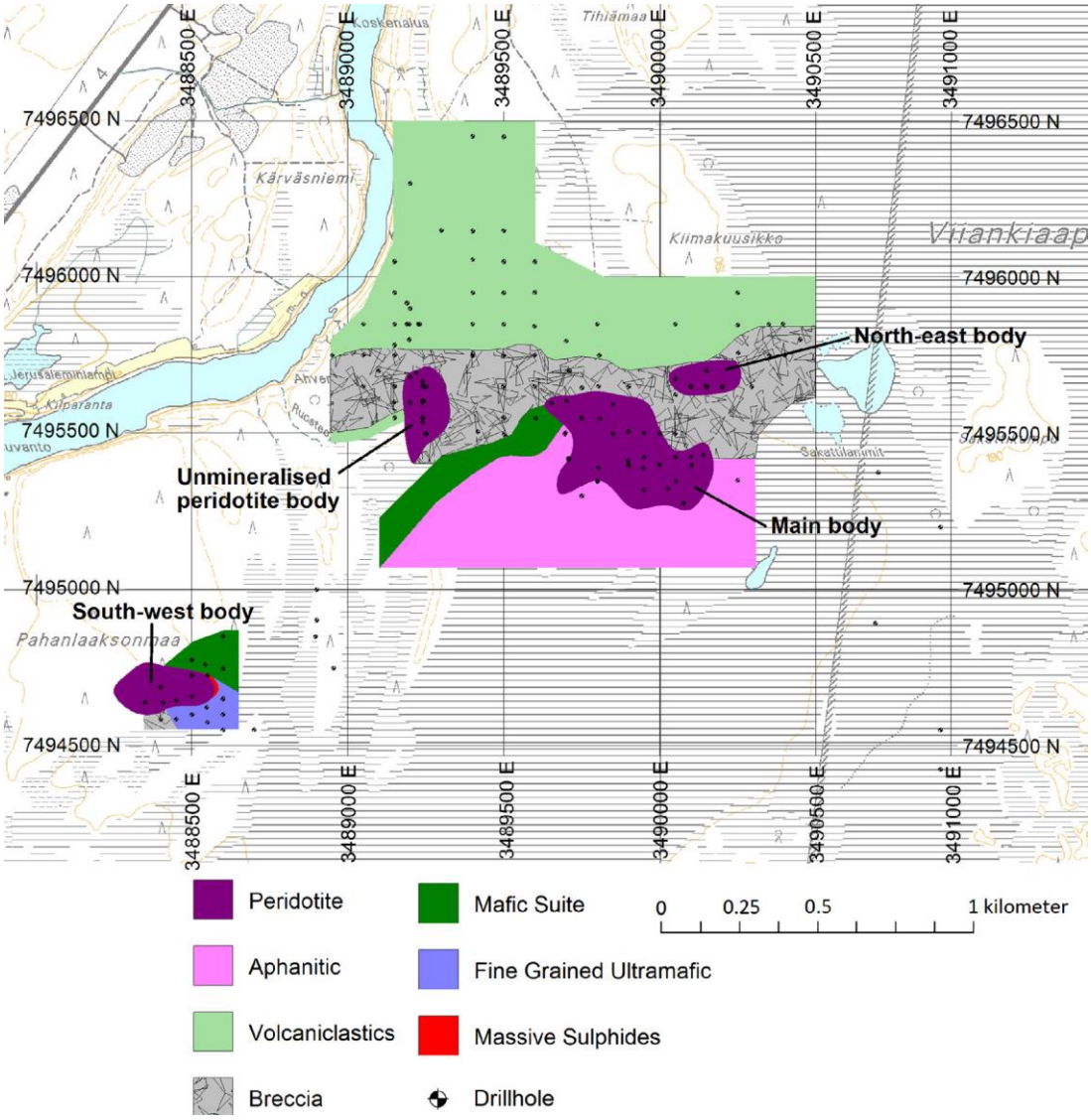

Figure 5. Simplified map of the studied area with the locations of the Main body, NE body and SW body. Horizontal lines illustrate wetland areas. After Brownscombe et al. 2015.

1.2.3.1. Peridotite

The peridotite unit (olivine cumulates) hosts the bulk of the Sakatti mineralization. With their complex geometry, these cumulate rocks define several channel-like bodies that seem to be connected, giving rise to a single large unit that is open along strike to the east

and west and has approximately 1500 metres of strike extent and 1000 metres of down dip extent. The peridotite dips roughly 50º towards the north, but due to its complexity, this is difficult to estimate accurately. Nonetheless, the peridotite unit seems to be conformable with the overall volcano-sedimentary sequence (Brownscombe et al. 2015). The combination of whole rock geochemistry and the textural study carried out by Halkoaho (2014) suggests that this unit has a komatiitic origin. This contrasts with the interpretation by Brownscombe et al. (2013) who classified peridotite as shallow level conduit-like intrusion.

1.2.3.2. Dunite

The dunite unit (olivine adcumulate) lies beneath the peridotite unit and seems to represent the base of the peridotite body (Brownscombe et al. 2015). It has a fairly lenticular shape and a thickness of 50 to 110 metres, and it exhibits a WSW trend and a 35º dip (Figure 6b).

1.2.3.4. Aphanite

The so-called aphanitic unit is a fine-grained ultramafic rock that has been interpreted to be coeval to the peridotite unit (Brownscombe et al. 2015). It occurs in the hanging wall and footwall of the main peridotite body, but always below the mafic suite and breccia lithologies. The aphanite unit exhibits a thickness of 200 to 400 metres, an E-W strike and a roughly 60º northward dip. This lithology is broadly unmineralized, but in the south western part of the Main body (Brownscombe et al. 2015).

1.2.3.5. Mafic suite

The mafic suite lithology occurs mainly in the immediate hanging wall of the Main body peridotite and in the hanging wall of the NE-body (Brownscombe et al. 2015). Petrographic analysis by Halkoaho (2014) suggests a similar composition of these two sections.

1.2.3.6. Pyroxenite

Pyroxenitic rocks seem to be common although they represent a small volume. They occur as thin layers and/or inclusions within the peridotite unit (Brownscombe et al. 2015). The grain size varies from fine to coarse, and different types of mineralization within pyroxenite are common, ranging from disseminated to massive parts.

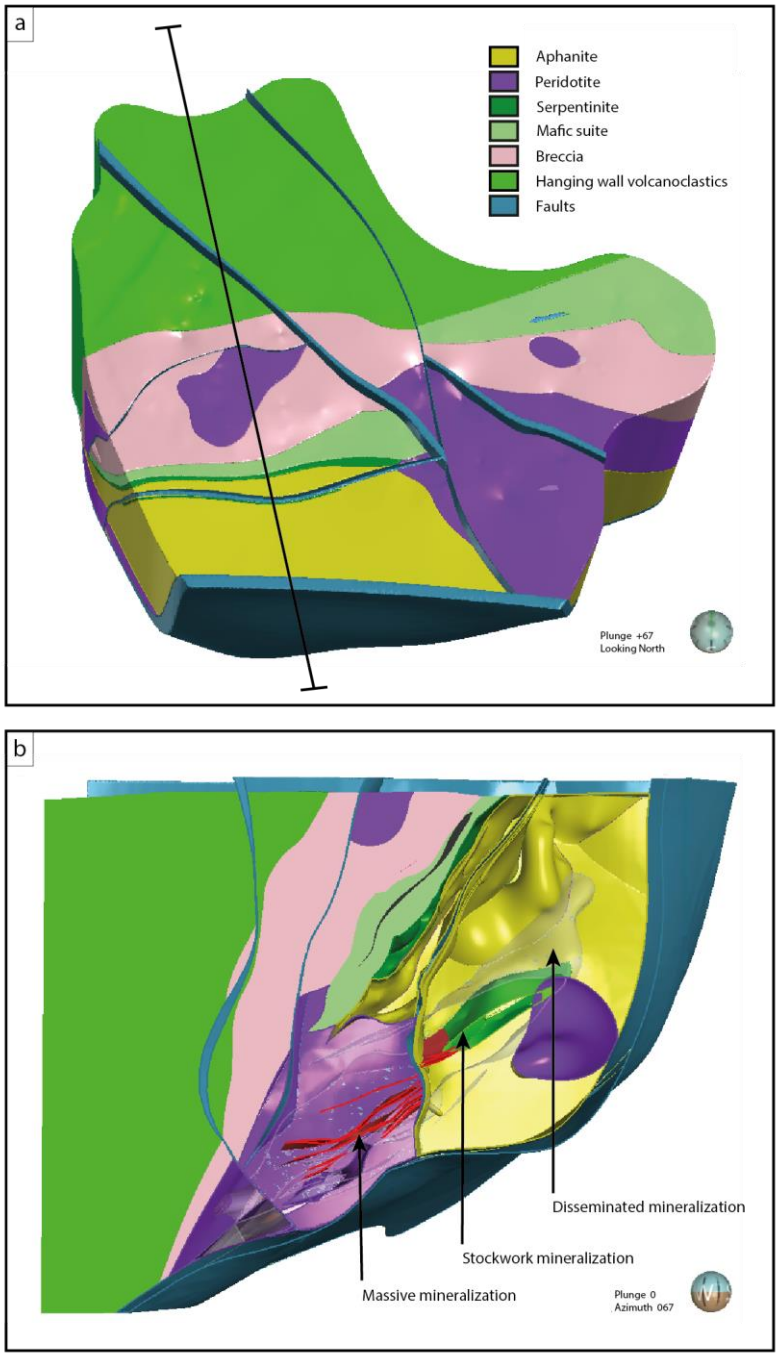

Figure 6. Bedrock lithostratigraphy of the Sakatti deposit Main and NE bodies. (a) Oblique plan view with location of cross section. (b) Main body cross section. After Sakatti 3D model (2017).

1.2.3.7. Gabbro

Gabbroic rocks with a thickness between 3 and 6 metres and a dip of 65 degrees northward occur as dykes within or near the margins of the western mafic suite unit (Brownscombe et al. 2015).

1.2.3.9. Breccia

The unit known as breccia does not represent a tectonic breccia but more like a strongly hematised angular to rounded polymictic breccia/conglomerate with clasts from the stratigraphically older Sodankylä group within a carbonate matrix (Brownscombe et al. 2015). It has an approximate E-W trend and a 70º northward dip and is 100 to 300 metres thick.

1.2.3.11. Hanging wall volcanoclastic sequence

Representing the uppermost sequence intersected in the Main body drilling (Brownscombe et al. 2015), the hanging wall volcanoclastic unit exhibits a thickness of about 500 metres and is open to the north. The lower contact, linked to the mafic suite and breccia, trends E-W and has a dip of 80º towards the north.

1.2.4. Mineralization

Based on the textures, sulfide content and sulfide mineralogy observed during core logging, the mineralization in the Sakatti deposit has been divided into 3 main categories: 1) Massive sulfides, 2) stockwork sulfides, 3) disseminated sulfides (Figure 7) (Brownscombe et al. 2015). This study will focus on the disseminated mineralization but also cover the geochemical characteristics of the massive sulfides from the NE and SW bodies.

1.2.4.1. *Massive sulfides*

The massive sulfide mineralization (Figure 7 and 8) brings the most value to the Sakatti project and is predominantly hosted by the peridotite unit (Ahvenjärvi 2015, Brownscombe et al. 2015). This mineralization typically occurs as massive lenses with a similar orientation as the one from the peridotite and dunite units. The biggest concentration of Ni of the deposit is located within the massive sulfides (Ahvenjärvi 2015, Brownscombe et al. 2015). These massive lenses have a thickness that varies from 1 to 20 metres as a package and are persistent for 600 metres along strike and 900 metres down dip. Individual lenses can be traced for up to 400 metres and have sharp contacts.

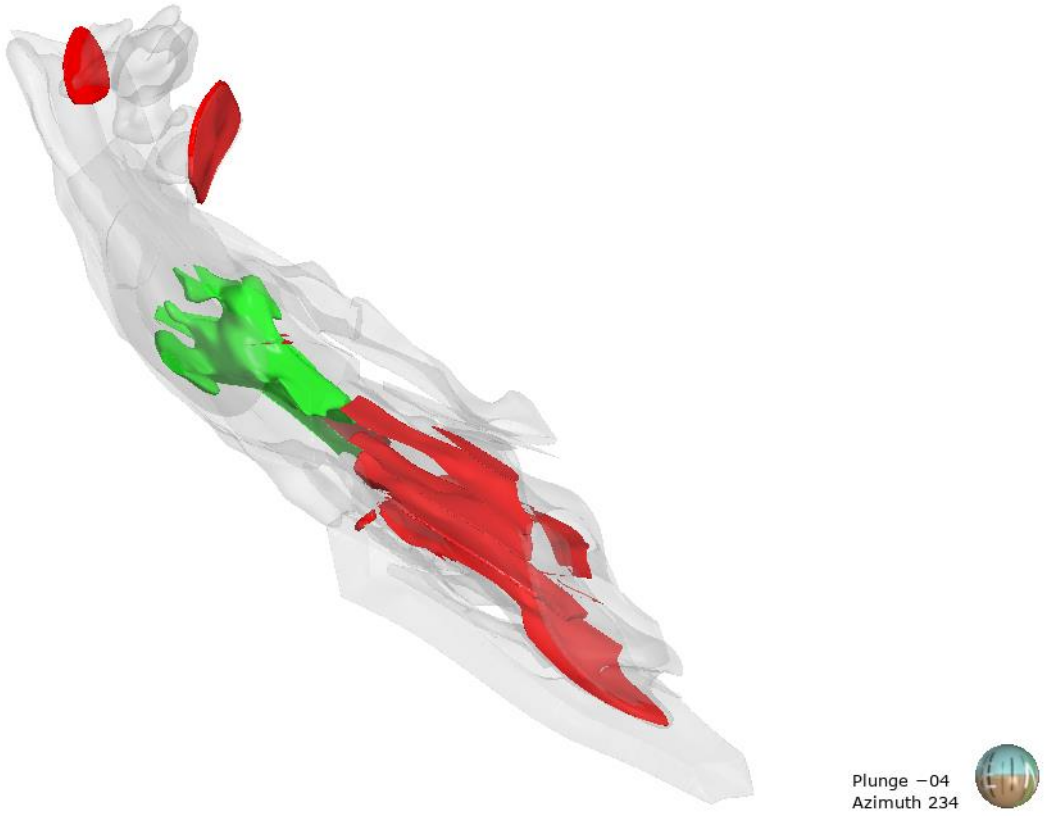

Figure 7. Cross section of the Sakatti Main body showing the three main mineralizations. Massive sulfides are marked in red, stockwork vein sulfides in green, and disseminated sulfides in grey. After Sakatti 3D model (2017).

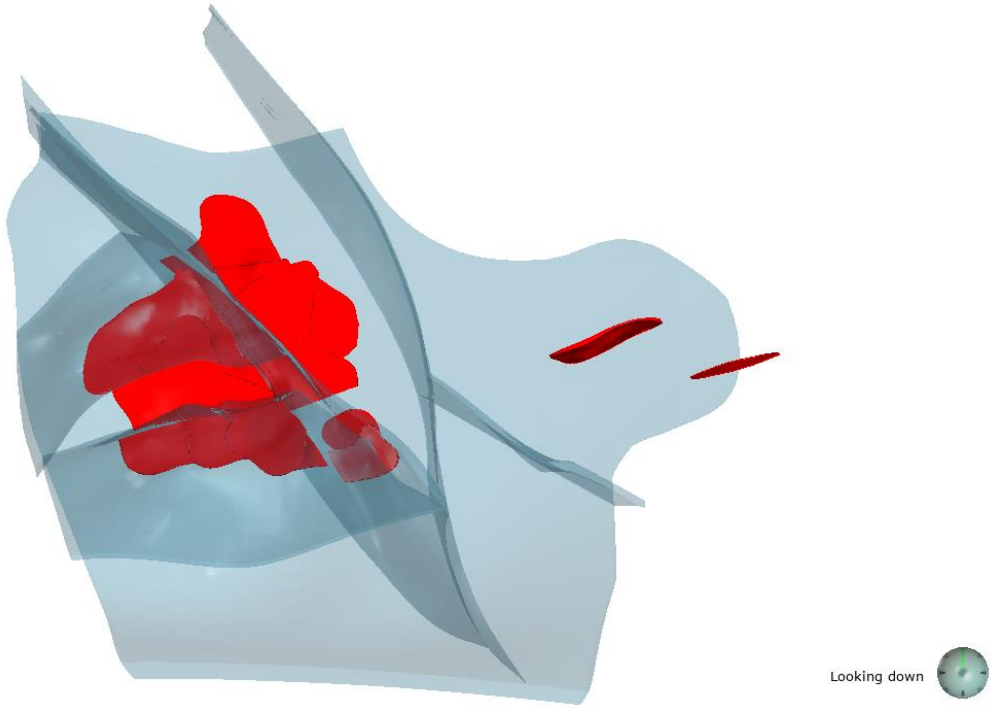

Figure 8. Plan view of massive sulfide lenses, in red, of the Main body and NE body. Fault system in blue. After Sakatti 3D model (2017).

1.2.4.4 Stockwork sulfides

Cu-rich stockwork vein mineralization (Figure 7 and 9) is characterized by chalcopyrite-dominated veins (Brownscombe et al. 2015, Fröhlich 2016). This mineralization has considerably lower content in Ni, Co, IPGE and Rh than the massive and disseminated sulfides (Fröhlich 2016). The PPGE, Au and Cu values of the stockwork sulfides are higher than in the massive sulfides, however, lower than the values in the disseminated mineralization, but Cu (Ahvenjärvi 2015, Brownscombe et al. 2015, Fröhlich 2016).

1.2.4.5. Disseminated mineralization

The disseminated mineralization is chalcopyrite dominated, which indicates an unusual high Cu content (Ahvenjärvi 2015, Brownscombe et al. 2015). This mineralization appears surrounding the massive and stockwork sulfides and seems to also have a similar dip and dip direction (Brownscombe et al. 2015) (Figure 7 and 10). Disseminated sulfides appear mainly hosted within the peridotite units in the Main and NE bodies, however, it has also been observed in the dunite and aphanite units (Brownscombe et al. 2015). The

current understanding approximately divides the bulk of the disseminated mineralization in the Main body into three sections (Anglo American ltd. 2017): (a) The lower body. Mainly hosted by the dunite. (b) The central body, is the biggest and is hosted by the peridotite unit just above the lower body. (c) The upper body. Located just above the central body.

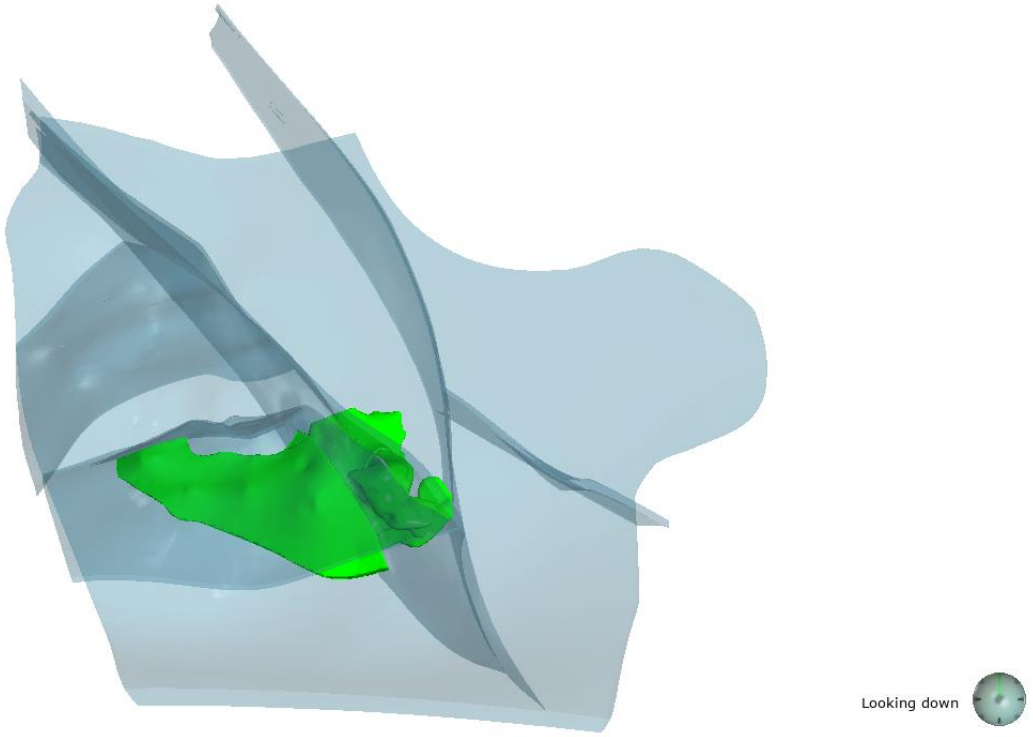

Figure 9. Plan view of the stockwork sulfide lenses, in green. Fault system in blue. After Sakatti 3D model (2017).

1.3. Classification of Ni-Cu-(PGE) deposits

Magmatic sulfide deposits can be found within different types of igneous rocks; however, they can be broadly categorized into sulfide-rich and sulfide-poor deposits (Barnes et al. 2017).

(a) Sulfide-rich deposits, exploited primarily for Ni and Cu. These can be sulfide-rich accumulations in small mafic or mafic-ultramafic intrusions sometimes interpreted as magma conduits (Lightfoot and Evans-Lamswood, 2015) (e.g. Voisey's Bay, Jinchuan, Norilsk-Talnakh). Also, accumulations of sulfide in komatiites (Kambalda, Perseverance, etc.) or in ferropicrites such as in the Pechenga deposit.

Finally, sulfide accumulation related to a meteorite impact, of which the unique example is Sudbury.

(b) Sulfide-poor deposits (typically less than 5 % sulfide), where the dominant value is in the platinum-group elements (PGE) and gold. Stratiform accumulations of disseminated sulfides within layered mafic-ultramafic intrusions, including PGE-rich reefs (e.g. Merensky Reef and Platereef, Bushveld Complex) (Holwell and McDonald, 2006, Mungall and Naldrett, 2008).

The Sakatti deposit belongs to the sulfide-rich group (**a**) displaying features of high sulfide content with accompanying Ni and Cu mineralization (Brownscombe et al. 2013, Brownscombe et al. 2015).

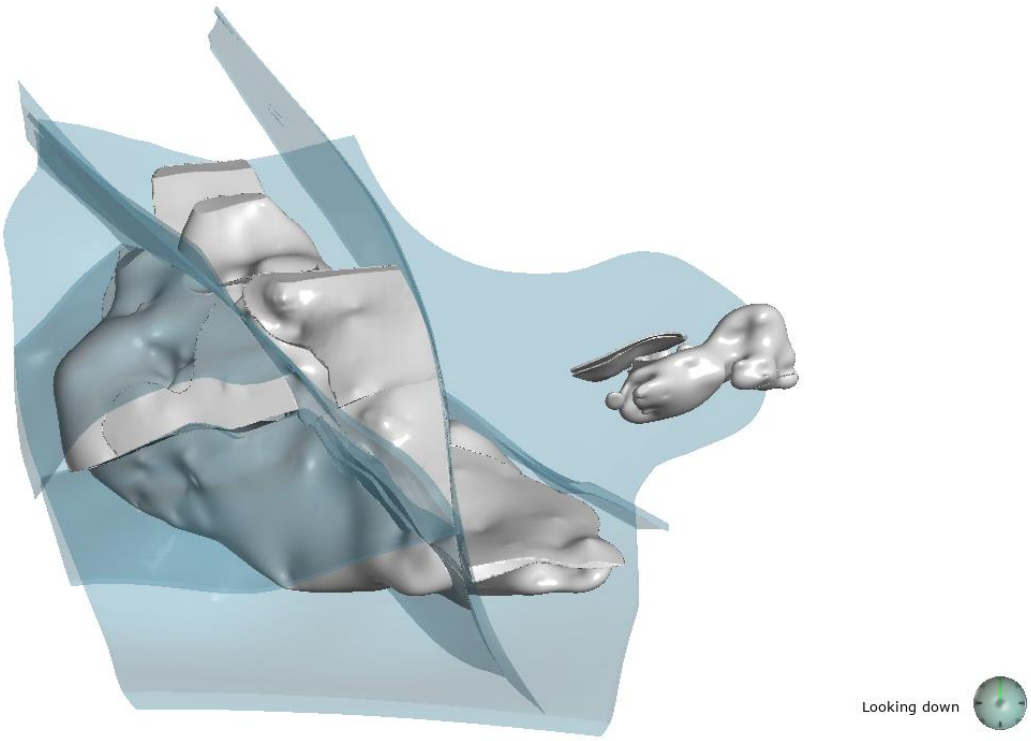

Figure 10. Plan view of the disseminated sulfide lenses, in grey, of the Main body and NE body. Fault system in blue. After Sakatti 3D model (2017).

Ni-sulfide deposits have also been classified based on their Ni/Cu ratios (Barnes and Lightfoot, 2005). This categorization gives rise to two broad classes (Class 1 and Class 2), which are further subdivided based on their geological association and rock type.

Class 1 deposits seem to be hosted by gabbronorite and troctolite except in the Jinchuan deposit, which is hosted by peridotites. They typically show Ni/Cu ratios ranging from

0.8 to 2.5 (Table 1). Moreover, the Ni content of 100 percent sulfides is between 1-6 wt. % Ni. Class 1 deposits have dived into six groups:

(i) Sulfide ores at the margins of an igneous complex as the result of an impact melt. Within this geological setting only one mining camp is known, the Sudbury basin.

(ii) Deposits that are typically found at the base of sills and margins of largely gabbroic dikes. These igneous bodies are thought to be linked to continental rifts and represent the feeder conduits of major intrusions or continental flood basalts. Known deposits within this subclass are the Norilsk-Talnakh and Jinchuan deposits. However, in the case of Jinchuan, the host rock is a peridotite, which has given rise to the idea that the sulfides got emplaced along an olivine crystal mush (De Waal et al. 2004).

(iii) Found in feeders in a rifted back arc. There are no known sulfide ores within this group (Barnes and Lightfoot, 2005).

(iv) Sulfides linked to a troctolite dike and intrusion that were emplaced in a suture zone, after a collision event. This subclass includes the Voisey's Bay deposit.

(v) Small intrusions emplaced in thick crust. No known Ni-sulfide ores are found within this type.

(vi) Ores associated with highly deformed gabronorites, about which too little published information can be found to establish a link with a geological setting. Two examples are the Pikwe and Vammala sulfide deposits.

Class 2 deposits are hosted by ultramafic rocks. The Ni/Cu ratios in this case tend to be higher than 3 (Table 1), and the Ni content in 100 percent sulfides is in the 6 to 18 percent range. This class can be further subdivided into deposits linked to komatiites and deposits associated with picrites. Komatiite group deposits occur in greenstone belts such as the Norsemen-Wiluma and the Cross-Forrestania in Western Australia and in the Cape Smith deposits. Picritic subclass includes deposits such as Pechenga and Kabanga. Overall, the

geological setting for these deposits linked to ultramafic rocks seems to be a rift zone (Barnes et al. 2001, Barnes et al. 1997).

Table 1. Estimates of Historic Production, Present Reserves, and Resources for Ni Sulfide Deposits and Camps. Modified after Barnes & Lightfoot (2005).

Minig camp	Location	Size (mt)	Ni (wt. %)	Cu (wt. %)	Contained Ni (t)	% of total resources	Deposit type
Sudbury	Ontario, Canada	1648	1.2	1.03	1977600	30.34	1
Noril'sk-Talnakh	Russia	1309.3	1.77	3.57	23174610	35.55	1
Jinchuan	China	515	1.06	0.67	545900	8.37	1
Voisey's Bay	Labrador, Canada	136.7	1.59	0.85	2173530	3.33	1
Selebi-Pikwe	Bostwana	110	0.75	1	82500	1.27	1
Shebandowan	Ontario, Canada	15	1.5	1	22500	0.35	1
Lynn Lake	Manitoba, Canada	20	1.02	0.535	20400	0.31	1
Monchegorsk	Russia	47	0.7	0.4	32900	0.5	1
Black Swan	Western Australia	10.9	3.43	0.15	373870	0.57	2
Forrestania Belt	Western Australia	14	1.3	0.06	18200	0.28	2
Honeymoon Well	Western Australia	128	0.79	0.008	1011200	1.55	2
Kambalda district	Western Australia	34.3	3.08	0.25	1055516	1.62	2
Lake Johnston	Western Australia	1.3	1.81	n.a.	251228	0.39	2
Mt. Keith	Western Australia	503	0.55	0.01	2766500	4.24	2
Perseverance	Western Australia	129.1	0.97	0.06	1252270	1.92	2
Windarra	Western Australia	6.66	1.21	0.16	80586	0.12	2
Widgiemooltha	Western Australia	21	1.66	0.17	350094	0.54	2
Yakabindi	Western Australia	290	0.58	0.008	168200	2.58	2
O'Toole	Brazil	6.6	2.2	0.4	145200	0.22	2
Thompson Belt	Manitoba, Canada	89	2.5	0.13	222500	3.41	2
Cape Smith (Raglan)	Quebec, Canada	18.5	3.13	0.88	579050	0.89	2
Hunter's Road	Zimbawe	30	0.7	n.a.	210000	0.32	2
Shangani	Zimbawe	22	0.71	n.a.	156200	0.24	2
Trojan	Zimbawe	20.4	0.68	n.a.	138380	0.21	2
Pechenga	Russia	36	1	0.4	360000	0.55	2
Kabanga	Tanzania	11.7	1.72	0.26	201240	0.31	2

Notes: n.a. = not available

Sakatti deposit seems to represent a peculiar case. The chemical composition of the ores within this deposit seem to categorize it as a class 1 deposit, but the ultramafic host rock and geological setting seems to better fit the class 2. The Sakatti deposit seems to be an unusual example of a Ni-Cu-(PGE) deposit with anomalously low Ni/Cu ratios due to its high copper content.

Table 2. Estimated compositions of sulfides fraction from some Ni deposits. After Barnes & Lightfoot (2005).

	n	S (%)	Fe (%)	Ni (%)	Cu (%)	Ag (ppm)	As	Co	Sb	Se	Zn	Os (ppb)	Ir	Ru	Rh	Pt	Pd	Au	Ref
Sudbury, Strathcona deposit, Class 1 (i)																			
Dissseminated	2	38.16	52.64	4.08	5.13	n.a.	80	2522	369	74	3791	101	211	469	452	3684	4324	1651	1
Massive	37	n.l.	n.l.	3.63	1.23	n.a.	n.a.	1500	n.a.	n.a.	233	8	14	21	30	858	882	100	2
Fe-rich	10	n.l.	n.l.	3.10	0.37	n.a.	n.a.	2100	n.a.	n.a.	n.a.	20	29	52	60	114	105	19	2
Cu-rich	32	n.l.	n.l.	1.97	28.27	n.a.	n.a.	300	n.a.	n.a.	2750	<0.5	0.11	<2	<0.16	4710	5213	296	2
Noril'sk-Talnakh, Oktabr'sky deposit, Class 1 (ii)																			
Disseminated	11	37.14	46.14	3.35	13.37	61	0.86	1558	0.52	n.a.	477	57	46	136	321	6808	25184	4307	3
Massive and matrix	33	37.24	55.71	3.63	12.27	47	2.30	1400	0.52	111	322	30	24	63	259	9421	29049	1217	3
Fe-rich Pd/Ir < diss	23	37.97	57.98	4.07	6.24	13	0.51	1657	0.15	70	187	30	31	81	339	2602	12435	238	3
Cu-rich Pd/Ir > diss	10	35.55	42.43	2.63	26.15	126	6.43	809	1.37	123	631	28	9	21	75	25103	67260	3470	3
Vein	2	34.73	35.85	2.65	32.21	75	5.07	690	0.89	n.a.	384	<1	1.10	6	22	28395	38821	2249	3
Voisey's Bay, Eastern Deeps deposit, Class 1 (iii)																			
Disseminated	25	n.l.	n.l.	6.08	3.32	n.a.	n.a.	n.a.	n.a.	n.a.	n.a.	10	6	31	19	360	354	355	4
Massive	12	n.l.	n.l.	3.32	1.15	n.a.	n.a.	n.a.	n.a.	n.a.	n.a.	15	7	26	18	34	144	18	4
Basal breccia sulfide	44	n.l.	n.l.	4.4	2.47	n.a.	n.a.	n.a.	n.a.	n.a.	n.a.	9	5	37	13	242	264	245	4
Western Australia, Perseverance deposit, Class 2 (i)																			
Disseminated	12	37.54	51.56	10.15	0.53	n.a.	n.a.	2410	n.a.	n.a.	n.a.	131	100	227	52	671	1412	56	5
Massive and matrix	15	38.19	53.66	7.72	0.20	n.a.	n.a.	1849	n.a.	n.a.	n.a.	199	158	420	113	176	374	27	5
Breccia	9	38.07	52.65	8.90	0.18	n.a.	n.a.	1958	n.a.	n.a.	n.a.	184	143	420	98	205	575	31	5
Cape Smith, all deposits, Class 2 (i)																			
Disseminated	89	36.99	48.21	11.43	3.38	14	142	3000	34.54	116	1436	351	264	1553	625	3530	9581	380	3
Massive and matrix	57	37.74	51.90	8.40	1.95	3	6		2.06	122	181	146	117	717	483	2052	3227	72	3
Fe-rich Pd/Ir < diss	32	37.77	52.15	8.65	1.43	2	7		1.53	113	171	173	154	917	601	1542	1907	54	3
Cu-rich Pd/Ir > diss	17	37.67	51.23	7.82	3.28	3	4		2.32	135	176	86	49	271	238	3375	6079	125	3
Vein	5	35.17	38.73	17.16	8.95	36	53		17.37	76		26	11	75	71	1985	14961	3734	3
Pechenga, all deposits, Class 2 (ii)																			
Disseminated	21	37.08	47.72	8.15	3.57	30	37	2477	3.97	75	481	26	26	57	36	917	998	156	6
Massive	16	37.24	49.19	9.43	2.07	18	29	2132	0.65	82	219	63	47	103	57	333	417	69	6
Sulfide separates	15	37.43	50.17	8.69	1.95	8	22	2008	0.50	82	144	62	41	118	51	375	346	101	6
Fe-rich Pd/Ir < diss	12	37.34	49.50	8.78	2.18	15	26	2112	0.74	72	265	99	63	135	65	208	258	43	6
Pd/Ir > diss	4	36.94	48.28	11.72	1.77	34	42	2193	0.43	120	124	17	21	49	38	1383	1766	288	6
Breccia matrix	18	37.75	51.67	7.40	1.31	17	68	1778	1.00	73	290	39	35	61	48	467	443	109	6
Vein	1	34.43	28.58	2.96	34.02	90	7	405	0.24	67	1392	442	221	511	122	223	51	42	6
Sedimentary	6	52.51	44.20	0.22	0.31	3	121	219	10.74	21	1309	<6	2	<10	<10	30	30	50	6

Notes: n.l. = the metal values were reported reculated to 100% sulfides but Fe and S were not reported, n.a. = no analyses; Ref: 1= this work, 2 = Li et al. (1993), 3 = Barnes (1997b), 4 = Naldrett et al. (2000), 5 = S.J. Barnes et al. (1988), 6 = Barnes et al. (2001b)

1.3.1. Origin of sulfide-rich Ni-Cu-(PGE) magmatic deposits

The formation of ultramafic to mafic magmas typically occurs in the asthenospheric or lithospheric mantle, but incorporation of crustal partial melts can greatly modify the composition of these mantle-derived magmas. Nickel ore deposits are 5 to 10 times richer in Ni and Co than the mantle and 100 to 200 times richer than the crust. The enrichment factor of precious metals in ore deposits is approximately 1000 times higher than in the mantle (Barnes and Lightfoot, 2005).

Considering that olivine is a major component of the asthenospheric and lithospheric mantle and that Ni has a moderate partition coefficient in this mineral, a high degree of partial melting of the mantle would be required in order to extract the maximum amount of nickel. For example, komatiites are thought to have the highest degree of partial melting, and they also have the highest Ni content. Cu and PGE do not partition into olivine, which implies that their abundance in melts is mainly controlled by sulfides (Barnes and Lightfoot, 2005). The amount of sulfides incorporated into the melt is controlled by the amount of S that the melt can dissolve. Previous studies on this matter

(Mavrogenes and O'Neill, 1999, Wendlandt 1982) show that at estimated mantle pressures, ultramafic to mafic melts can dissolve 500 to 1000 ppm of sulfur. Therefore,

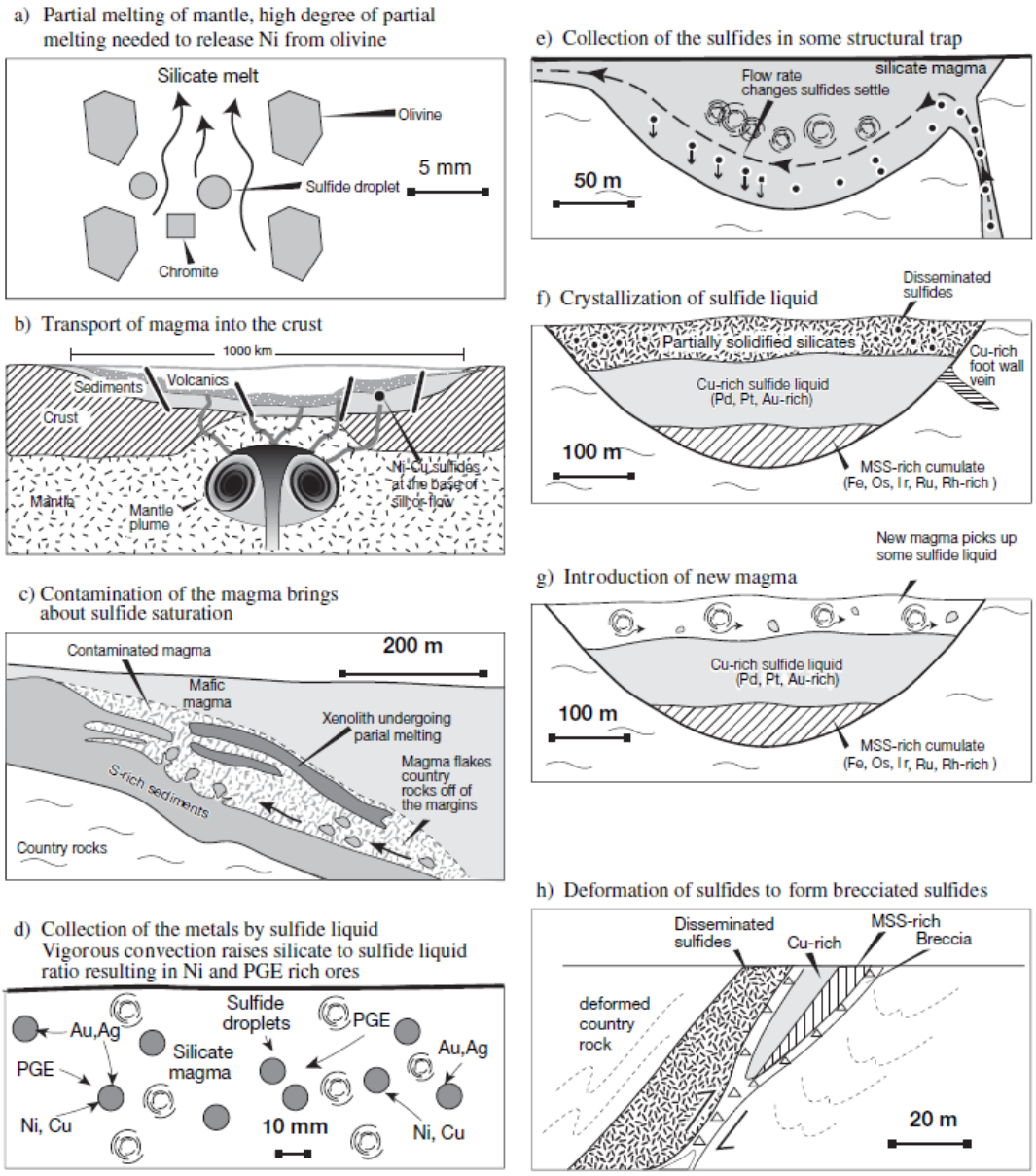

Figure 11. Cartoon outlining the processes that lead to the formation of a Ni sulfide ore deposit. a. The mantle melts to release Ni from olivine and PGE from sulfides. b. Magma is transferred to the crust along crust penetrating faults. c. Sulfur is added to the magma from sediments to bring about saturation of a sulfide liquid. d. The sulfide droplets assimilate chalcophile metals. e. The droplets are transported by the magma until the magma flow slows such that they collect at the base of the intrusion or flow. f. The sulfide liquid undergoes crystal fractionation to produce an MSS cumulate and a Cu-rich liquid that can be injected into the footwall. g. In some cases there may be a new injection of magma and the Cu sulfide liquid may be entrained and moved to a new site collection site. h. Deformation concentrates in the incompetent sulfides, resulting in sulfides being displaced from their parent body, possibly as breccias. After Barnes & Lightfoot (2005).

assuming that the mantle carries approximately 200 ppm of S (Lorand 1993) a 20 to 40 % of partial melting would be required to extract all the sulfides in the mantle (e.g. Barnes et al. 1985, Keays 1995, MacLean 1969). This again matches with the need for high degrees of mantle melting such as 50 % observed in komatiites from the Barberton Mountain Land (Herzberg 1992).

All in all, a degree of partial melting at which the maximum content of Ni is incorporated would imply that all the sulfides in the mantle have been extracted (Naldrett et al. 2011).

1.4. Common features in Ni-Cu-(PGE) deposits

Within these deposits, Ni and Cu are hosted by metal sulfides. The typical mineral assemblage consists of intergrowths of pentlandite ($[FeNi]_9S_8$), pyrrhotite (Fe_7S_8) and chalcopyrite ($FeCuS_2$). Depending on the deposit, also Cu-bearing minerals such as cubanite (Fe_2CuS_3), mooihookite ($Cu_9Fe_9S_{16}$), and talnakhite ($Cu_9[Fe,Ni_8]S_{16}$) may be present. In most cases, 1 to 15 percent of magnetite is found associated with these sulfides. Cobalt, PGE and Au are extracted from most magmatic Ni-Cu ores as by-products, with a significant impact on the economic value of some deposits such as Norilsk-Talnakh (Barnes and Lightfoot, 2005). Cobalt tends to occur, up to a percent level, within the pentlandite mineral structure substituting the nickel. The PGEs are typically present as platinum-group minerals (PGMs) as small grains of PGE-bearing arsenides, sulfides, tellurides, bismithides and atimonides, which can exsolve from the base metal sulfides or from S-poor melts and occur at or near grain boundaries (Cabri 1981, Makovicky 2002). It is also fairly common to find a large proportion of the Pd contained in pentlandite as a solid solution (Distler 1994, Paktunc et al. 1990).

The rise of these metal-bearing mantle melts typically would need to be effectively conveyed through the crust with a minimum degree of olivine fractionation and sulfide segregation. After the emplacement of the melt, metal sulfide liquid saturation must occur in order for a Ni-Cu-PGE deposit to form. In summary, the factors leading to the saturation of silicate magma in Fe-sulfide liquid include: (a) a drop in temperature, (b) an increase in pressure, (c) an increase in fO_2, (d) a decrease of fS_2, (e) a change in the

melt composition (particularly a drop in Fe or a rise in SiO_2, $Na_2O + K_2O$, or MgO) (Barnes and Lightfoot, 2005, Mavrogenes and O'Neill, 1999, Naldrett 2013).

The sulfur saturation will cause the exsolution of an immiscible sulfide melt from the silicate melt in the form of droplets (Figure 11). The ability of these droplets to scavenge metals from the silicate magma is strongly linked to two main factors, the chalcophile nature of the metals and the degree of interaction between the sulfide and silicate melt (Barnes and Lightfoot, 2005, Naldrett 2013). The amount of these elements that partitions into the sulfide melt is strongly controlled by the "R factor" (silicate-magma/sulfide-magma ratio) and the "N factor" (total mass of sulfide magma divided by total mass of silicate magma) (Barnes and Lightfoot, 2005, Naldrett 2013).Taking the above into account, it is possible to understand why, in general, massive sulfides show lower metal tenors than disseminated ores that could have interacted for a longer time with larger amount of silicate magma due to a lower R factor and a higher N factor than those of massive sulfides. Pd/Ir ratios in massive ores are generally lower than in disseminated sulfides, and massive and net-textured ores show a wider range of Ni/Cu and Pd/Ir ratios than the disseminated ore. This could be explained by combining the R and N factors with the fractional crystallization that is thought to occur in sulfide melts as the temperature drops (Barnes and Lightfoot, 2005, Naldrett 2013).

Transport and deposition of these sulfide droplets is controlled by gravity and the flow of the magma. The presence of a structural trap (e.g. embayment in the footwall) is essential in many cases to form a deposit as it will cause the flow rate to decrease, and therefore the gravity effect will increase, allowing the percolation and accumulation of sulfide droplets at the bottom of the flow or intrusion as massive or semi-massive bodies. This process is explained in a simple way by Naldrett (1973) with the "billiard-ball model". These sulfides may occur in different forms such as disseminated, matrix or net-textured, massive and stockwork veins. The disseminated ore in most cases occurs as irregular 1-mm to 1-cm patches that occupy the interstitial space between silicates and oxide minerals. However, at some localities like Norilsk-Talnakh, Pechenga, and Insizwa, South Africa, sulfides occur as 1 to 10-cm sized globules (Barnes and Lightfoot, 2005). The massive ores tend to be found at the contacts between the country rock and the host

rock. Stockwork veins represent massive to semi-massive ores that migrated away from the main massive ore as fractionation proceeded.

Weathering and metamorphism can extensively affect the Ni-Cu-(PGE) deposits, causing the primary mineralogy to be modified partially or completely. Supergene alteration is rather common within deeply weathered terranes, causing the loss of S and/or base metals. In such case, primary sulfides have been replaced by secondary ore minerals such as violarite, bravoite, millerite and in some cases native Cu or Cu oxides. On the other hand, metamorphism could have caused the Fe-sulfides to become oxidized, leading for example to pyrrhotite being replaced by magnetite (e.g., Cawthorn and Meyer, 1993).
Deformation can complicate the relationship between sulfide and silicate minerals. Sulfide minerals tend to represent the incompetent rocks that will focus deformation. Meanwhile, the host rocks generally will not deform so easily, showing more brittle behaviour, which could lead to a brecciated texture with a matrix of deformed sulfide minerals. This texture has also been referred to as “durchbewegung” (Vokes 1969) and is an especially common feature in the Thompson and Pechenga deposits.

1.5. Fractionation of sulfide liquid

As a general rule, the typical ore types found in an orthomagmatic Ni-Cu-(PGE) deposits are massive, stockwork veins and disseminated, with intermediate stages such as semi-massive or net-textured ores (Barnes and Lightfoot, 2005, Dare et al. 2011, 2014, Naldrett 2013). In the following, a description of the widely accepted genetic concept of these ore types will be presented.
It has been known for a long time that sulfide melts commonly experience fractional crystallization (Hawley 1965, Keays and Crocket, 1970, Naldrett et al. 1982). It has been pointed out (Chai and Naldrett, 1992, Naldrett et al. 1994a, Naldrett et al. 1994b, Naldrett et al. 1994c, Zientek et al. 1994) that similar to the fractional crystallization in silicates, the sulfides also tend to form cumulus phases, such as the monosulfide solid solution (MSS) or the intermediate solid solution (ISS) which become isolated from the fractionating liquid to varying degrees. This fractional crystallization is also controlled

by the degree of fractionation and possible migration of the remaining fractionated liquid away from the crystallized materials.

The monosulfide solid solution is a high temperature equivalent of pyrrhotite (Naldrett 2013) that starts to crystallize from the sulfide melt at ~1,200°C. The oxygen content of the sulfide liquid controls the formation of primary magnetite (Naldrett et al. 2011). When the temperature drops below 1000°C, Ni and Co become moderately compatible whereas the Cu becomes strongly incompatible. Also, Pt, Pd and Au are incompatible with MSS, whereas IPGE (Os, Ir and Ru) and Rh are highly compatible. Therefore, the Fe-rich MSS tend to become Ni, Co and IPGE plus Rh enriched while the remaining liquid become richer in Cu, Pt, Pd and Au (Barnes and Lightfoot, 2005).

The intermediate solid solution starts to crystallize at ~900 °C, at which temperature a high percentage of the initial sulfide liquid has already crystallized. Cu becomes strongly compatible with it, and Se joins Ni and Co as moderately compatible elements. Nevertheless, Pt, Pd and Au together with Te, Bi and As remain incompatible with the cumulus phases and continue to concentrate in the residual melt (Barnes and Lightfoot, 2005, Barnes et al. 1997, Dare et al. 2014, Li et al. 1992, Liu and Brenan, 2015). It is important to note that during the cooling process all the solid phases continue to re-equilibrate. The exsolution of pentlandite begins at temperatures below 850 °C and is tightly bound to the sulfur content of the system; the higher the S content, the lower the temperature of formation (Naldrett et al. 2011).

According to the genetic model described above, pyrrhotite and pentlandite exsolve from the MSS and later chalcopyrite from the ISS as the temperature keeps decreasing (Naldrett et al. 2011). Pd, Pt, Au, Te, Bi and As become enriched in the last drops of sulfide melt and should therefore be commonly linked to the ISS. However, it has also been shown that Pd can be present in considerable amounts in pentlandite. This could be explained by diffusion of this element into pentlandite during cooling (Godel et al. 2006).

With the progression of sulfide fractionation, the wetting ability of the residual melt increases as the Cu content rises, and this could be associated with a capillarity effect that is thought to have a major influence on the tendency of the fractionated liquid to escape,

leaving behind the MSS which has been categorized as dry MSS. Capillarity could also be supported or triggered by deformation or strain, which could lead to the injection of this Cu-rich liquid into fractures, ultimately giving rise to Cu-rich stockwork veins (e.g. footwall Cu veins at Sudbury, Canada) or just a dissemination (Barnes and Lightfoot, 2005). It is possible for the ISS not to migrate and therefore also form massive sulfide accumulations at the transition zone in between the MSS and ISS (Barnes and Lightfoot, 2005, Naldrett et al. 1982, Naldrett et al. 2011). A general comparison between mineralization styles in several magmatic deposits can be seen in table 3.

The wettability of a sulfide melt in reference to the silicate and oxide phases is dictated by the dihedral angle. This dihedral angle is the angle formed by two intersecting walls of a liquid filled pore at a junction with two solid grains. The value of this angle is defined by the amount of solid-liquid contact required to minimize the total surface energy of the system. A dihedral angle below 60 degrees classifies a melt as wetting and occupies prismatic grain edge channels, which remain open allowing an interconnected melt phase in three dimensions (Rose and Brenan, 2001).

2. METHODS

This chapter provides a concise description of the sample selection, including QA/QC (quality assurance / quality control) procedures and methods of chemical analysis.

2.1. Sample selection

To enable adequate characterization of the disseminated ore, the sample selection followed three main premises. **1)** Sampling was focused on the dominant Cu-rich dissemination within the peridotite unit and in lesser amounts in the bottom dunite. **2)** Grade representativeness. Within the range of Cu-grades, samples were collected from low, medium and high grades in a spread that was as even as possible and proportional to their abundances. **3)** Spatial representativeness. Proper spatial distribution was maintained throughout the entire deposit, with a major focus on the Main body.

Table 3. General characteristics of the typical mineralization styles in magmatic deposits. After Barnes & Lightfoot (2005).

Massive Sulfides	Disseminated Sulfides	Vein Sulfides
Sulfides interconnected (lenses, layers)	Sulfides not interconnected	Sulfides interconnected
Massive appearance	Net-textured appearance	Massive appearance (stringers)
Several m thick lenses	Irregular mm-cm thick patches or globules	Varying in thickness from a few mm to m
28 - 38 wt. % S content in rocks containing mineralization	0.6 - 17 wt. % S content in rocks containing mineralization	28 - 38 % S content in rocks containing mineralization
LowPd/Ir ratios	Medium Pd/Ir ratios	High Pd/Ir ratios
High Ni/Cu ratios	Medium Ni/Cu ratios	Low Ni/Cu ratios
Related to MSS segregation	More related to ISS segregation	Related to ISS segregation
Fe-rich portion enriched in Ni, Os, Ir, Ru, Rh (Re) Cu-rich portion enriched in Pt, Pd, Au and Ag	Enriched in Pt, Pd, Au	Enriched in Cu, Pt, Pd, Au, Ag, Te, Bi, As

The first step involved studying the Cu grade ranges within the whole rock chemical assays of the disseminated ore. As agreed with Janne Siikaluoma (pers. comm. 2018), a cut-off grade of 0.2 wt. % of Cu and a cap of 1.56 wt. % of Cu was established. The cap value depicts an approximate boundary point between the disseminated ore grades and net-textured ore like grades. The predominance of lower grades seems to characterize the disseminated ore, with the largest amounts ranging from about 0.2 to 0.4 wt. % Cu. Figure 12 shows a clear trend, where the higher Cu grades are the least abundant and vice versa. Following this pattern, the disseminated ore has been classified into 3 different categories: **a)** low Cu grade, 0.2 to < 0.4 wt. % Cu; **b)** medium Cu-grade, 0.4 to < 0.8 wt. % Cu; **c)** high Cu-grade, 0.8 – 1.56 wt. % Cu.

The next stage involved drill hole selection according to the premise of spatial and ore grade representativeness previously established. For that, a Leapfrog 3D model of the deposit was used, where the drill holes were plotted that remained after the application of the geochemical filter. As the deposit in the Main body extends NW-SE and NE-SW, with the longest axis and major metal tenor variation towards NW-SE, the samples were mainly collected in this direction. A tentative selection of the ideal holes was done, plus possible alternative drill holes were chosen.

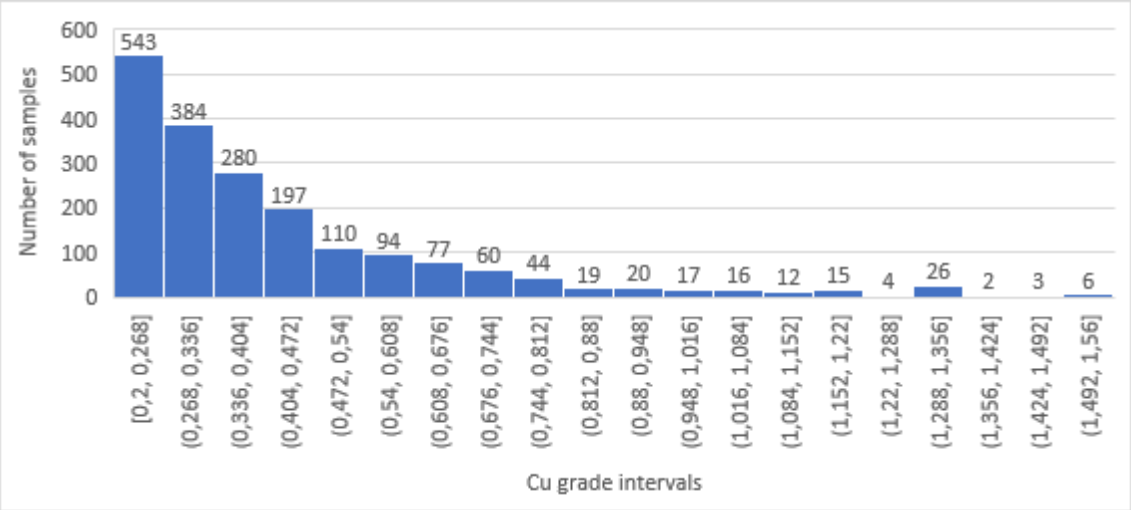

Figure 12. Histogram that represents the general abundancies of samples in different Cu grade intervals.

The last filter to reach the final selection of samples consisted of carrying out an in-situ review of the chosen drill holes. At this stage, a 4th premise for sample selection was assigned, which involved focusing the sampling only on the disseminated ore that showed a clear predominance of chalcopyrite, as unaltered as possible. With the help of a portable X-ray fluorescence (pXRF) device and visual characterization the sampling was completed. A total of 26 holes were checked, of which 18 were selected (Figure 13) and 63 samples were collected. From 41 samples polished thin sections were prepared for petrographic studies and SEM (Scanning Electron Microscope) analysis. 19 samples were sent to a laboratory and chemically analysed for their base metals, gold and platinum group elements (PGE). Three representative samples were selected for X-ray computed tomography study.

2.2. Mineral characterization

The characterization of the mineral phases started with a visual examination of the drill cores, continued with petrographic microscopy and was completed with a FE-SEM-EDS (Field Emission Scanning Electron Microscope with an Energy Dispersive Spectroscopy) and SEM-EDS (Scanning Electron Microscope with an Energy Dispersive Spectroscopy) analysis. The petrographic microscopy comprised transmitted and reflected microscopy study of the 41 polished thin sections. The main target was to identify sulfide minerals

and characterize how they are related to the surrounding silicates and oxides. Mineral phases that were not possible to characterize using only microscopy were analyzed using a FE-SEM-EDS at the Geological Survey of Finland and SEM-EDS at the University of Helsinki. The FE-SEM-EDS machine model was a EOL TM JSM-7100F and the SEM-EDS model was a modernized Jeol JXA-8600 superprobe.

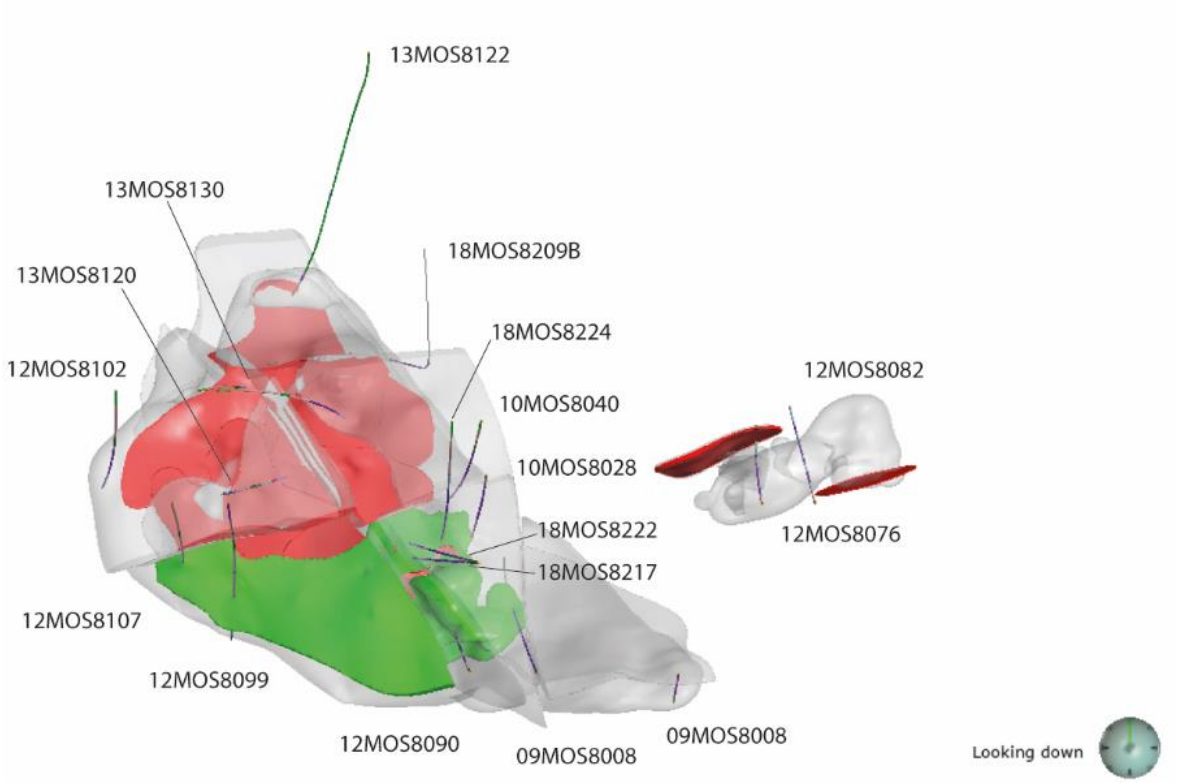

Figure 13. Drill holes location for disseminated ore sampling. After Sakatti 3D model (2017).

2.3. X-ray computed tomography

X-ray Computed Tomography (XCT) is a non-destructive method that allows the visualization of the internal features of solid material and its 3D characterization.

This technique takes what are called XCT (X-ray Computed Tomography) images, which are commonly called slices. These images are formed using voxels, which are pixels to which a third dimension or volume has been added. When all the slices have been made (all the images have been taken), they are combined into a full-scale 3D model of the analysed object. For this study, three drill core samples from 5 to 20 cm long and 5 cm

wide were analyzed. Analysis time have a direct impact on the resolution and therefore the detectable grain size.

The obtained images are representations of the variation in the attenuation of the X-rays that occurs when the beams cross the sample. The attenuation depends on the atomic number of the material. The denser the mineral (i.e. the higher the atomic number), the greater the attenuation and vice-versa. Therefore, as this study used back-scattered imaging, the denser phases in the obtained images are brighter than the less dense ones. The purpose of this technique in this study is to evaluate the feasibility of doing a mineral phase differentiation and a 3D textural study in order to identify the wettability and connectivity of the disseminated ore grains. Moreover, the effect of the structural features on the ore was also checked.

The analysis was done at the Geological Survey of Finland (GTK) and the model of the machine used was GE phoenix v|tome|x s. The obtained three-dimensional models were studied with the help of the software PerGeos. Using PerGeos it was possible to visually inspect the models through the surface and in depth by doing cross sections or filtering out mineral phases by their X-ray attenuation. This program also allows to select a range of mineral phases based on their X-ray attenuation and artificially separate their grains. Additionally, it also enables to extract different characteristics of the mineral grains, such as volume and orientation.

2.4. Geochemical analysis

The samples for chemical analysis were sent to the Intertek Genalysis laboratories in Perth, where they were analysed for their contents of 13 elements (S, Co, Ni, Os, Ir, Ru, Re, Rh, Cu, Pd, Pt, Au, Se). Multi-acid digestion and fire assay were used for sample preparation, while Inductively Coupled Plasma Optical Emission Spectrometry (ICP-OES) and Inductively Coupled Plasma Mass Spectrometry (ICP-MS) techniques were utilized for their analysis.

2.4.1. Multi-acid digestion

Three-acid digestion (nitric, perchloric and hydrochloric acids) was used for cobalt, nickel, copper and sulfur. This method completely extracts these elements from the sulfide minerals, but some of the silicates are also partially digested, especially liable phases such as olivine. According to personal communication from specialists at the Intertek Genalysis laboratories, by using 3AH digest, most of the nickel and cobalt from the olivines could have been incorporated into the solution and therefore included in the overall chemical analysis. Meanwhile, refractory phases such as chromite, pyroxenes or amphiboles are more resistant to these acids, which would mean that they would have been attacked to a lesser degree. Nonetheless, this issue seems to not have a noticeable effect on the analysis of PGE, Se, S, Au and Cu contents due to the low amounts of these elements that can be accommodated within silicates.

The Ni and Co values are not initially reliable for geochemical interpretations regarding sulfide phase. Thus, an additional procedure was carried out to obtain a close approximation of the true amounts of these elements in sulfides. For this, the Ni and Co contents of silicates need to be subtracted from the total values of the geochemical analysis. By request, Anglo American staff prepared Ni vs S and Co vs S diagrams based on whole rock geochemical assays of the Sakatti deposit. The values given by the intersection of their trend line with the Ni and Co axis is an indication of the amounts of these elements in the silicates, which was then subtracted from the total Ni.

Four-acid digestion (hydrofluoric, Nitric, Perchloric and Hydrochloric acids) or fusion digest was used for rhenium and selenium. This method includes hydrofluoric acid which has a strong attack on silicate bound minerals, causing the complete incorporation of these elements from silicates and oxide minerals into solution.

2.4.2. Nickel sulfide fire assay

This technique was used for gold, iridium, osmium, palladium, platinum, rhodium, ruthenium and selenium and has been considered to be the most effective for the accurate determination of all PGE (platinum group elements) and Au contents (Hoffman 2002).

A 25 g pulverized portion of the selected sample was combined with a mixture of nickel powder, sodium carbonate, sodium borate, silica and sulfur, called flux (Hoffman 2002). Thereafter this mix was heated to temperatures above 1000 ºC for about 90 minutes in a crucible to completely melt it. This triggered the formation of nickel droplets to scavenge the Au and the platinum group elements from the liquid. Subsequently, the molten material was poured into a mould and allowed to cool. Due to the properties of the components, as the nickel cumulates are denser, they went to the bottom of the mould and the lighter silicates formed a silicate slag on top. Finally, the formed glass bed was dissolved by a hot concentrate of HCL, which dissolved everything except the Au- and PGE-bearing sulfides.

2.4.3. ICP-MS and ICP-OES

ICP-MS was used for the quantification of the elements that were analysed using 4-acid digestion and Ni-S fire assay preparation. However, before using this analytical method, the sulfide residue had to be further digested with a solution of nitric and hydrochloric acids (aqua regia) (Hoffman, 2002). Nevertheless, it needs to be taken into account that this may have caused a partial loss of osmium as volatile (Robert et al. 1971).

After the last digestion, the solution was passed as an aerosol into an argon plasma, which caused the ionization of the sample, allowing the analysis of the elements by the ICP-MS. The outstanding features of this technique are the high accuracy, precision and the low detection limit on the order of parts per billion (Table 4).

Table 4. Elements analyzed with ICP-MS with the detection limits for each element and method used. After Genalysis laboratories.

Element	Au (ppb)	Ir (ppb)	Os (ppb)	Pd (ppb)	Pt (ppb)	Re (ppm)	Rh (ppb)	Ru (ppb)	Se (ppb)
Detection limit	2	1	1	1	1	0.002	1	1	0.5
Method	NS25/MS	NS25/MS	NS25/MS	NS25/MS	NS25/MS	4A/MS	NS25/MS	NS25/MS	4A/MS

The elements extracted with the 3-acid digestion were analyzed with ICP-OES. The solution also passed to an aerosol state, but in this case, it was introduced into a flame,

causing a fraction or all of the metallic ions in the aerosol to be converted into free atoms. These could be detected and quantified at trace level (Table 5) by atomic emission techniques (Fassel and Kniseley, 1974).

Table 5. Elements analyzed with ICP-OES with the detection limits for each element and method used. After Genalysis laboratories.

Element	Co (ppm)	Cu (ppm)	Ni (ppm)	S (%)
Detection limit	10	10	10	0.01
Method	3AH/OE	3AH/OE	3AH/OE	3AH/OE

3. RESULTS

The following section presents the results obtained from the analysis of the selected disseminated samples using the methods previously described. In addition, geochemical assays from massive sulfide samples of the NE and SW bodies are also discussed.

3.1. Macroscopic characterization

The disseminated ore could be subdivided into three groups. **a)** Dissemination characterized by fine-grained sulfides scattered in homogeneous manner (Figure 14a). No apparent connectivity between sulfide grains was observed and seems to exhibit a link to lesser Cu grades. Mainly hosted in the intercumulus phase of ad- to mesocumulates. **b)** The ore occurs distributed as patches (Figure 14b) and appears to be the most abundant type. It shows variable levels of connectivity between these patches depending on the Cu-grades. Nonetheless, no pervasive connectivity was observed within this group. It typically ranges from low to medium Cu-grades and is commonly hosted in the intercumulus phase of ad- to orthocumulates. **c)** Characterized by higher degrees of connectivity that sometimes appears to be similar to net textured ore (Figure 14c). This type typically represents the highest Cu grades generally in the intercumulus of meso- to orthocumulates. This texture is the least common.

The impact of serpentinite veins on the mineralization appears to be minimal; however, carbonate veins seem to cause severe remobilization of the ore, showing an alteration halo from where the sulfides have been leached (Figure 14d). Moreover, when the disseminated ore is close to a pyroxenite layer, the effect is similar to that of carbonate veins; the ore appears to be remobilized towards pyroxenite (Figure 14e).

The proximity to the semi-massive, stockwork or massive ores (Figure 14f) have sometimes affected the original texture, abundance and composition of the disseminated ore, as different degrees of reactions amongst them have occurred.

3.1.2. Petrography

The study of the disseminated ore samples revealed that all the primary sulfide phases are located within the intercumulus phase of olivine ad- to orthocumulates. The general opaque mineralogy is dominated by chalcopyrite and magnetite. The full suite of ore mineral phases that characterize this mineralization type are:

- Sulfide minerals: chalcopyrite, pyrrhotite, pentlandite, marcasite, violarite, millerite, cubanite, pyrite, bornite and covellite.
- Oxides: chromite, magnetite and ilmenite.

Additionally, PGM and a nickel-rich variant of pyrrhotite are present in trace amounts. Some of these minor phases were first spotted with the microscope and later identified and better characterized with FE-SEM-EDS.

No textural and compositional differences in the silicate and ore minerals between the Main body and NE body disseminated samples were observed.

The silicate phases commonly associated with Cu-rich disseminated mineralization are divided into cumulus and intercumulus minerals. In the studied samples olivine and chromites are the only cumulus phases. The intercumulus is formed by ortho- and clinopyroxenes, ortho- and clinoamphiboles, phlogopite and chlorite. Pyroxenes occasionally occur in the form of poikilitic grains. These pyroxenes are usually orthopyroxenes and have inclusions of olivines, sulfide phases and oxides. Sulfide minerals like chalcopyrite have also been observed to grow along the contacts of these grains. The clinoamphiboles may be pargasitic hornblende. These clinoamphiboles and

phlogopite may have a magmatic origin, which could indicate a hydrous melt. However, the amphiboles may have also replaced the pyroxenes in a later phase. Chlorite is common alteration product of pyroxenes. Serpentinization and talc alteration are widespread, being the first the most abundant.

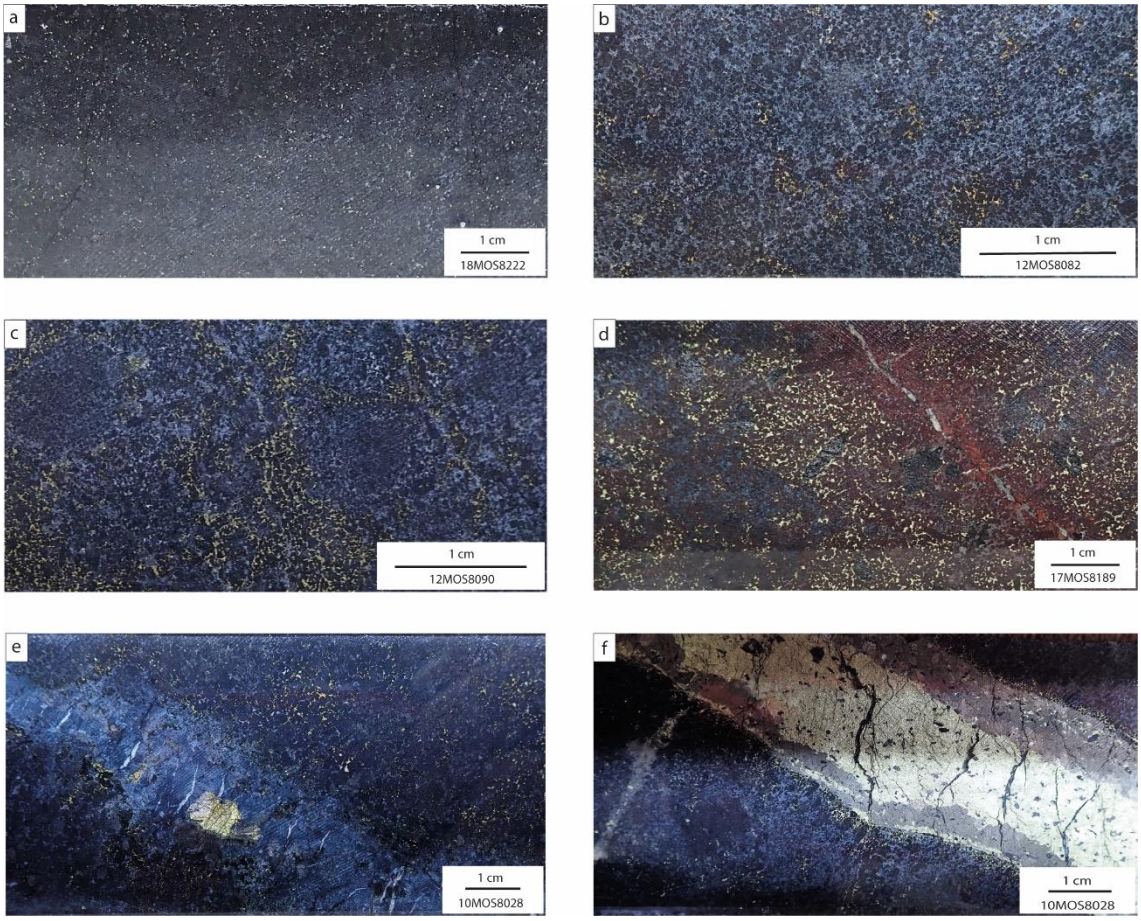

Figure 14. Macroscopic view of the different disseminated ore textures. (a) Homogeneous low Cu grade, (b) patchy low to medium Cu grade, (c) Patchy or interconnected high Cu grade, (d) Carbonate vein leaching the sulfides around it, (e) Pyroxenite leaching the sulfides around it, (f) stockwork vein apparently leaching the disseminated ore.

An in-depth description of the ore minerals will follow, focusing on their spatial distribution and the textural features that characterize this ore type.

3.1.2.1. Chalcopyrite and Cubanite ($CuFeS_2$; $CuFe_2S_3$)

Chalcopyrite is the most abundant sulfide phase within the disseminated ore (Figure 15a). It occurs as clusters or more evenly distributed among the intercumulus phases. The chalcopyrite forms grain aggregates around the olivine cumulus grains which denotes a significant wettability. This fits with the observations by Ebel and Naldrett (1996b) of an

increase in the wetting ability of sulfides with an increase of copper content in crystalizing sulfide melt. Other silicates such as pyroxenes can have a poikilitic texture within which intergrowths or inclusions of chalcopyrite can be found, but certain degree of wetting ability can still be seen through the rims of these silicates. Cubanite occurs as lamellae exsolutions in chalcopyrite (Figure 15b) mainly constrained within the deeper NW part of the Main body (Figure 15d) and with the massive sulfide lenses. No cubanite was found within the NE-body.

Magnetite is the main alteration product of chalcopyrite and cubanite. Propagating from rims and fractures, it can completely replace these copper minerals in a pseudomorphic way (Figure 15c). The presence of nearby minerals more liable to magnetite alteration, such as pyrrhotite, was observed to increase the degree of magnetite alteration of the surrounding chalcopyrite and cubanite. This is evident in the form of reaction rims and magnetite propagating from the more susceptible minerals towards cubanite and chalcopyrite as intergrowths.

3.1.2.2. Pyrrhotite and Pentlandite ($Fe_{(1-x)}S$; $[FeNi]_9S_8$)

Pentlandite normally occurs as exsolutions in pyrrhotite (e.g. flame exsolutions) or as individual crystals, but both minerals can also be found independent of each other. It is common for chalcopyrite to form intergrowths within these phases or to even engulf them in a way that they are left as inclusions within the Cu-Fe-sulfide (Figure 16a). Pyrrhotite and pentlandite seem to have crystallized in an earlier stage than the chalcopyrite, however, in some cases more coeval textures between these minerals have been observed.

Pyrrhotite was observed as three different types **a)** The most common is monoclinic pyrrhotite (Figure 16b), also referred to as magnetic pyrrhotite or 4C pyrrhotite due to its superstructure (Bertaut, 1953). Pyrrhotite is brown to pink-brown in color and is occupying the intercumulus phase. Anisotropism is strong varying from bluish grey to dark brown.

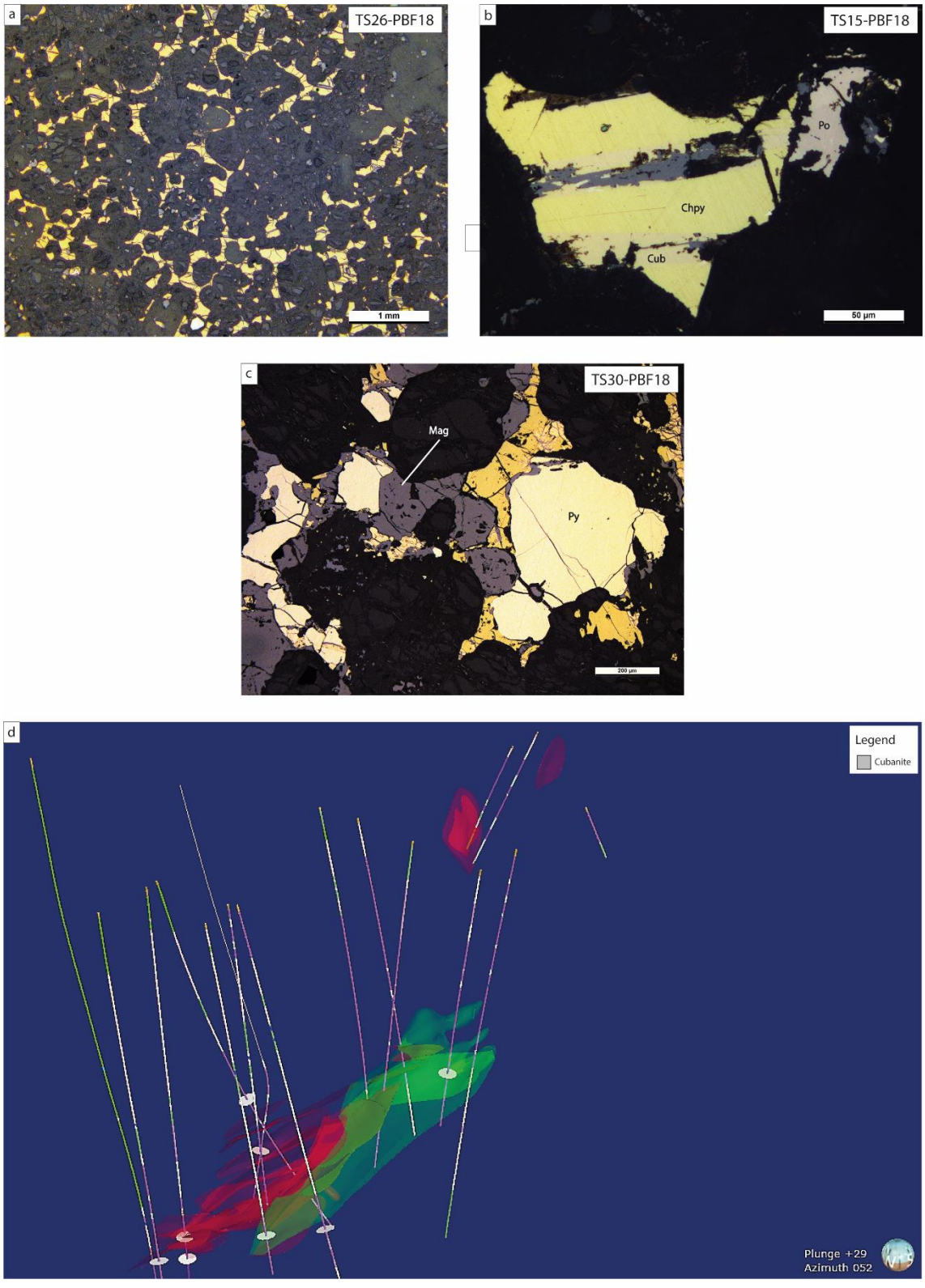

Figure 15. (a) Chalcopyrite general distribution, (b) Cubanite replacing chalcopyrite, (c) Magnetite replacing chalcopyrite, (d) Distribution of samples containing cubanite in the Sakatti deposit. Modified after Sakatti 3D model (2017). Abbreviations: Chpy = chalcopyrite, Po = pyrrhotite, Cub = cubanite, Py = pyrite, Mag = magnetite

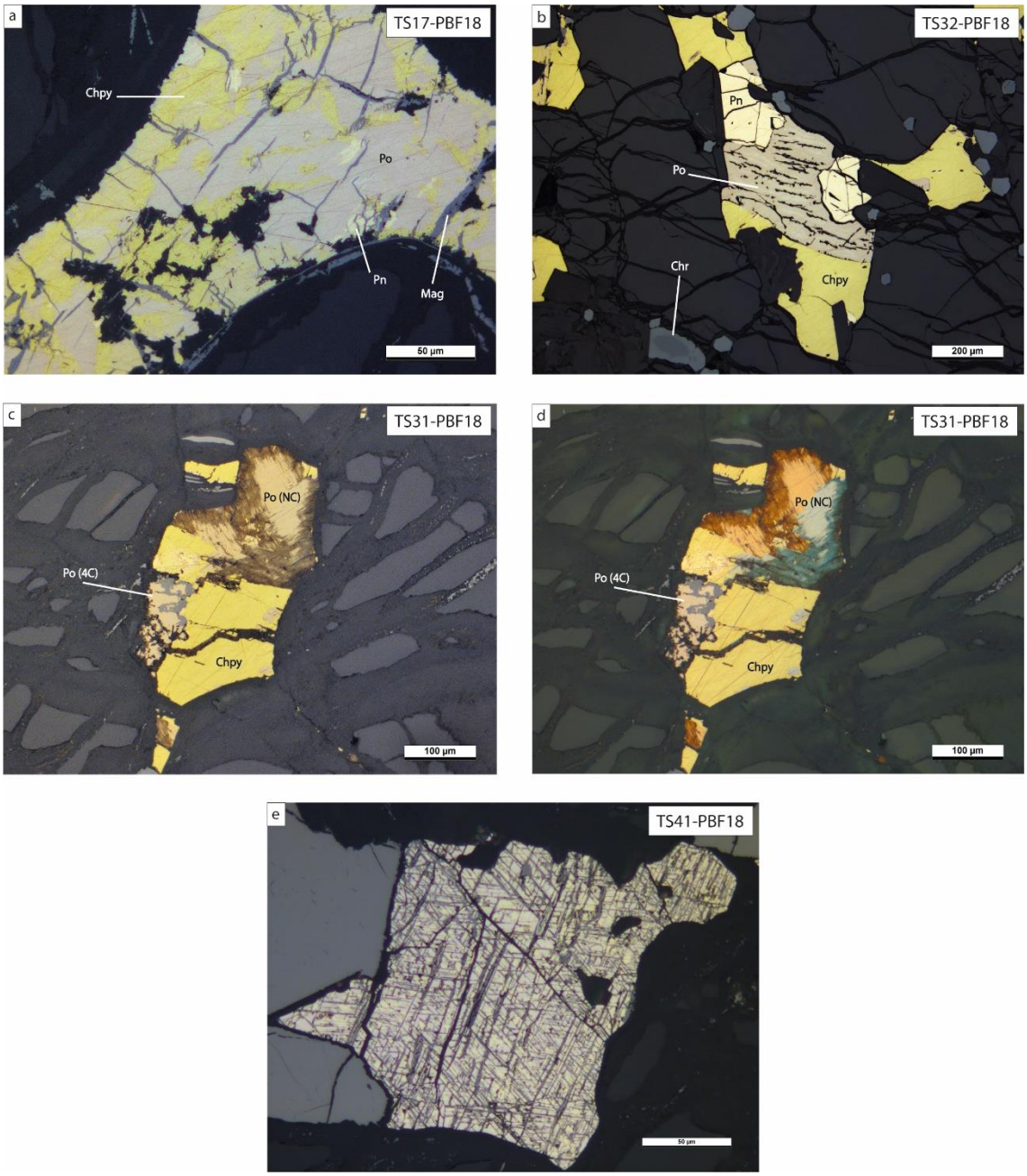

Figure 16. (a) Chalcopyrite intergrown pyrrhotite and pentlandite crystals, (b) NC pyrrhotite stripes within 4C pyrrhotite, (c and d) nickeloan pyrrhotite normal light and crossed nicols, (e) octahedral fracturing of pentlandite crystals through which magnetite develops. Abbreviations: Chpy = chalcopyrite, Po = pyrrhotite, Pn = pentlandite, Chr = chromite, Mag = magnetite

Magnetic pyrrhotite becomes stable below 254 ºC (Figure 17) and may coexist with either NC pyrrhotite (more iron-rich bulk compositions) or pyrite (more sulfur-rich compositions). **b)** Another type of pyrrhotite is also present as exsolutions within a few of the 4C pyrrhotite grains (Figure 16b). This, plus the slightly different optical properties, such as lighter colour, isotropism and the comparison with the FeS-FeS_2 phase diagram stability fields (Figure 17), has led to this variant being categorized as intermediate or

non-magnetite pyrrhotite, also referred to as NC pyrrhotite ($Fe_{n-1}S_n$ (n>8)) in reference to its superstructure. It is a more iron-rich pyrrhotite, as can be seen in the phase diagram (Figure 17), and it can coexist in solid solution at ambient conditions with the 4C variety within approximately 46.9 and 47.2 of Fe atomic %. This intermediate pyrrhotite becomes stable at 204 ºC or lower. It has been called hexagonal pyrrhotite due to the apparent X-ray diffraction symmetry of the NC pyrrhotite (Pósfai et al. 2000). **c)** Nickeloan pyrrhotite ($(Fe,Ni)_7S_8$) (Figure 16c), occurs as small inclusions in chalcopyrite, near the 4C pyrrhotite. Characterized by its anhedral shape, similar colour to 4C variant, alteration rims, twinning and strong anisotropic colours, from a bright blue to an orange-brown (Figure 16d). The identification of this mineral was possible with the aid of FE-SEM-EDS analysis. Nickeloan pyrrhotite is stable at high temperatures, at which some atoms of nickel occupy the structural positions of iron (Becker et al. 2010). Generally, as the temperature decreases and pentlandite becomes stable, it starts exsolving from the Ni-rich pyrrhotite and thereby extracting all the nickel from the structure (Francis and Craig, 1976). Nevertheless, in some cases, this process does not occur and the nickel-bearing pyrrhotite persists.

The main alteration products of pyrrhotite are marcasite and magnetite, which can pseudomorphically replace pyrrhotite. Marcasite differs from its polymorph pyrite in showing strong anisotropism. These alterations can be observed within the whole deposit, but it seems to be more pervasive at shallow depths in the Main body (Figure 18). The alteration degree is generally medium to low, <40%. Magnetite alteration appears to be a later event than marcasite alteration since magnetite has been found replacing marcasite.

Pentlandite is the primary main nickel carrier phase. It is present within the intercumulus phase as un-fractured to widely deformed or broken grains. Additionally, after FE-SEM-EDS analysis imply that some crystals are cobalt-pentlandite. In some samples, pentlandite is more abundant than pyrrhotite (Figure 19). There are some parts of the deposit in which pyrrhotite or its alteration product marcasite are completely absent but

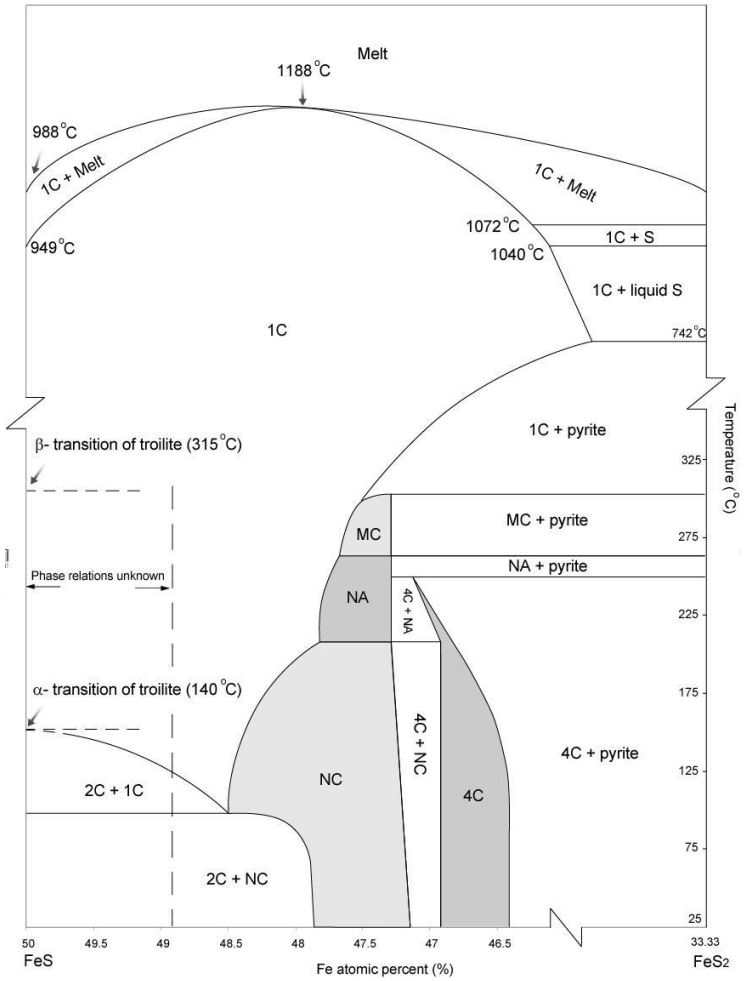

Figure 17. Phase diagram for the system FeS to FeS2 representing stability fields of various pyrrhotite superstructures. After Wang & Salveson (2005).

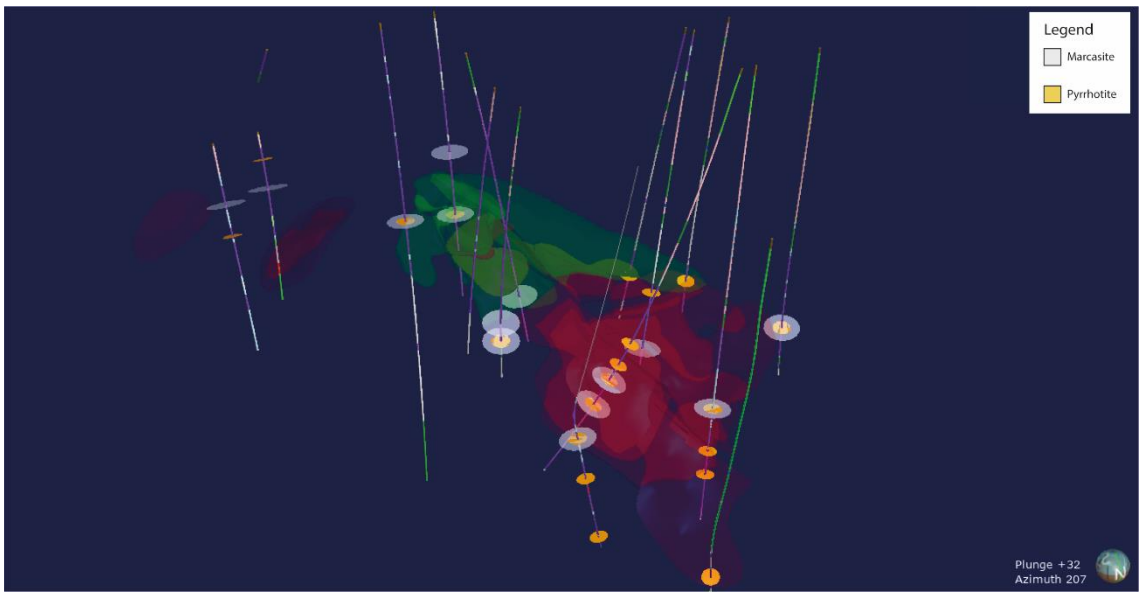

Figure 18. Pyrrhotite and marcasite distribution within the Main and NE bodies of the Sakatti deposit. Modified after Sakatti 3D model (2017).

pentlandite is present. Nonetheless, magnetite grains with shapes resembling the sulfide phases may indicate their previous existence. Additionally, some pentlandite crystals are fractured in the direction of octahedral cleavage (Figure 16e) through which the magnetite alteration spreads.

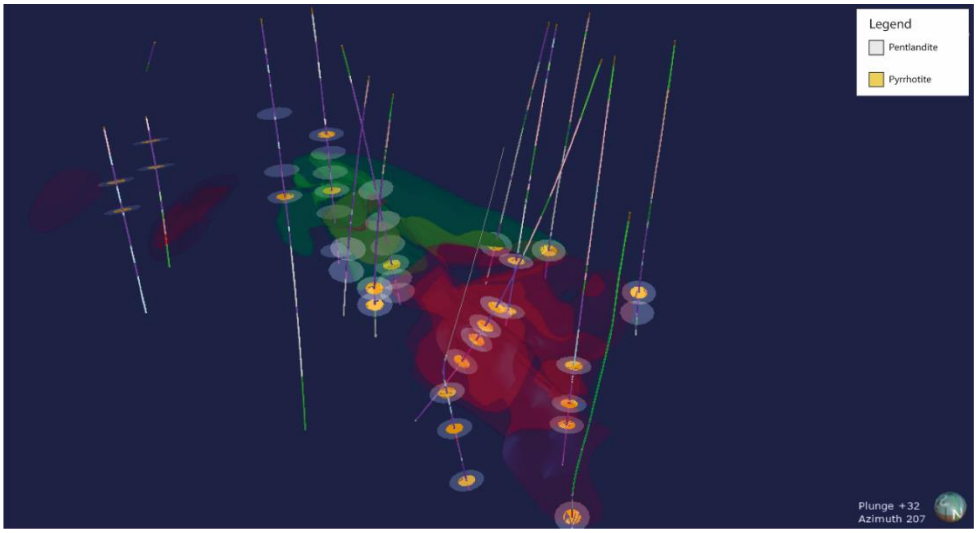

Figure 19. Pyrrhotite and pentlandite distribution within the Main and NE bodies of the Sakatti deposit. Modified after Sakatti 3D model (2017).

3.1.2.3. *Violarite and Millerite ($Fe^{2+}Ni_2S_4$; NiS)*

The alteration products of pentlandite are violarite and millerite. Violarite and millerite occur predominantly in shallow parts of the deposit and the first seems to be more common (Figure 20d). The alteration degree of pentlandite to violarite and millerite is medium to low (<50 %)

Violarite occurs as aggregates of small-sized crystals partially or completely replacing pentlandite in a pseudomorphic way (Figure 20a, b). No nucleation of this mineral outside of pentlandite grains was observed. Characterized by a light grey colour with pink to violet tints, which combined with its isotropism makes it possible to be distinguished from pentlandite with optical microscopy. However, due to its small grain size, the existence of this mineral was first confirmed with a FE-SEM-EDS analysis. Amount of violarite increases close to fractures and cleavages within the pentlandite crystals.

Millerite generally occurs together with violarite replacing pentlandite crystals in a pseudomorphic way. It was also detected partially replacing chalcopyrite (e.g. sample TS24) and in relation to bornite and covellite (Figure 20c). It has a pale colour with yellow tints and is characterized by strong anisotropy that goes from pale yellow to blue. Presence of millerite was confirmed with the aid of FE-SEM-EDS analysis.

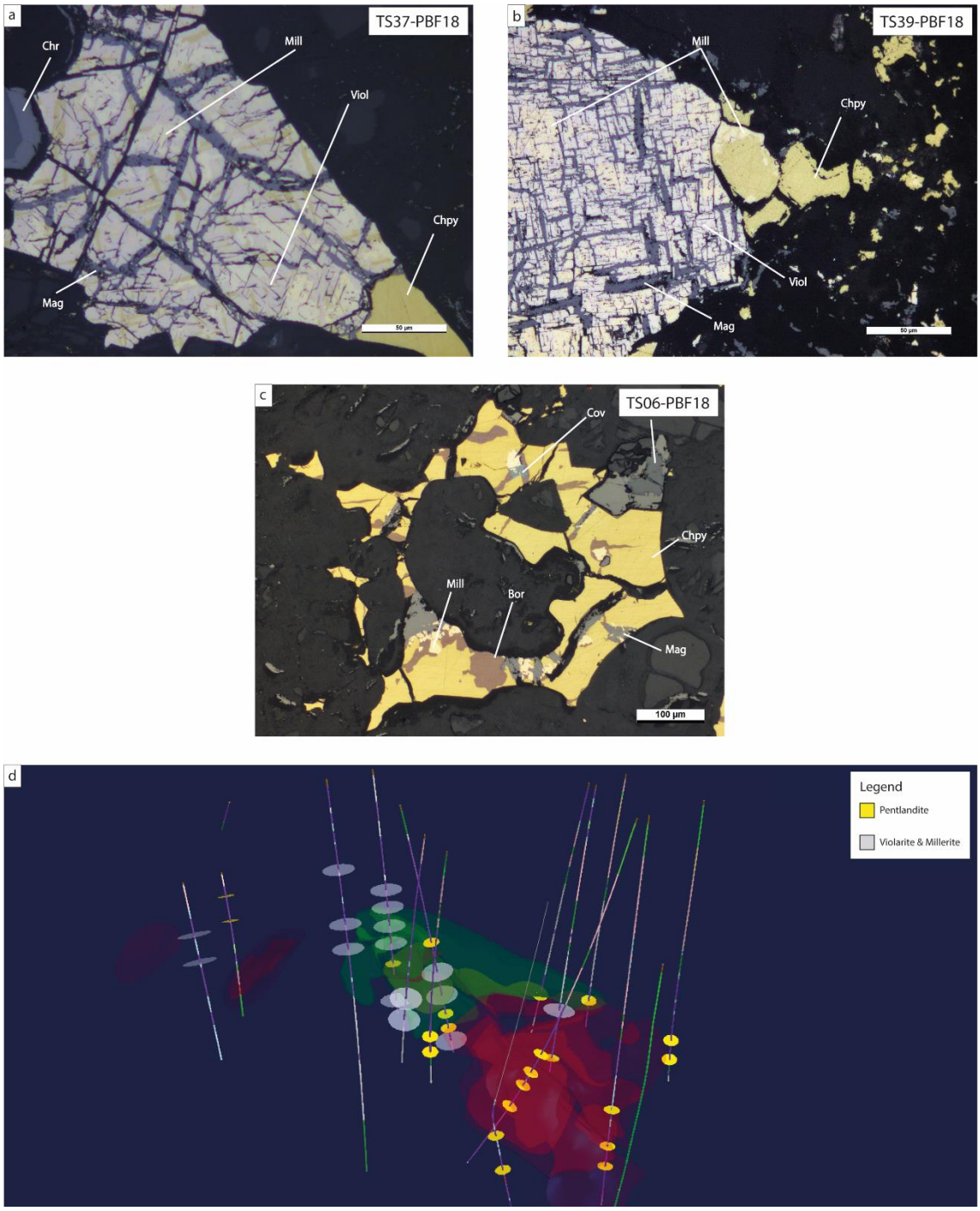

Figure 20. (a and b) Violarite and millerite replacing pentlandite, (c) presence of millerite in relation to bornite and covellite, (d) Distribution within the Main and NE bodies of pentlandite versus violarite and millerite. Modified after Sakatti 3D model (2017). Abbreviations: Chpy = chalcopyrite, Viol = violarite, Pn = pentlandite, Mill = millerite, Bor = bornite, Cov = covellite, Chr = chromite, Mag = magnetite

3.1.2.4. Bornite & Covellite (Cu_5FeS_4 & CuS)

Alteration of violarite and millerite to magnetite occurs predominantly along the cleavages and fractures (Figure 20a, b). However, these minerals appear to be less liable to magnetite alteration than other secondary phases like marcasite.

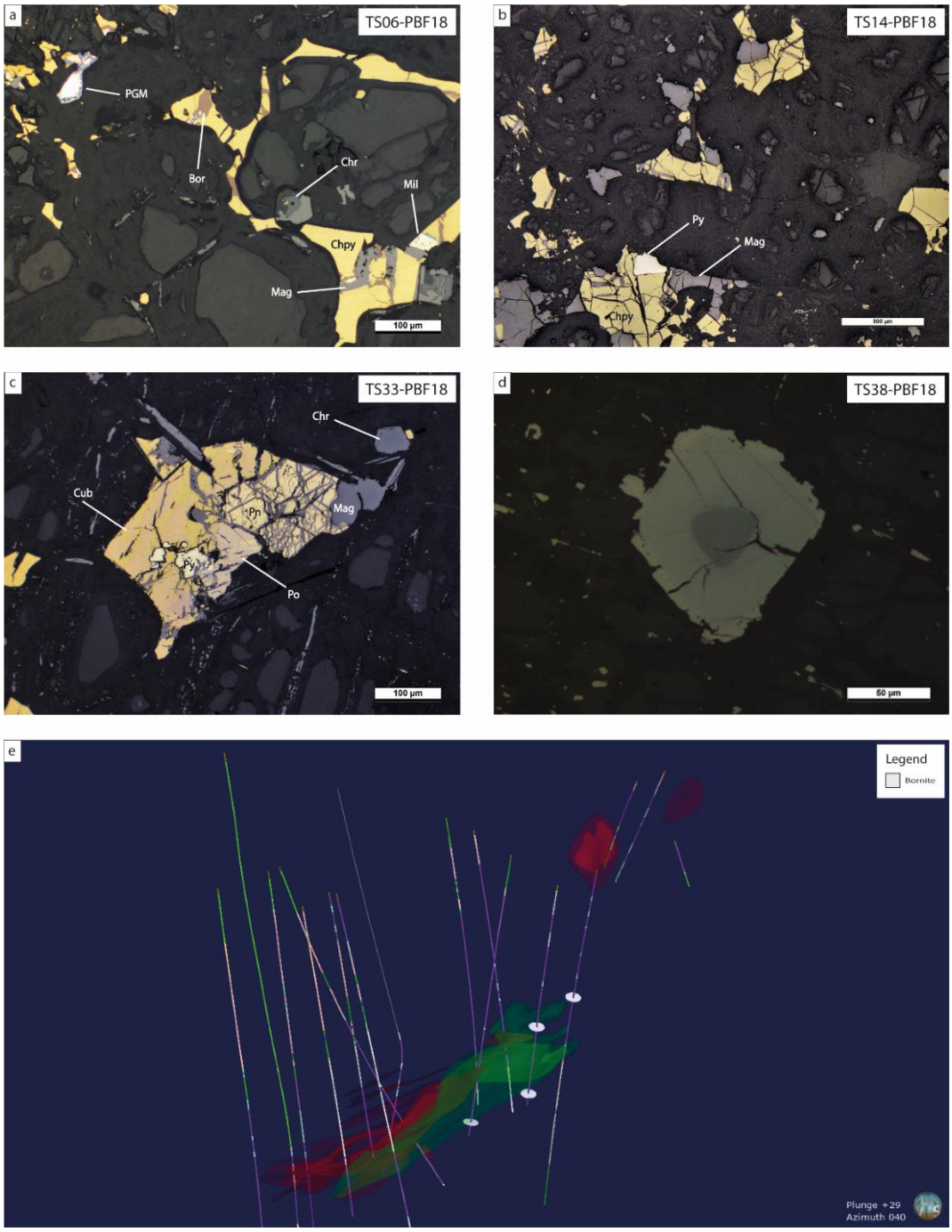

Figure 21. (a) Presence of bornite and a PGM, (b) Euhedral pyrite crystal and magnetite pseudomorphic replacement of chalcopyrite, (c) anhedral pyrite in relation with chalcopyrite, pyrrhotite and pentlandite. (d) triple zonation of a chromite crystal, (e) bornite distribution in the Main and NE bodies. Modified after Sakatti 3D model (2017). Abbreviations: Chpy = chalcopyrite, Po = pyrrhotite, Pn = pentlandite, Bor = bornite, Chr = chromite, Mag = magnetite, PGM = platinum group mineral.

Bornite and covellite were only found locally in the stockwork zone and are constrained to very specific depths in holes 18MOS8217, 17MOS8189 and 12MOS8090 (Figure 21e). The distribution of these samples in the deposit seem to denote a certain orientation and inclination, which seems to approximately match the location, azimuth and dip of the SE-NW faults 1 and 2 (Figure 21e). Bornite and covellite replace chalcopyrite as anhedral crystals through rims, fractures and along the cleavages (Figure 21a). No nucleation of these minerals outside the boundaries of chalcopyrite was observed.

3.1.2.5. Pyrite ($Fe^{+2}S_2$)

Pyrite was observed as anhedral crystals that mainly occur together with chalcopyrite and pentlandite (Figure 21b), however, it also occurs as subhedral to euhedral grains normally linked to chalcopyrite and pyrrhotite or as individual crystals (Figure 21c). No colour anomalies were noted that could indicate contamination of pyrite by another element such as cobalt or nickel. This is backed up by FE-SEM-EDS analysis that confirms the absence of additional elements in its structure. Magnetite appears to be replacing pyrite through rims and fractures, but it seems to be more resistant to this alteration than chalcopyrite.

3.1.2.6 Chromite ($Fe^{+2}Cr_2O_4$)

Chromite is the most abundant oxide after magnetite. It formed before and during early stages of the crystallization of the olivine. With euhedral tendency, the chromite crystals were found spread within cumulus grains, cumulus-intercumulus boundaries and commonly close to the sulfides, with the latter growing around chromites.

Compositional zoning of chromite crystals is common, showing a decrease of chromium content from the core to the rim of the crystals. Thus, the core of these crystals are formed chromite or chromium-spinel while the rims can be composed of just magnetite. Up to three different zones were noted, as shown in Figure 21d.

3.1.2.7. Magnetite ($(Fe^{+2}Fe^{+3})_2O_4$)

As the most abundant oxide, magnetite occurs as an alteration product of all the primary sulfides and some of their alteration products, and chromite. No clear observations of primary magnetite were noted. Nucleation of magnetite generally begins around the rims and fractures of minerals and spreads to the point of pseudomorphic replacement. Moreover, it has been observed that magnetite nucleates outside of the altered mineral forming alteration fronts and propagates to surrounding sulfide phases that were initially in contact with this mineral.
Pyrrhotite and its alteration product marcasite have been found to be the sulfides most liable to magnetite replacement. Magnetite locally seems to be partially or completely replaced by ilmenite in some samples of the NE-body.

3.1.3 FE-SEM-EDS and SEM-EDS analysis

FE-SEM was used on a specific set of samples (Samples TS06, TS13, TS17, TS22, TS32 and TS41) in order to determine the phases that were too small and showed anomalous optical properties or were too similar to those of other minerals. Even more, this method was used to find the phases that generally fall underneath the limit of detection marked by their grain size, such as the platinum-group minerals (PGMs) or other precious metals. Table 6 is a compilation of all the relevant major and minor phases determined with the aid of FE-SEM, of which a description will be given below with a greater focus on PGM, tellurides and certain sulfides.

3.1.3.1. Platinum-group minerals (PGMs)

The PGMs of the disseminated ore are platinum-, palladium- telluride and bismuth-telluride phases, of which 78 % belong to the merenskyite-moncheite-melonite series, 19 % are michenerite and 3 % are sopcheite (Figure 22). They occur in relation to chalcopyrite or its alteration products, although they also occur as grains isolated from sulfides commonly surrounded by serpentine. They also appear in supergene domains where bornite and covellite can be found (Figure 23a). The observed alteration of these

PGMs occurs by replacement of platinum (Pt) and in lesser amount palladium (Pd) by lead (Pb) and silver (Ag). Moreover, magnetite seems to be replacing the PGMs.

The merenskyite-moncheite series minerals have been found in several examples within samples TS06, TS17, TS32 and TS41, and it represents the most abundant platinum-group minerals. Of this series, moncheite predominates and exhibits euhedral to anhedral

Table 6. Major and minor phases of the disseminated ore determined with FE-SEM-EDS

Type	Mineral/Phase	Composition
PGM	Moncheite	$(Pt,Pd)(Te,Bi)_2$
	Merenskyite	$(Pd,Pt)(Te,Bi)_2$
	Michenerite	(Pd,Pt)BiTe
	Sopcheite	$Ag_4Pd_3Te_4$
Tellurides	Altaite	PbTe
	Melonite	$NiTe_2$
	Rucklidgeite	$(Bi,Pb)_3Te_4$
	Hessite	Ag_2Te
Sulphides	Cobalt-Pentlandite	$(Co,Ni,Fe)_9S_8$
	Violarite	$FeNi_2S_4$
	Millerite	NiS
	Nickeloan pyrrhotite	$(Fe,Ni)_7S_8$
	Galena	PbS
	Heazlewoodite	Ni_3S_2
	Co-Pyrite	$(Fe,Co)S_2$
	Cobaltite	CoAsS
	Gersdorffite-arsenopyrite-cobaltite ss	NiAsS-FeAsS-CoAsS (*ss)*
Precious metals	Electrum	(Au,Ag)
	Native Gold	Au
	Native Silver	Ag
Oxides	Baddeleyite	ZrO_2
Sulphates	Barite	$BaSO_4$
Phosphates	Apatite	$Ca_5(PO_4)_3F$

Shapes (Figure 23). The platinum and palladium remobilization from PGMs and substitutïon by Pb and Ag seem to be fairly common for the moncheite, where Pd seems to be more mobile than Pt, this matches with what Holwell et al. (2017) observed. Moncheite crystals shows zoning denoting progressive alteration from pure moncheite at the core of the crystal to a Pb-bismuth-telluride (Altaite) at the rims (Figure 23b, c). Also,

magnetite appears to replace moncheite and melonite (Figure 23d), with no trace of Pd and decreasing content of Pt towards the rims, which denotes remobilization.

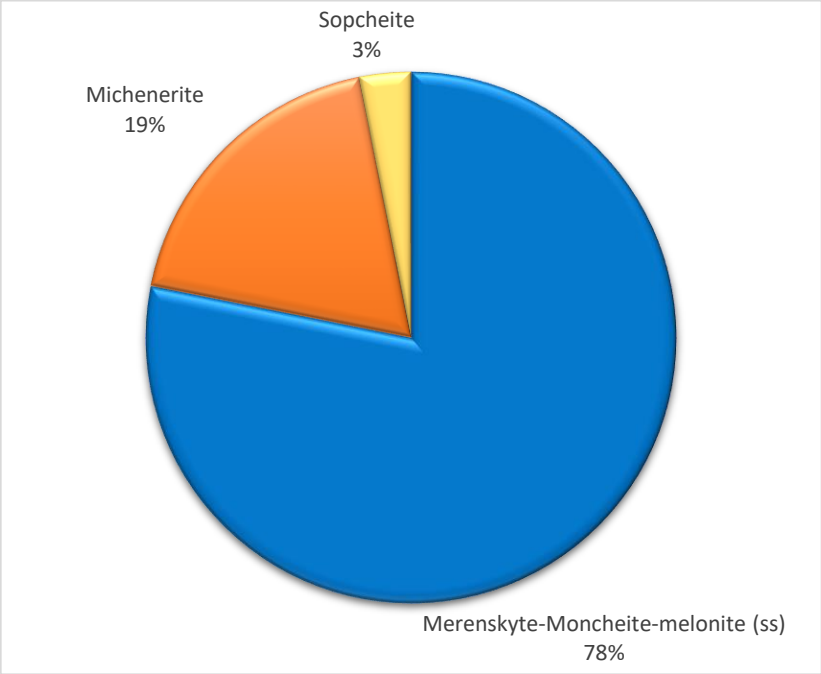

Figure 22. Diagram representing the overall PGM content found in the disseminated ore of Sakatti.

Although michenerite is the second most abundant PGM after the merenskyite-moncheite series, with only four grains observed in samples TS13 and TS06. With its subhedral to anhedral shapes, it also seems to occur in relation to chalcopyrite. Two compositionally different michenerite were observed: one platinum-rich with little or no palladium and the other palladium-rich phase. The alteration of this mineral also involves Pd-Pt remobilization and Pb-Ag incorporation.

Sopcheite was only observed in the rim of a moncheite crystal which had been partially altered altaite. Covellite appears enclosing these platinum-group minerals.

3.1.3.2. Tellurides

The most abundant telluride outside of the platinum-group minerals found in the Sakatti deposit is altaite, followed by melonite, rucklidgeite and hessite.

Altaite occurs close to chalcopyrite, cubanite and heazlewoodite or as separate grains. As previously described, it seems to have a secondary origin, a product of the remobilization of Pt and Pd from PGM and the incorporation of Pb (Figure 23b, c). It is not uncommon to see altaite in contact with melonite, and a Ni-bismuth mineral that may be badenite, although further study would be required to confirm that.

Melonite may represent an end member of the merenskyite-moncheite-melonite solid solution series (Figure 21d). Melonite has also been found related to hessite or altaite and rucklidgeite. This last phase can also carry small amounts of selenium.

3.1.3.3. Sulfides

The sulfide phases discovered with FE-SEM were, cobalt-pentlandite, millerite, galena, heazlewoodite, cobaltite, chalcocite, sphalerite and gersdorffite-arsenopyrite-cobaltite solid solution.

Pentlandite was observed to commonly contain cobalt, which sometimes enabled its classification as cobalt-pentlandite (Figure 23e and Table 7). Millerite was detected in the sample TS06, which is characterized by the presence of hydrothermal sulfides such as bornite and covellite and the absence of pyrrhotite and pentlandite. Pyrrhotite occasionally contained minor amounts of copper.

Heazlewoodite and galena are not abundant sulfides as they could reaffirm the mobilization of nickel and the presence of lead in the system respectively. Heazlewoodite occurs as an individual crystal in contact with chalcopyrite or in mixtures with cobalt-pentlandite. Galena may occur in the contacts between cobalt-pentlandite and chalcopyrite or in mixtures of heazlewoodite and cobalt-pentlandite. The FE-SEMS scans also detected gersdorffite-arsenopyrite-cobaltite solid solution grains. It occurs in close to heazlewoodite, altaite and a Ni-bismuth phase.

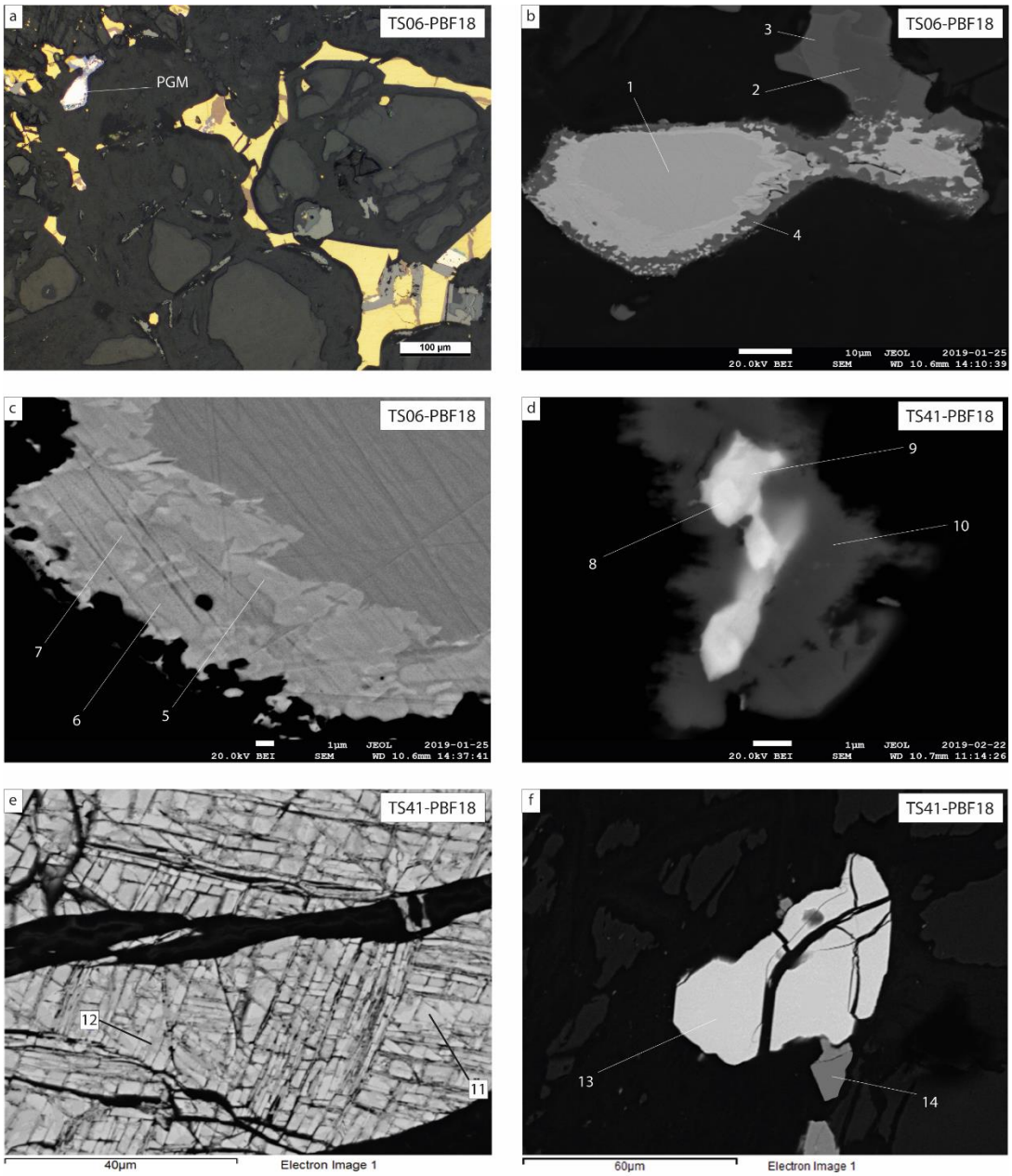

Number	S	O	Fe	Co	Ni	Cu	Pd	Ag	Te	Pt	Bi	Pb	Zr	Hf	Total
1							4.92		60.53	33.63					100
2	35.11		21.92	5.78	37.19										100
3	26.57		11.07			59.46		2.9							100
4	25.57		10.12			60.2		2.72	1.39						100
5									52.84	41,00		6.16			100
6						1.73		8.83	36.11			53.34			100
7									52.36	39.66		7.98			100
8			7.96		7.81				43.97	11.7	28.58				100
9			6.29		11.47				54.04	2.59	25.62				100
10		34.12	65.88												100
11	39.71		19.23	21.72	38.88										100
12	39.66		17.39	67.87	36.16										100
13		30.02											68.07	1.9	100
14		33.59	66.41												100

Notes: All values in weight percentage

Figure 23 and Table 7. Pictures show the mineral distribution and textures of different mineral phases. Picture in a) shows the PGM analyzed through FE-SEM-EDS displayed in pictures b) and c) The table shows the compositions of those phases analyzed with the help of FE-SEM-EDS. Estimated mineral phases: 1 = Moncheite, 2 = Co-pentlandite, 3 = bornite with Ag, 4 = covellite, 5 = moncheite with no Pd, 6 = altaite with hessite, 7 = moncheite with altaite, 8 = moncheite with melonite, 9 = merenskyite-moncheite-melonite (ss), 10 = magnetite, 11 = violarite, 12 = Co-pentlandite becoming violarite, 13 = baddeleyite, 14 = magnetite.

Covellite contains minor amounts of silver in a crystal lattice in grains close to PGM and other tellurides including sopcheite**.** Sphalerite crystals are scarce, and only a few were found in three samples. It occurs close to ilmenite, with which it forms intergrowths, and also observed close to Pt-telluride and surrounded by serpentine.

3.1.3.4. Gold and silver

Although not abundant, silver and gold occur in native form and more commonly as electrum. These precious metals occur close to chalcopyrite and cubanite as inclusions relatively close to their rims. However, they were also observed separated from any sulfide and surrounded by olivine and serpentine. Electrum was also noted close to the previously mentioned Ni-bismuth phase (possibly badenite) and galena. Electrum crystals tend to be around 10 to 20 microns in size, with one exception of up to 100. Only one grain of native gold was found with subhedral to anhedral shape and surrounded by serpentine. Two grains of native silver were observed as anhedral inclusions within chalcopyrite and forming intergrowths with electrum and a Ni-bismuth phase. The larger native silver grain does not exceed 7 by 3 microns.

3.1.3.5. Oxides, sulfates and phospates

With the help of FE-SEM-EDS analysis it was observed that ilmenite crystals may contain abundant inclusions of magnetite and Co-pentlandite. Additionally, one 70 by 40 microns crystal of baddeleyite was detected in contact with magnetite (Figure 23f).
Barite commonly occurs within fractures of broken sulfides and oxides, such as chalcopyrite and chromite, sometimes related to galena.

Apatite was found in contact with chromite and showing intergrowths with chalcopyrite and what seems to be marcasite or pyrite. These apatite crystals represent the chlorine rich type, with no trace of fluorine or hydroxide.

3.2. X-ray computed tomography (XCT)

When doing X-ray computed tomography analyses is important to bear in mind some of the drawbacks of this technique: **a)** XCT is a qualitative method that needs to be complemented with other techniques in order to reach more detailed and quantitative results. It does not provide element composition of the mineral phases like SEM (scanning electron microscope) or EMPA (electron micro probe analyzer). Hence, it is fundamental to do at least a petrographic study of the samples so the obtained images and 3D model could be adequately interpreted. **b)** It is not possible to distinguish between phases with similar densities (e.g. With a difference of +- 1 g/cm^3) (Table 8). Therefore, the distinction between the majority of the sulfides and oxides is not possible. Considerably denser minerals such as PGM can be discerned from the sulfides and oxides.

Table 8. Oxides, sulfides and PGMs estimated densities. After Webmineral database.

	Mineral	Ideal Formula	Common substitutions	Density
Oxides	Chromite	$Fe^{2+}Cr_2O_4$		4.5 - 5.09
	Magnetite	$Fe^{2+}Fe^{3+}{}_2O_4$		5.175 – 5.2
Sulphides	Chalcopyrite	$CuFeS_2$		4.1 - 4.3
	Pyrrhotite	Fe_7S_8		4.58 - 4.65
	Pentlandite	$(Fe,Ni)_9S_8$		4.6 - 5
	Pyrite	FeS_2		4.8 - 5.2
Pt minerals	Braggite	(Pt,Pd)S	Ni	10
	Cooperite	PtS	Pd, Ni	9.5
	Isoferroplatinum	Pt_3Fe	Ru, Rh, Ir, Pd, Os, Cu, Ni	16.5
	Moncheite	$PtTe_2$	Pd, Ni, Sb	10
	Sperrylite	$PtAs_2$	Rh, Ir, Sb, S	10.58
Pd minerals	Braggite	(Pt,Pd)S	Ni	10
	Cabriite	Pd_2SnCu	Pt, Ag, Sb	11.1
	Isomertieite	$Pd_{11}As_2Sb_2$	Te	10.33
	Kotulskite	PdTe	Pt, Ni, Bi, Sb	8.26
	Merenskyite	$PdTe_2$	Pt, Ni, Bi, Sb	8.547
	Michenerite	PdBiTe	Pt, Ni, Sb	9.5
	Plumbopalladinite	Pd_3Pb_2	Ag, Cu, Bi, Sn, Sb	12.4
	Polarite	Pd(Bi,Pb)	Pt	12.51
	Stannopalladinite	Pd_5Sn_2Cu	Pt	10.2
	Sudburyite	PdSb	Ni, Te, Bi, As	
	Taimyrite	Pd_9Sn4Cu_3	Pt	15.6
	Vysotskite	PdS	Pt, Ni	6.7
Telluride	Melonite	$NiTe_2$		7.3

c) Sample size and resolution limitations. The higher the desired resolution, the longer the scan time, the smaller the dimensions analyzed and the higher the noise in the resulting image. Moreover, the machine has a precision threshold of eight voxels in size, therefore, any detected feature below that results unreliable. Thus, all grains with a size below that threshold, such as PGMs, were filtered out, resulting in an elimination no bigger than 2% of the total amount.

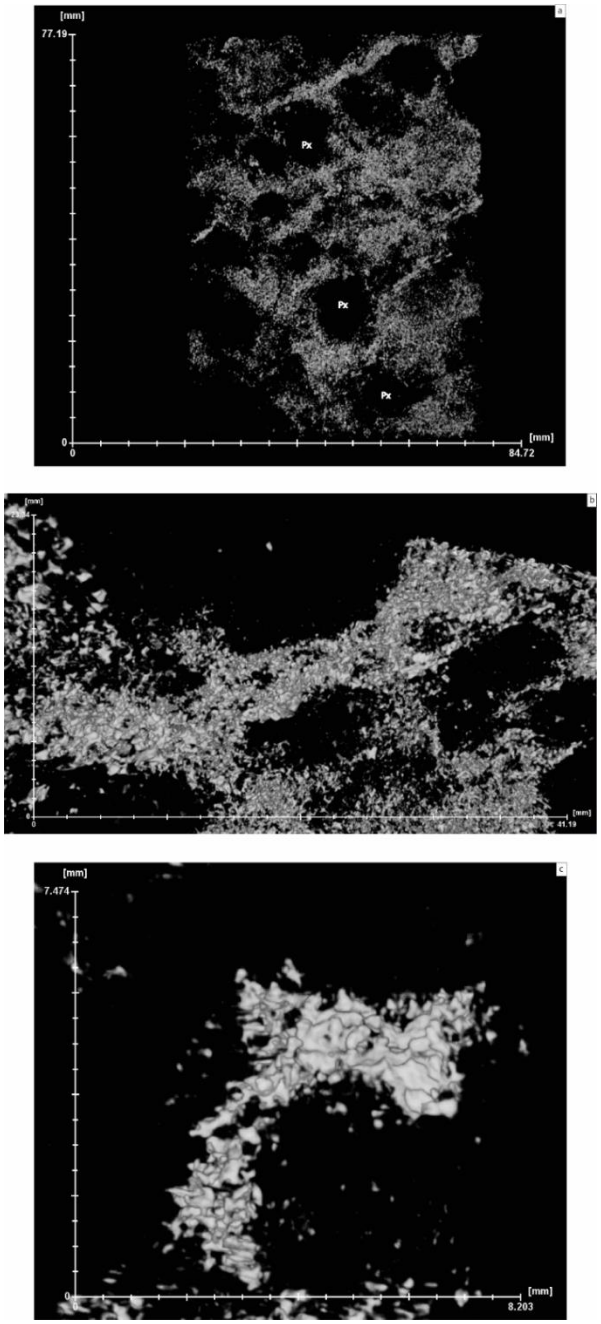

Figure 24. XCT backscattered images from sample CT01_PBF18 only showing the sulfides. (a) Entire view where is possible to see a certain degree of connectivity between sulfides. The spaces marked with Px represent pyroxene poikilitic grains. (b and c) More detailed view of the sulfides where connectivity between the grains can be seen.

The main objective of this analysis was to evaluate the potential that X-ray computed tomography has in the characterization of ore related mineralogy, structures and textures in a Ni-Cu-(PGE) magmatic deposit like Sakatti. Three samples were chosen (CT01-PBF18, CT02-PBF18 and CT03-PBF18) that represent from low to high Cu-grades of the disseminated ore within peridotite as a host rock. As general rule silicates have considerably lesser densities than oxides and sulfides which allowed to filter out all the silicate minerals leaving the denser phases visible.

The sample CT01-PBF18 from drill core 12MOS8090 is 130 mm by 50 mm in size. The aim for this sample was to study the degree of connectivity of the chalcopyrite dominated sulfides. Thus, the analysis was carried out in order to maximize the resolution without a significant compromise of the size of the sample analysed. This way a 70 by 40 mm portion was analysed achieving a resolution of 40 μm. Sulfide minerals occupy the intercumulus space and surround the poikilitic pyroxenes. This sample depicts a high Cu-grade disseminated mineralization. The sulfide phases in three dimensions show a significant degree of connectivity and wettability (Figure 24a,b,c), especially surrounding the pyroxene poikilitic grains, however, few sulfide grains are also found within these pyroxene blasts. Minerals with similar densities (Table 8), such as chromite, chalcopyrite, pyrrhotite, pentlandite, pyrite, etc. will not be able to be discerned. Using the three-dimensional model, it has been possible to visually distinguish phases significantly denser than these common sulfides and oxides (Figure 25). With the intention of quantifying these denser phases a histrogram was constructed, where the Y axis is the number of samples and the X axis represents the maximum attenuation value of each grain normalized to their respective volume. Thus, it is possible to compare the different grains independently of their volume (Figure 26). In this histrogram the grains with the lowest X-ray attenuation are the most abundant and their quantity decreases as the attenuation increases with no fluctuations until approximately 0.011. After 0.011 of X-ray attenuation it is possible to see approximately 3 spikes of the number of grains which may indicate the presence of several denser mineral phases.

The sample CT02-PBF18 with dimensions 125 mm by 50 mm was sampled from drill core 18MOS8222. It is an adcumulate-textured dunite. It represents a low Cu-grade disseminated mineralization with no apparent sulfide connectivity. The target for this

sample was to evaluate the degree of connectivity and discern possible denser phases such as PGM from the sulfides and oxides. Considering the small grain size of the ore minerals, the analysis was set to maximize the resolution. A 25 by 50 mm section was analyzed with a resolution of 15.07 µm. Sulfide grains in three dimensions turn out to have low connectivity (Figure 27a,b,c). Due to the higher resolution and with the aid of petrographic observations phases (Figure 27c), however, no anomalous denser minerals such as PGM were discerned. The histogram brings out seven anomalous spikes at higher attenuation values above 0.58 that may indicate the presence of denser phases (Figure 28).

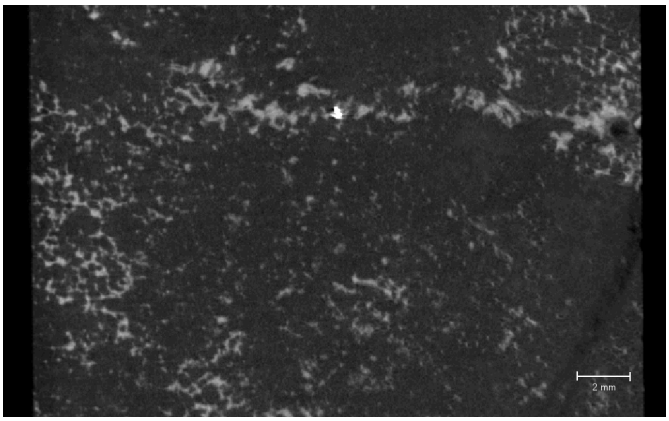

Figure 25. XCT backscattered image from sample CT01_PBF18. In black to dark grey are the silicates. Light grey represents the sulfides. White shows a considerably denser mineral phase than the sulfides around.

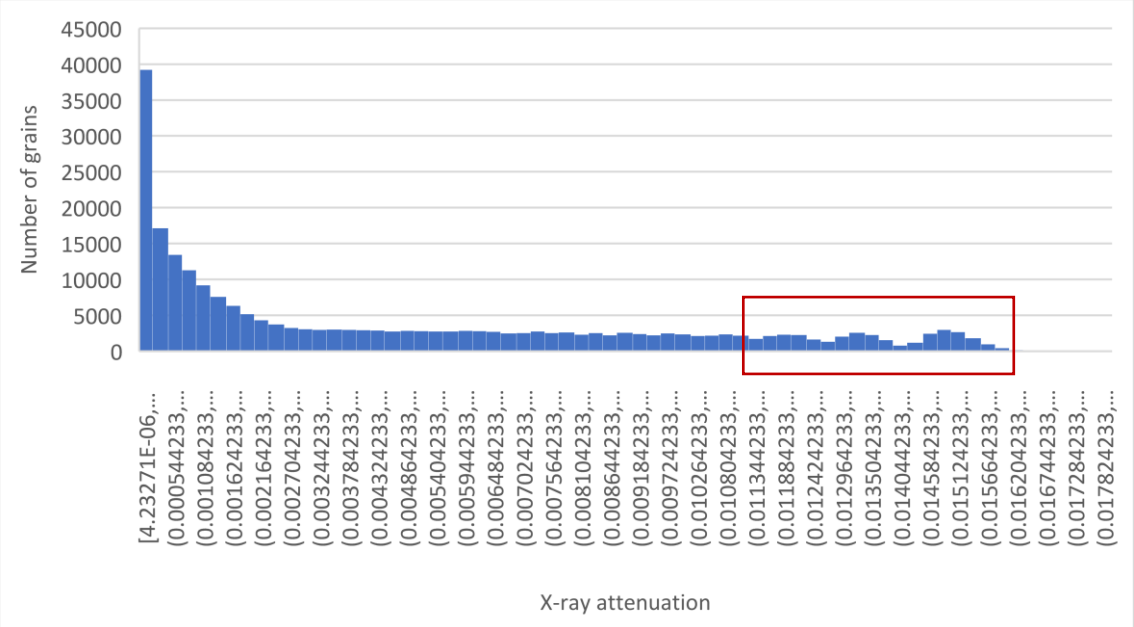

Figure 26. Histogram from sample CT01_PBF18 representing the number of sulfide grains detected for each X-ray attenuation interval. The red rectangle marks three clear spikes that differ from the general trend.

The sample CT03-PBF18 with dimensions 235 mm by 50 mm was sampled from drill core 18MOS8224. This sample represents a medium Cu-grade dissemination with the ore distributed in patches of sulfides. It is characterized by several carbonate and serpentine veins that seem to cause certain degree of remobilization of the sulfides. Thus, the aim for this sample was to study the sulfide and oxide textures in a bigger scale and how they are connected to structures such as veins. Consequently, the size of the scanned area was

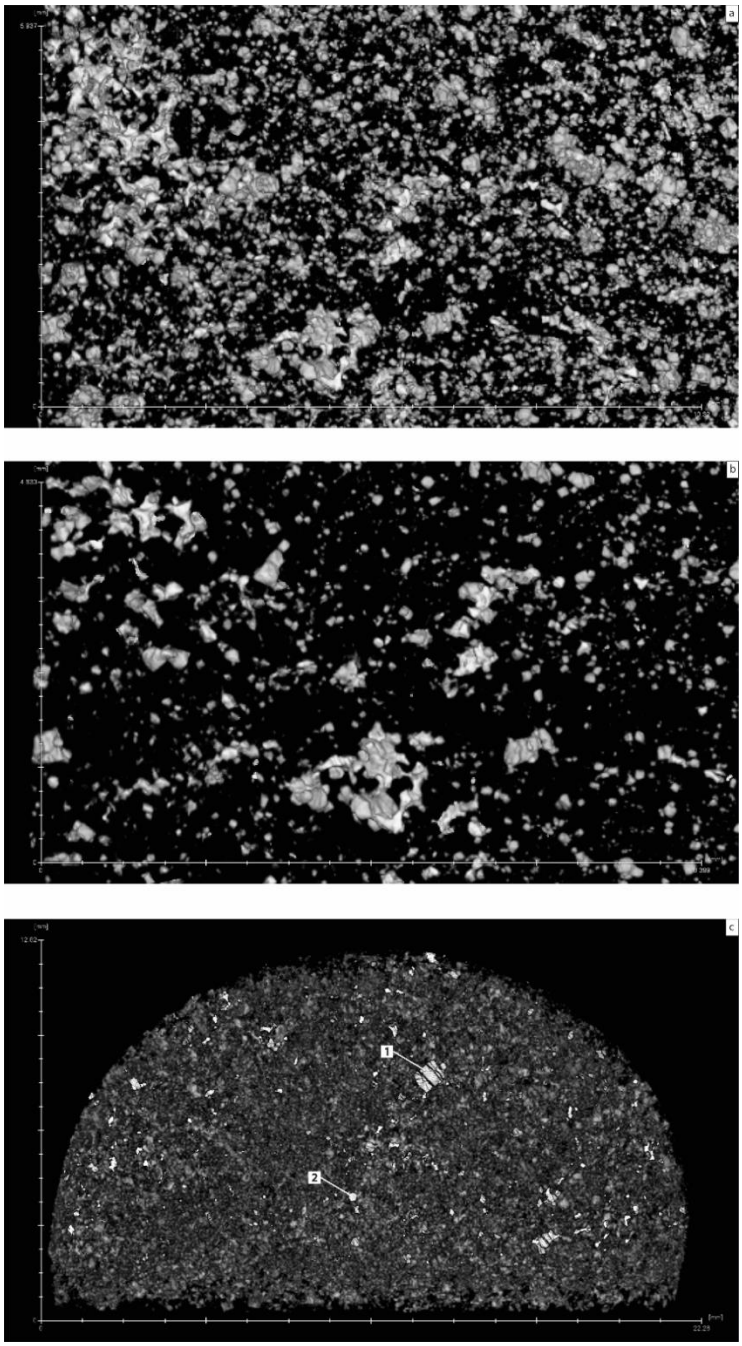

Figure 27. XCT backscattered images from sample CT02_PBF18 only showing the sulfides. (a and b) Detailed view showing the low connectivity between sulfides. (c) General view where is possible to discern some oxides from sulfides. 1 = Sulfide, 2 = oxide (possibly chromite)

maximized which translated into a lower resolution. The scan size was 224 by 42.5 mm and the resolution obtained was 117 µm. In Figure 29a is possible to see that the veins are filled with sulfides but no clear indication of intense remobilization of local ore minerals has been noted. A detail view of the widest serpentine-carbonate vein (Figure 29b) reveal that the sulfides filling this structure present a bigger grain size and higher X-ray attenuation than the surrounding ones. In terms of mineralogy, no anomalous denser minerals were found by visually studying the model. The histogram evidences three anomalous spikes in the number of samples towards higher attenuation values above 0.0016 that could indicate the presence of four mineral phases (Figure 30).

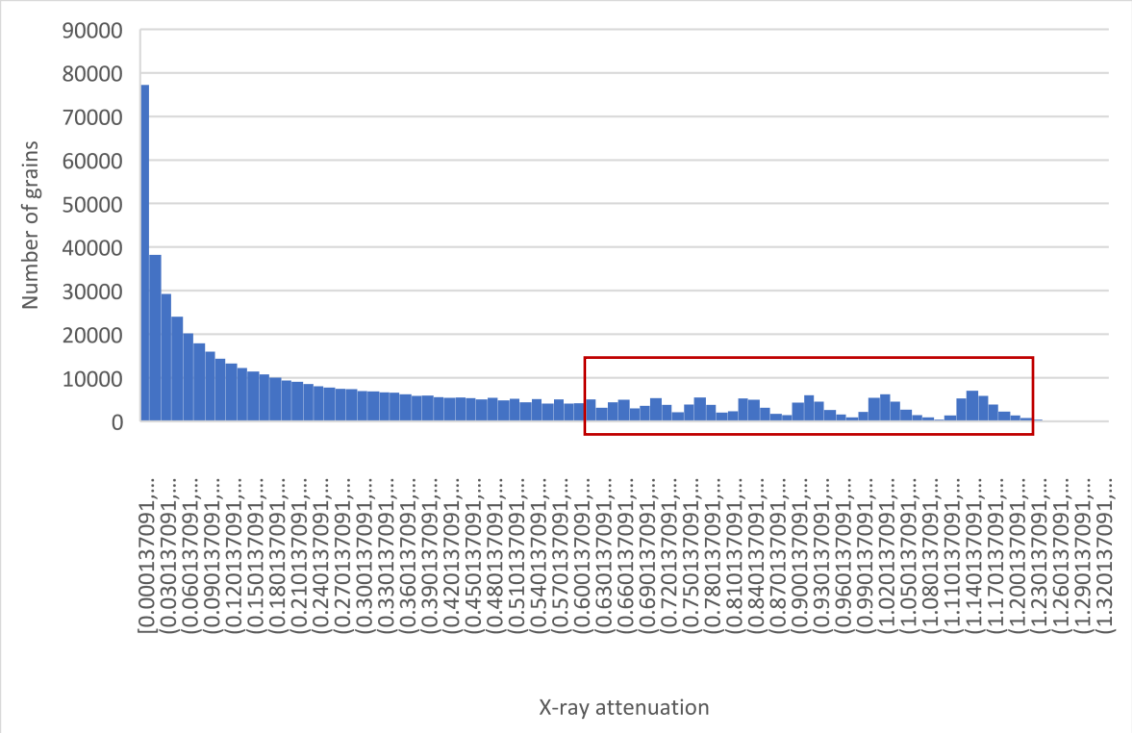

Figure 28. Histogram from sample CT02_PBF18 representing the number of sulfide grains detected for each X-ray attenuation interval. The red rectangle marks three clear spikes that differ from the general trend.

3.3. Chalcophile element composition

Base metals (Ni, Cu, Co), platinum group elements (Ru, Rh, Pd, Os, Ir, Pt), selenium, sulfur and gold were analysed from 19 chalcopyrite dominated disseminated ore samples. Additionally, another 19 massive sulfide geochemical samples from the NE and SW bodies were included in this study. In order to be able to use the data for geochemical characterization, it was fixed by substituting those values below the detection limit (BDL)

(Table 9 and 10) by BDL/√2. This measure it has been selected as the best method to produce the smallest error possible by Croghan and Egeghy (2003), and Verbovšek (2011).

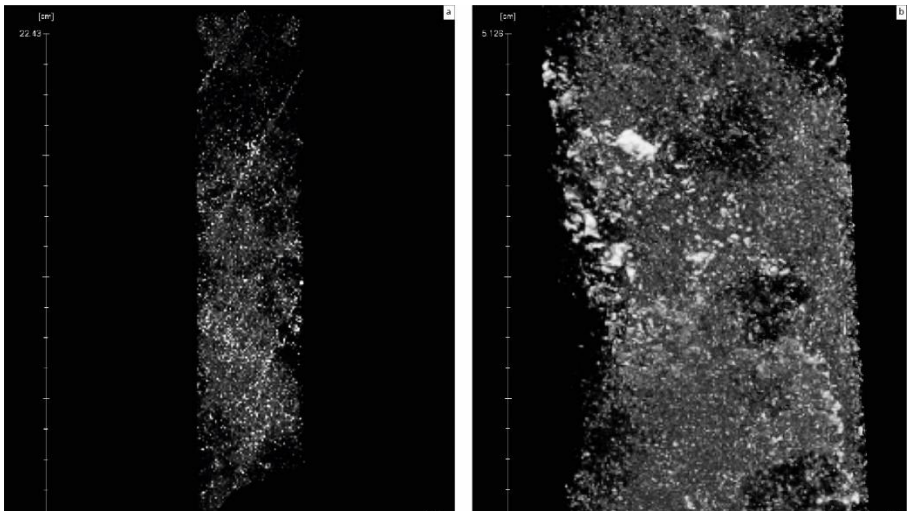

Figure 29. XCT backscattered images from sample CT03_PBF18 only showing the sulfides. (a) General view of the whole sample. (b) Detailed view showing one of the veins crossing the sample.

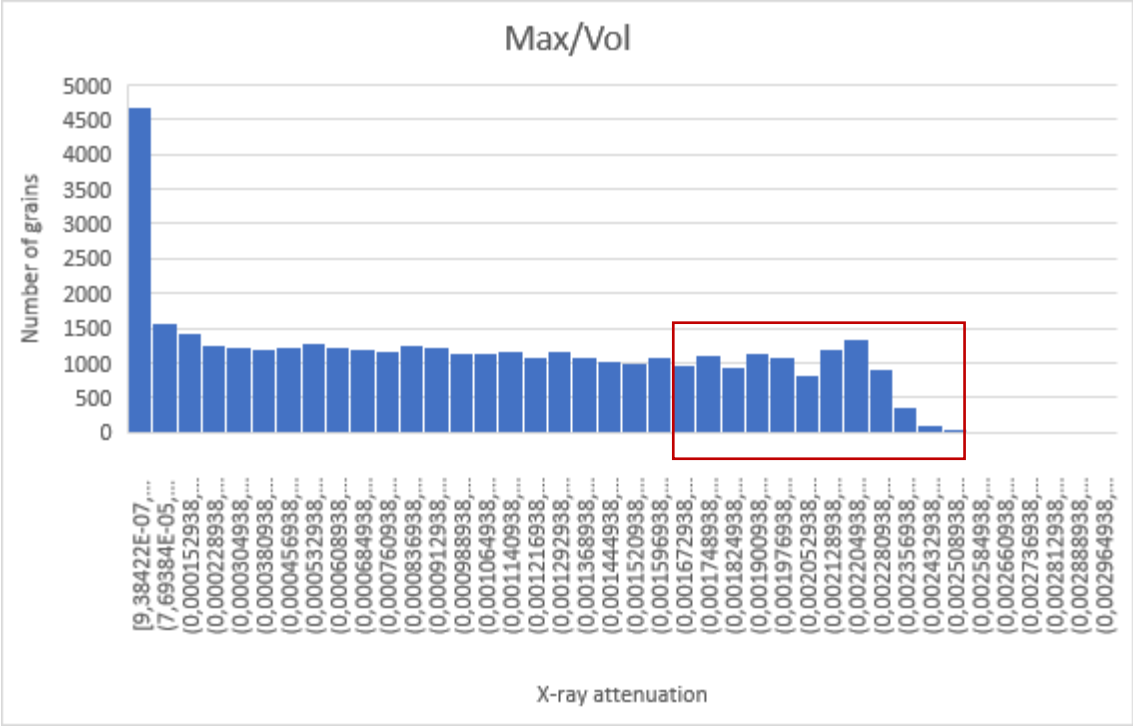

Figure 30. Histogram from sample CT03_PBF18 representing the number of sulfide grains detected for each X-ray attenuation interval. The red rectangle marks three clear spikes that differ from the general trend.

Two main types of diagrams were constructed to help in the interpretation of these data sets: spidergrams and ratio plots. First, the spidergrams are based on the abundancy

patterns of base metal, PGEs and gold normalized with primitive mantle values of (McDonough and Sun, 1995). The elements used are *Ni, Co, Os, Ir, Ru, Rh, Pt, Pd, Au and Cu*; and are set in a line graph from more compatible (left side) to more incompatible (right side) with the mantle during its melting (Barnes and Lightfoot, 2005, Rollinson 2014).

Table 9. Element content for the chemically analyzed disseminated ore samples.

	Au (ppb)	Co (ppm)	Cu (ppm)	Ir (ppb)	Ni (ppm)	Os (ppb)	Pd (ppb)	Pt (ppb)	Re (ppm)	Rh (ppb)	Ru (ppb)	S (%)	Se (ppm)
FMOS148702	149	114	15471	3	2076	4	802	553	X	2	8	1.98	22.6
FMOS148703	98	100	2572	2	2393	2	135	215	X	1	9	0.33	3.3
FMOS148704	256	151	8091	12	3701	18	224	367	X	2	33	1.41	11.9
FMOS148705	134	108	6230	2	2551	3	148	169	X	1	8	1.2	6.3
FMOS148706	554	109	4192	3	2478	2	537	1284	X	3	9	0.49	10.8
FMOS148708	45	121	3944	8	2219	3	58	96	X	4	13	0.85	3.7
FMOS148709	138	178	4908	10	3056	9	161	242	X	11	26	0.95	6.7
FMOS148710	174	93	5069	3	1363	3	206	318	X	1	6	0.59	6.2
FMOS148711	138	130	4024	2	3042	1	215	282	X	3	9	0.72	5.7
FMOS148713	42	155	9358	14	2117	9	118	189	0.007	19	13	1.92	8.8
FMOS148714	122	115	2600	3	2315	3	174	290	X	2	12	0.39	3.7
FMOS148715	326	103	4919	2	2729	2	75	228	X	1	8	0.51	3.9
FMOS148716	133	110	4487	3	1270	2	255	369	X	2	7	0.52	5.7
FMOS148718	176	130	6504	2	2611	2	152	271	X	1	6	0.93	5
FMOS148719	311	92	5665	3	1608	3	97	229	X	5	11	1.21	7.3
FMOS148720	183	147	5024	7	4193	15	205	317	X	2	16	1.07	8
FMOS148722	103	108	5552	1	2070	2	129	275	X	X	2	0.9	6.2
FMOS148723	358	143	6251	2	1951	X	88	466	X	1	10	1.04	6.9
FMOS148725	146	108	5505	1	2320	2	410	286	X	2	6	0.92	8.8

Notes: X = not detected

Secondly, the ratio plots comprised: **a)** *Ni/Cu vs Pd/Ir* and *Cu/Ir vs Ni/Pd*. Based on (Barnes and Lightfoot, 2005), these were used in order to obtain a broad image of which deposit type/s Sakatti would fit best, as they give an idea of the interpolation relationship between the host rock and sulfides plus how the sulfide separation process from the host rock occurred. **b)** *S/Se vs Pt+Pd*. This diagram was done according to the studies of (Queffurus and Barnes, 2015) and helps in getting an idea of the proportion of sulfides related to silicates (R factor), fractionation degree, possibility of sulfur contamination and metamorphic or hydrothermal alteration of the deposit itself. **c)** *Rh vs Rh/Cu* (Naldrett et al. 1999). With these plots it is possible to estimate the degree and path of the fractionation of the sulfide melt.

Table 10. Element content for the chemically analyzed massive ore samples from the NE and SW bodies.

	Au (ppb)	Co (ppm)	Cu (ppm)	Ir (ppb)	Ni (ppm)	Os (ppb)	Pd (ppb)	Pt (ppb)	Re (ppm)	Rh (ppb)	Ru (ppb)	S (%)	Se (ppm)
FMOS92052	83	3366	40550	150	1607	74	309	4410	0.102	213	60	40.76	69
FMOS92053	100	3690	43718	103	1681	48	145	1280	0.071	201	44	39.27	110
FMOS92055	61	2187	60338	36	18882	19	1466	5105	0.036	35	15	35.72	155
FMOS92056	38	3867	3131	117	38942	61	3253	2917	0.07	139	42	38.09	230
FMOS92057	27	2336	30394	44	76627	18	3527	2692	0.055	73	20	32.89	147
FMOS92059	50	1792	44778	12	76284	4	5459	2412	0.058	23	4	30.26	128
FMOS92060	16	1254	148428	14	47333	4	3606	2363	0.054	32	7	30.69	127
FMOS92061	297	2922	21403	140	20313	57	2199	2124	0.091	116	65	34.23	132
FMOS92062	20	1600	71692	2	10861	3	536	1675	X	X	6	34.95	122
FMOS92063	51	1698	25380	35	84861	13	2439	1798	0.045	64	13	30.72	122
FMOS92065	68	2979	10014	57	15854	25	1050	1635	0.07	99	47	40.16	165
FMOS92066	562	2356	72800	42	18980	16	2096	3826	0.066	63	20	37.41	164
FMOS92067	34	1679	3914	359	16350	163	321	393	0.012	236	210	15.54	147
FMOS92068	148	255	4735	4	3560	4	245	400	0.005	6	6	2.98	16
FMOS92069	35	4634	13443	115	44223	54	870	707	0.134	100	83	40.56	55
FMOS92070	9	3253	4610	253	27055	169	461	735	0.311	128	279	37.2	99
FMOS92072	61	2078	9063	188	66984	99	1262	705	0.137	139	148	31.8	85
FMOS92073	481	2041	32533	10	4245	7	411	822	0.081	15	8	28.23	94
FMOS92074	26	948	2499	16	41933	8	892	783	0.038	23	13	27.8	120

Notes: X = below detection limit

3.3.1. Base metal, platinum group elements and gold spidergrams

The metal contents were recalculated to 100% sulfide content and normalized to mantle values. By normalizing these chalcophile elements it will be possible to compare their distribution relative to each other (Barnes and Lightfoot, 2005). Moreover, the plotted data will be more even than unnormalized one which help in its interpretation (Naldrett and Duke, 1980) (Figure 31a, b and Figure 32a, b). Pd/Ir can be used as the expression of the slope of the trend (Barnes et al. 1985).

The average disseminated ore sulfides (Figure 31a) shows a general positive slope with increasing values from Ni being 12 times richer than the mantle, to Au and Cu being almost 10000 times more enriched than the mantle. This general trend can be divided into two different slopes. First, from Ni to Rh pattern is characterized by a positive slope only reaching a maximum of 144 times mantle values for Rh. Second, the pattern formed by Pt to Cu denotes a steeper slope with values that oscillate from approximately 2200 times

mantle values for Pt to 8600 times mantle values for Au. Moreover, Os, Pt and Au show a positive spike compared to the general trend of these chalcophile elements.

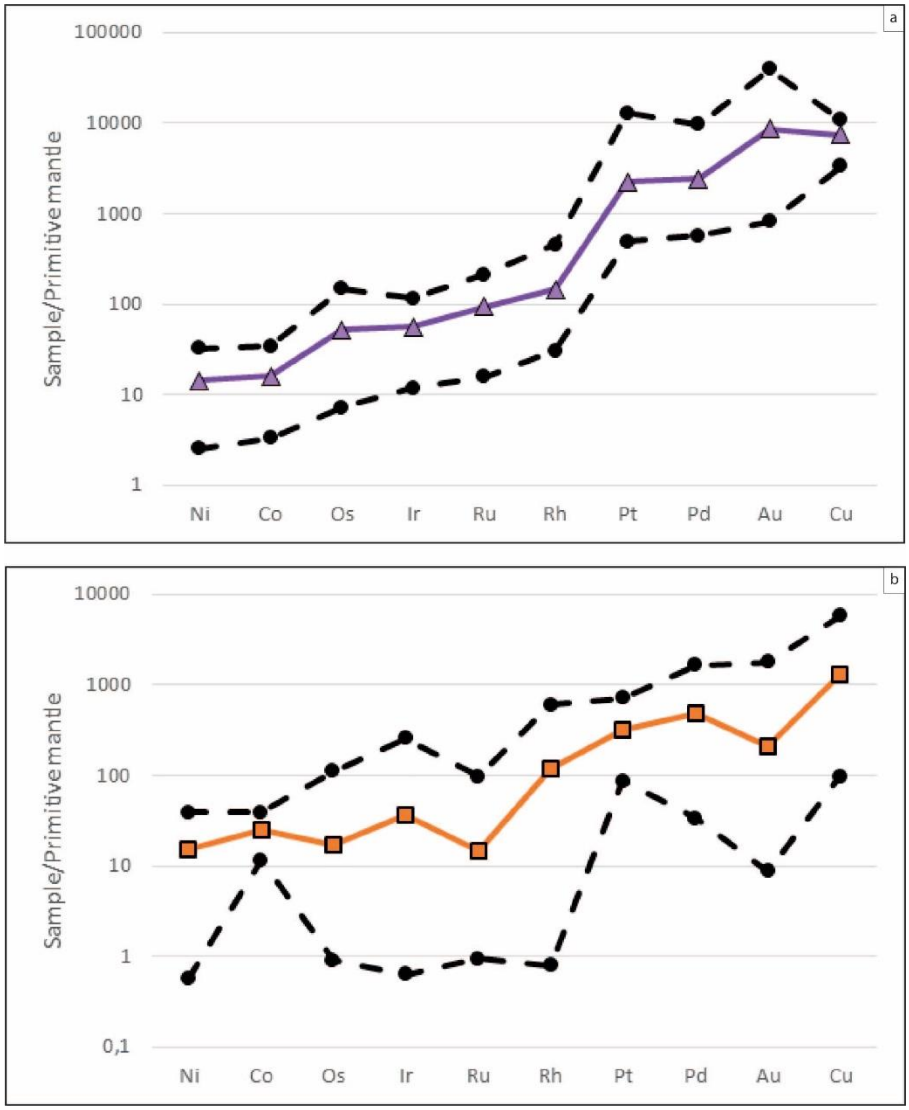

Figure 31. All data has been recalculated to 100 % sulfides and mantle normalized. (a) Spidergram representing the average disseminated ore values in purple, and the maximum and minimum values with dashed lines. (b) Spidergram representing the average values from the massive ore in the NE and SW bodies in orange, and the maximum and minimum values with dashed lines.

The average of massive sulfides from the NE and SW bodies (Figure 31b) presents a less steep slope than the disseminated samples. Element enrichment compared to mantle values are approximately 15 for Ni and 1300 for Cu. Overall, the slope of the average values shows a positive growth without major anomalies, however, Os, Ru and Au, especially the last two, exhibit a depletion when compared to the general trend. On one side, the maximum values trend within the NE and SW bodies massive ore approximately

follow the average. Although, no depletion of Os can be seen compared to the general pattern. Ni shows a certain enrichment and Pt slight depletion when compared to the average. On the other side, the minimum values for Ni, Os, Ir, Ru, Rh show a significant anomalous depletion reaching below mantle values.

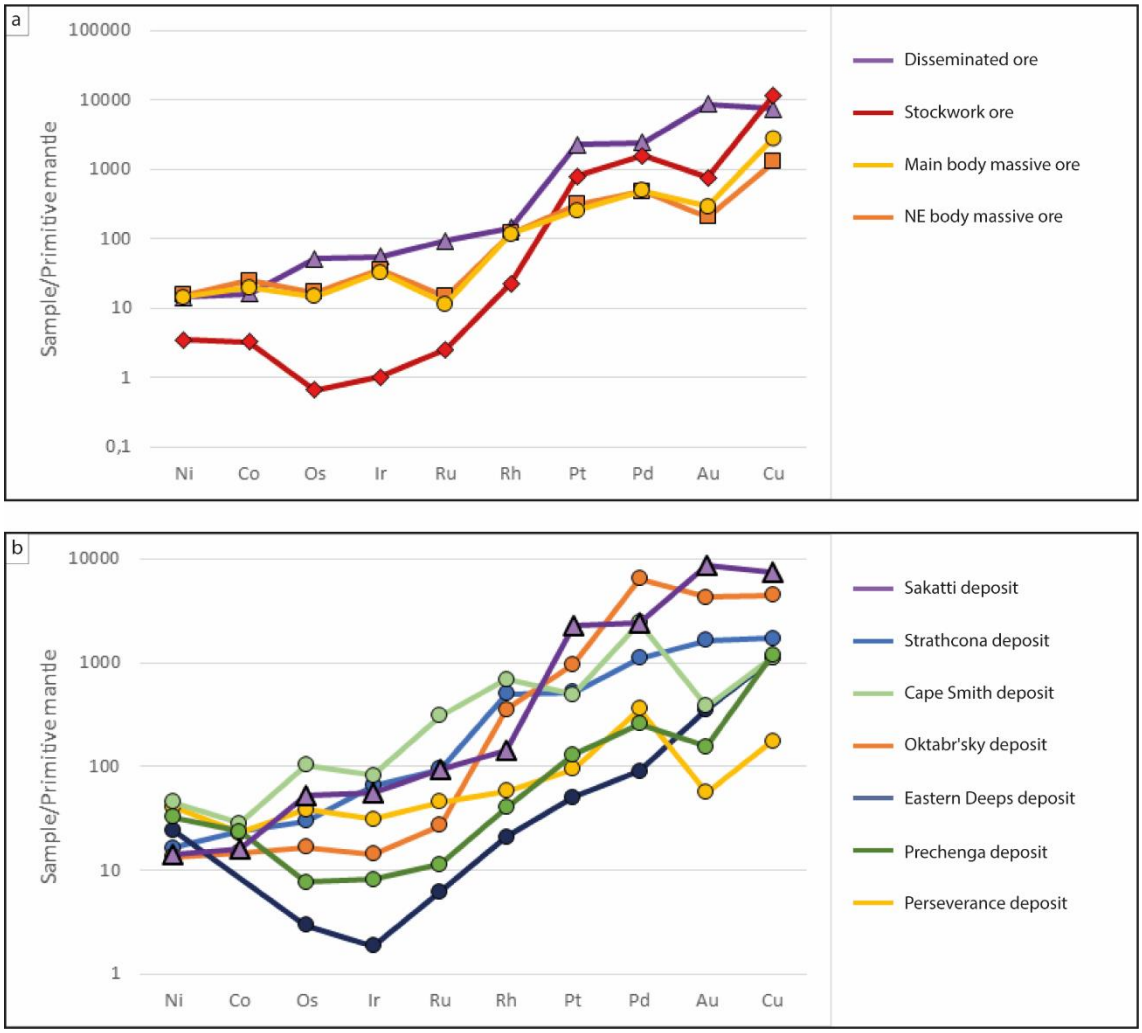

Figure 32. All data has been recalculated to 100 % sulfides and mantle normalized. (a) Spidergram containing the three major ores in Sakatti. (b) Spidergram where disseminated ore samples from different major Ni-Cu-(PGE) magmatic deposits have been plotted (Barnes and Lightfoot, 2005), including Sakatti.

A comparison of the average values of the different ore styles within the Sakatti deposit can be seen in Figure 32a. While the massive sulfides from the NE and SW bodies and Main body present a very similar patterns between them, the disseminated and stockwork ores yield very distinctive patterns. The stockwork trend shows a clear depletion in IPGE with Os reaching values below mantle content, and a drastic enrichment in PPGE (Rh, Pt

and Pd), Cu with a depletion in Au (Fröhlich 2016). The disseminated ore has similar values to the massive ores from Ni to Rh and a similar trend to the stockwork ore from Pt to Cu. The content from Pt to Cu increases noticeably in the disseminated ore compared to the massive sulfides and becomes the ore with the highest content in Pt, Pd and Au of the Sakatti deposit. The disseminated mineralization shows a depletion in Pd and Cu, and an enrichment in Au compared to the stockwork ore.

When comparing the element signature of the disseminated ore in Sakatti to other disseminated ores of well-known Ni-Cu-(PGE) deposits (Figure 32b), disseminated ore of Oktabr'sky deposit from Norilsk-Talnakh shows a similar overall pattern.

3.2.2. Diagnostic chalcophile element ratios: Ni/Cu vs Pd/Ir and Cu/Ir vs Ni/Pd

These diagrams are used to better understand the relationship between the sulfides and the host rock. Moreover, they are also indicative of the sulfide segregation. By plotting data from extensively studied and properly classified deposits, Barnes and Lightfoot (2005) established approximate constrained areas for different kinds of host rocks. These authors also included an estimated compositional range for Cu-rich sulfide veins as they don’t show a strict genetic relationship with their host rock.

Disseminated ore, and NE and SW bodies massive samples were plotted together with data from the Main body massive sulfides (Ahvenjärvi 2015) and stockwork vein ore (Fröhlich 2016) (Figure 33a,b). Average values of these ore styles are indicated as green symbols.

Disseminated samples mostly occur outside of any host rock ranges, nevertheless, few of them fit within the rims of the Cu-rich sulfide veins, flood basalts and layered intrusions areas (Figure 33). The disseminated ore Ni/Cu, Pd/Ir and Cu/Ir ratios show similar values to the massive sulfides from the Main body, and NE and SW bodies. In the Cu/Ir vs Ni/Pd diagram, the disseminated ore has some samples with values similar to the massive and stockwork sulfides, however, the rest follow a distinctive trend towards lower Ni/Pd and higher Cu/Ir.

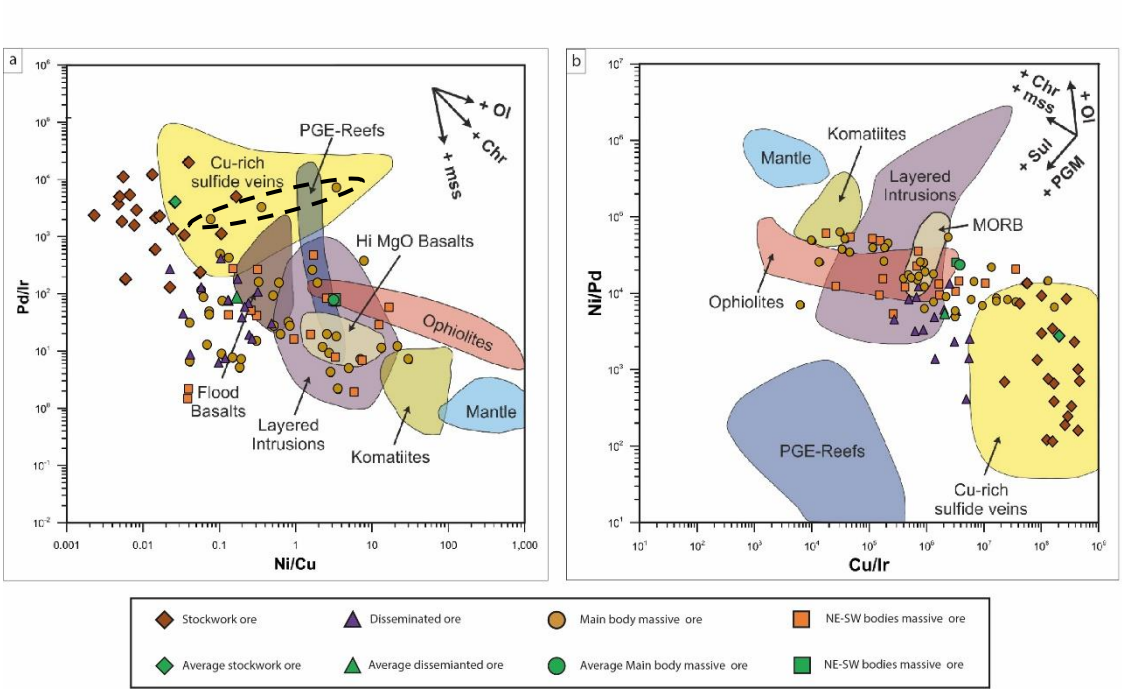

Figure 33. (a) Ni/Cu vs Pd/Ir diagram with all the major ore types from Sakatti plotted and their average values. The three massive sulfide samples within the dashed ellipse were proven to be anomalous by Fröhlich (2016) so they were excluded for the average calculation of that ore type. (b) Ni/Cu vs Pd/Ir diagram with all the major ore types from Sakatti plotted and their average values. The samples were recalculated to 100 % sulfides. Diagrams modified after Barnes and Lightfoot (2005) and Fröhlich (2016).

Massive sulfide samples from the NE and SW bodies fall within the compositional fields of high MgO basalts, layered intrusions, ophiolites and flood basalts (Figure 33). Only a few samples plot within the field of komatiites. Some of the samples fall outside of any host rock type area towards lower values of Ni/Cu, Pd/Ir and higher Cu/Ir and Ni/Pd. In general, NE and SW bodies massive ore present a considerably similar Ni/Cu vs Pd/Ir and Cu/Ir vs Ni/Pd ranges to the Main-Body massive sulfides (Ahvenjärvi 2015). Overall, the massive sulfide ore has a larger compositional spread than the disseminated and stockwork ores.

In the Ni/Cu vs Pd/Ir diagram (Figure 33a), the disseminated ore average plots at the boundary of the flood basalts field. In the Cu/Ir vs Ni/Pd diagram (Figure 33b), the disseminated ore average plots in the border of the layered intrusions domain. The stockwork mineralization average falls into the Cu-rich sulfide veins region in both diagrams. The massive mineralizations average fit into the layered intrusion compositional field, close to the boundary with the PGE-reef area, in the Ni/Cu vs Pd/Ir

diagram. In the Cu/Ir vs Ni/Pd plot the massive sulfides average is in the boundary of the ophiolites close to the layered intrusions field.

At Ni and Cu diagram (Figure 34a) it is possible to see an approximately progressive evolution from massive sulfides, through disseminated ore to the most Cu-rich stockwork veins ore samples. The disseminated ore has a low Cu spread below stockwork ore values and Ni values similar to the massive ores. The stockwork ore shows a low spread in Cu content, while the Ni values go from lowest of all ore types to massive ore like values. In the Ir versus Pd plot (Figure 34b), some of the NE and SW bodies massive sulfides present a slightly lower Pd than the Main body massive mineralization. The disseminated and the stockwork vein ores have similar Pd content, however, their Ir content set them apart. In the Ir vs Pd plot (Figure 34b), the stockwork ore seems to form a negative slope with the massive sulfides, while the dissemianted mineralization is concentrated in a distinct area separated from the other two ores.

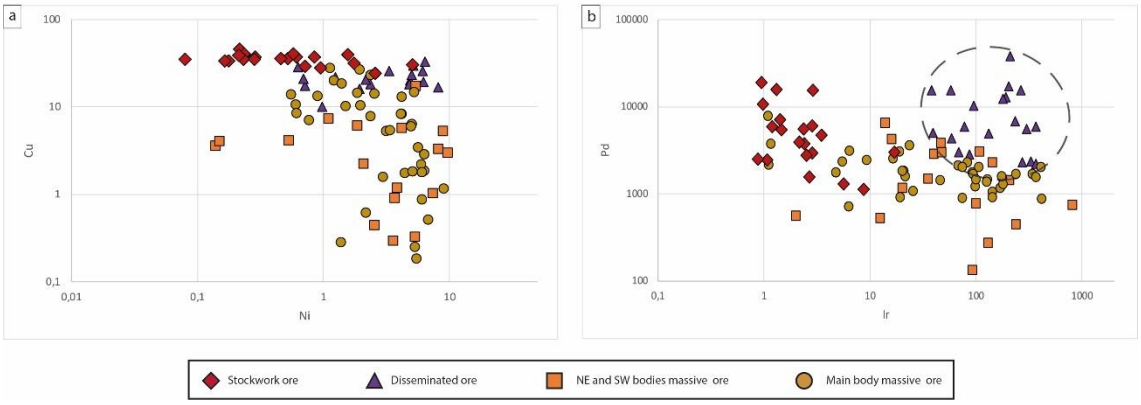

Figure 34. (a) Ni vs Cu diagram with all the major ore types from Sakatti plotted. (b) Ir vs Pd diagram with all the major ore types from Sakatti plotted. Dashed black circle emphasizes the disseminated ore distinct area. Samples have been recalculated to 100 % sulfides.

3.3.3. R-factor diagram: S/Se vs Pt+Pd

This diagram provides useful information regarding the R-factor, its relations with the fractionation of the sulfide liquids and the typical ranges of S/Se and Pt+Pd for MSS and ISS. It also gives information regarding possible hydrothermal alteration and metamorphism. Additionally, it could point to sulfur contamination of the system if S/Se ratios are above mantle values, or to S-loss in case these ratios are below 3800 (Queffurus

and Barnes, 2015, Smith et al. 2016). As a general rule, S/Se ratios of magmatic sulfide deposits vary from ~100 to ~100,000. However, a wide range of S/Se ratios and $(Pt+Pd)_{100\% S}$ values may occur within a single deposit due to different ore textures and compositions (Queffurus and Barnes, 2015).

Processes that may affect the S/Se ratios have been classified by Queffurus and Barnes (2015) into magmatic and late- to post-magmatic processes. Such magmatic processes can be: 1) addition of S due to crustal assimilation into the system; 2) Se depletion in the silicate magma due to an early partition of this element into the sulfide liquid; and 3) variations in the R-factor (silicate melt to sulfide melt ratio). In the case of the late- to post-magmatic processes, high-grade metamorphism and hydrothermal alteration including low temperature events such serpentinization and supergene enrichment can trigger changes in this ratio.

The disseminated sulfides, and massive sulfide samples from the NE and SW bodies have been plotted on Figure 35 together with the Main body massive sulfides from Ahvenjärvi (2015) and stockwork veins samples from Fröhlich (2016). In addition, samples from Oktyabr`sk, Norilsk Talnakh and McCreedy East, Sudbury (Czamanske et al. 1992) are shown for comparison.

The disseminated sulfides range from massive values to the ISS compositional zone, with the bulk of the samples close or within the latter (Figure 35). The disseminated ore has a higher overall content in $(Pt+Pd)_{100\% S}$ than the stockwork mineralization.

The NE and SW bodies massive sulfides show similar values to the Main body massive sulfides but with greater scattering. The bulk of the massive mineralization, from NE and SW bodies, seems to be divided into two populations, a less fractionated part with closer to mantle domain values, and another with a more fractionated compositions, below mantle values, that fall closer to the ISS field.

The stockwork vein sulfide samples (Fröhlich 2016) show a similar trend as the disseminated ore but with a higher scattering and overall lower $(Pt+Pd)_{100\% S}$. Some of the samples are within the ISS area but the bulk of the samples fall outside of any

compositional field. Five samples of the stockwork ore show S/Se and $(Pt+Pd)_{100\% S}$ values that lay within the high-grade metamorphism area.

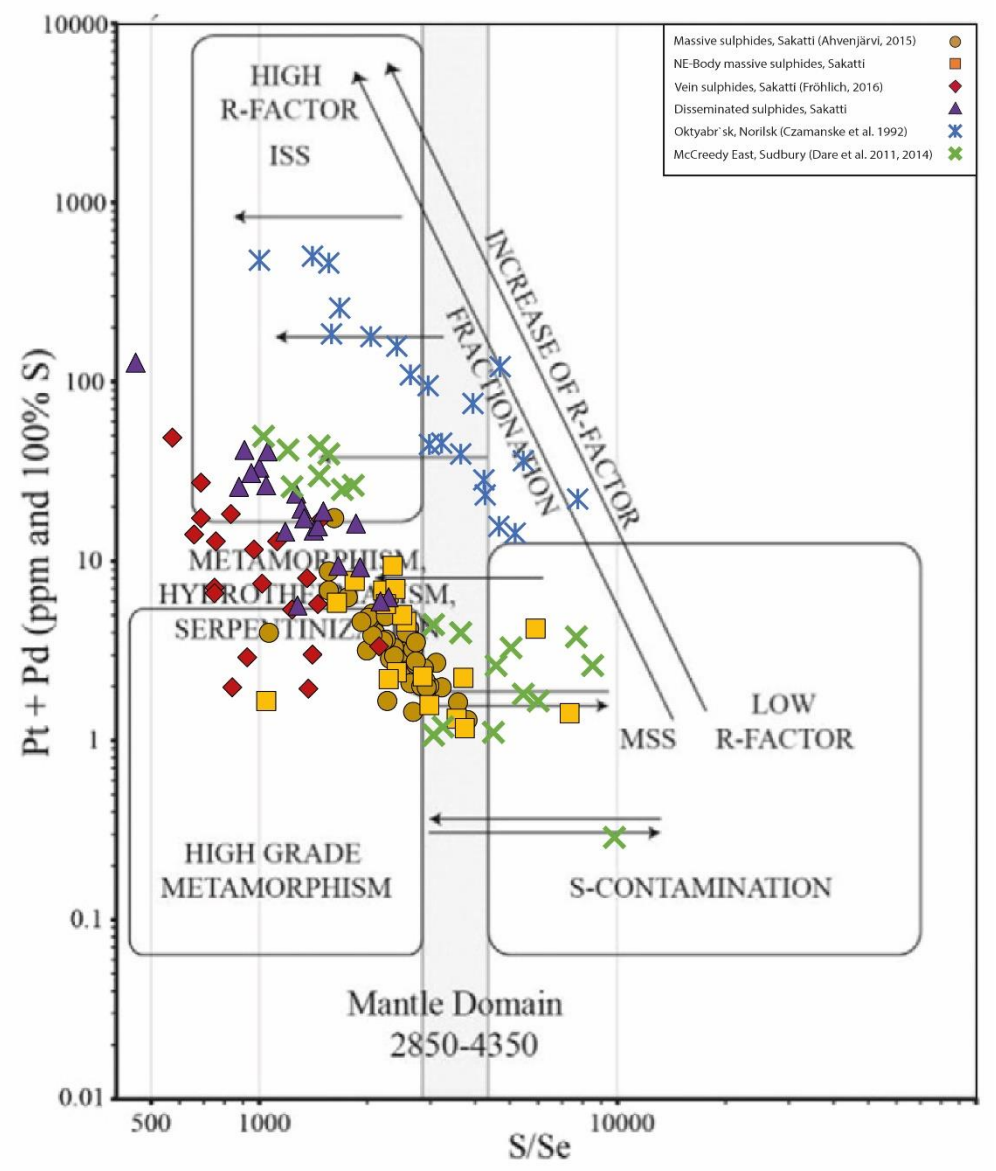

Figure 35. S/Se vs Pt+Pd diagram with all the major ore types from Sakatti plotted, plus Oktyabr`sk and McCreedy East deposits. Samples have been recalculated to 100 % sulfides. Diagram after Quefurus and Barnes (2015).

An overall negative slope can be seen at deposit scale but also within each ore type. This is also visible in the other deposits used for comparison, being most evident in the Oktabr'sky deposit. The general pattern is of a decreasing S/Se ratio and increasing $(Pt+Pd)_{100\% S}$ as the fractionation of the sulfide melt evolves. The least fractionated samples from the Sakatti deposit fit with the Main body massive samples and with the

NE and SW bodies massive ore. The disseminated ore samples have an overall slope trend and inclination that seem to represent the natural continuation of the fractionation path from massive sulfides towards lower S/Se ratios and higher $(Pt+Pd)_{100\% S}$. The stockwork vein sulfides (Fröhich 2016) also clearly reflect high degree of sulfide fractionation but their systematically lower $(Pt+Pd)_{100\% S}$ separates them from disseminated mineralization. The general trend of the Sakatti ores is similar with that of the Oktyabr`sk deposit. It shows a negative slope with very similar progression of S/Se ratios from less to more fractionated samples. In the case of the McCreedy East deposit, similar fractionation is evident, but there is a clear gap between the less fractionated samples and the more fractionated ones. Nevertheless, the content of the samples in McCreedy East is closer to the ones from the Sakatti deposit than the samples from the Oktyabr`sk deposit.

3.3.4. Sulphide fractionation: Rh vs Rh/Cu

By using the Sudbury deposit as a frame of reference, Naldrett et al. (1999) demonstrated that is possible to follow the fractional crystallization process of sulfide melts with a log-log plot of Rh versus $Rh/Cu*10^7$. Moreover, they also stated that variations in the Rh/Cu ratio while having constant values of Rh will denote changes in the proportions of the MSS, ISS and the liquid.

The progression of the fractionation can be followed with the slope defined by Rh vs. $Rh/Cu*10^7$. The crystallization starts with the formation of MSS in which process Naldrett et al. (1999) assumed that the partition coefficients of Rh and Cu between MSS and the residual liquid would approximately be 4 and 0.05 respectively. In Figure 36, continued fractional crystallization of MSS will be reflected in the diagram by the evolution of the heavy solid line for the liquid and the heavy dashed line for the MSS. Mixtures of MSS and the coexisting liquid lie in between the two path lines. The mono-sulfide solid solution and liquid fractionation lines terminate when around 89 % of the original liquid has crystallized and the remaining liquid reaches around 32 wt. % of Cu and 0.348 ppb of Rh while the MSS show 1.6 % of Cu and 1.39 ppb of Rh (Ebel and Naldrett 1996a, Ebel and Naldrett, 1997, Fleet et al. 1993, Fleet and Pan, 1994, Li et al. 1996, Naldrett et al. 1999). At this point approximately, the ISS will begin its crystallization, which will cause a shift in the compatibility of Rh and Cu in relation to

the newly created solid and the remaining liquid. Here the Rh will become incompatible while Cu significantly compatible with ISS, thus, Rh content will start to build up again in the residual liquid and Cu will start crystallizing. The trend of the Cu-ore fractionation will be noted by the black dotted line. The green solid line marks the path of possible mixing between the unfractionated MSS and the unfractionated liquid, while the purple solid line links the fractionated MSS with the fractionated liquid.

As the Cu content builds up in the residual liquid while the MSS crystallizes, the wettability of the sulfide liquid with respect to the silicates increases. This together with gravity and deformation could lead to the separation of the fractionating liquid from the MSS, leaving behind a dry MSS. This migrating liquid will lead to the formation of a solid dominated by ISS Cu-rich veins that could be cutting the previously formed MSS cumulates. This could also lead to the mixing of the more fractioned veins with the less fractionated MSS, marked in Figure 36 by the light blue solid line.

In that diagram, the massive sulfide samples from the NE and SW bodies of this study form a noticeably similar compositional trend to the Main body samples of Ahvenjärvi (2015). The most unfractionated sample of the NE and SW bodies massive ore has 444 of $Rh/Cu*10^7$ and 139 ppb of Rh that equals to 0.31 wt% of Cu and fit with the MSS fractionation path. As the fractionation progresses and the Sakatti MSS keeps forming, several massive samples from the NE and SW bodies are observed to lie in between the MSS and the residual liquid. Also, several of these samples are found within the path of the fractionating liquid.

The disseminated samples seem to depict more evolved compositions within the MSS as all the samples lie approximately at the end of the fractionating path of the MSS. Some of these even reach values such as a $(Rh/Cu)*10^7$ ratio of 1.29 and a Rh content of 2 ppb which equates to 1.55 wt. % of Cu. This drives the Cu and Rh content in the residual liquid extremely close to the limit established by Naldrett et al. (1999) before the ISS starts forming (32 wt. % of Cu and 0.348 ppb of Rh).
Based on the data given by Naldrett et al. (1999), the McCreedy East deposit shows a more similar trend with the one observed in the Sakatti deposit (Figure 36b). Both deposits have most of the MSS in between the MSS fractionation path and the residual

liquid path. Moreover, each of them also contains a Cu-rich vein ore, which predominantly falls in between the residual liquid and ISS fractionation path. Nonetheless, the disseminated ore from Sakatti seem to not fit with the McCreedy East or any other deposit within Sudbury

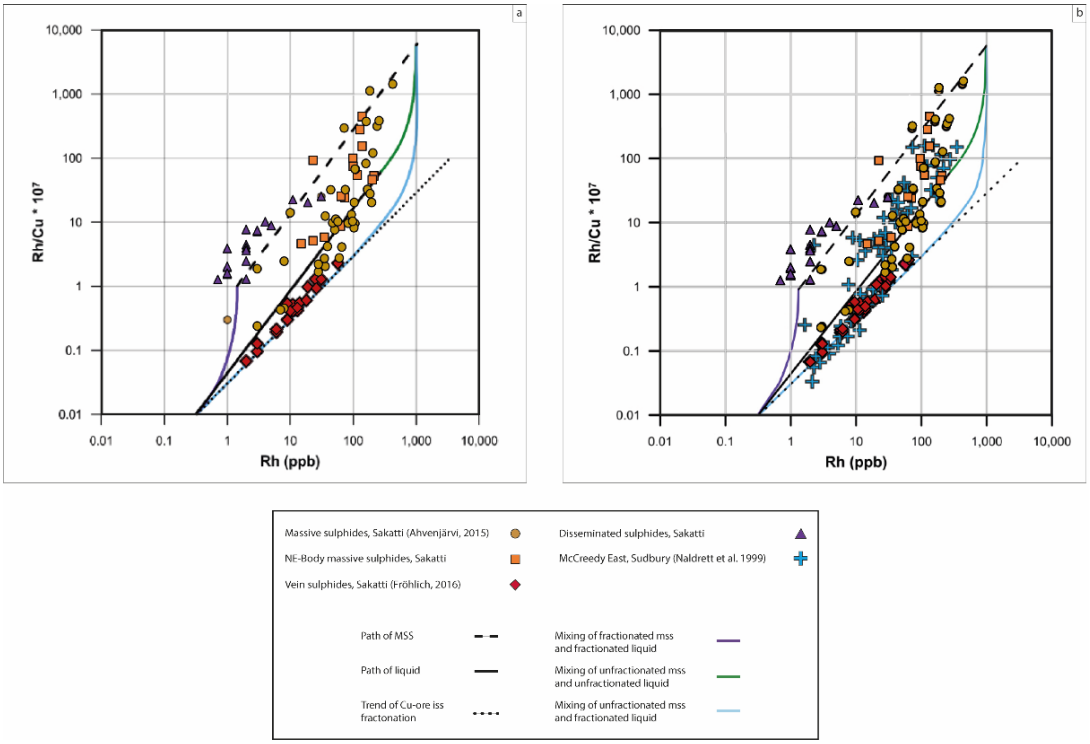

Figure 36. (a) Rh vs Rh/Cu diagram with all the major ore types from Sakatti plotted. (b) Rh vs Rh/Cu diagram with Sakatti and McCreedy East ores plotted for comparison. Modified after Naldrett et al. (1999) and Fröhlich (2016).

4. DISCUSSION

4.1. Sulfide mineralogy of Sakatti disseminated ore

The disseminated ore occurs predominantly as patches with low connectivity between them. Such texture has been primarily attributed to the process of percolation which is controlled by capillary and gravity (Barnes et al. 2017). The wettability of the sulfides plays an important role in the degree of capillary. The process of percolation would have been self-reinforcing as the migration of sulfides caused the sulfides droplets to grow by coalescence which would have led to a bigger gravitational pull for percolation and silicate melt displacement.

The disseminated mineralization at Sakatti consists of chalcopyrite, pyrrhotite and pentlandite as the main primary sulfide phases, with chalcopyrite being the predominant one. Pyrite is present in small amounts. Platinum group minerals are tellurides and bismuth-telluride phases, the merenskyite-moncheite-melonite series being the most abundant, followed by michenerite and sopcheite (Figure 22). Overall, there is a significant degree of alteration affecting the disseminated primary mineralogy, which becomes more intense towards the shallower parts of the deposit. This will be further addressed below, in section 4.4.

The chalcopyrite presents a considerable wettability around the olivine cumulate crystals and pyroxene poikilitic grains, but it is also found as inclusions within the latter. This implies that at least part of the disseminated mineralization formed coevally with the poikilitic grains. Chalcopyrite shows intergrowths with pyrrhotite and pentlandite crystals (Figure 16), and sometimes engulfs some of these crystals. These textural relations could suggest ISS migration, marked by the chalcopyrite injecting into the MSS as represented by the pyrrhotite and pentlandite.

The presence of NC pyrrhotite as inclusions within the most common 4C pyrrhotite may be explained by a local increase in the Fe atomic percentage causing both types of pyrrhotite to crystallize at the same time (Figure 17) (Wang and Salveson, 2005). Nickeloan pyrrhotite is stable at high temperatures, where some atoms of nickel occupy structure positions of iron (Becker et al. 2010). Generally, as the temperature decreases and pentlandite becomes stable, it starts to exsolve from the Ni-rich pyrrhotite (Francis and Craig, 1976). Nevertheless, if the cooling occurs rapidly, Ni-rich pyrrhotite may remain as a metastable phase. Thus, it may be indicative for those units of the deposit that have experienced rapid cooling. This mineral was found in samples TS07 and TS31, which represent deeper parts of the Main body.

According to the FE-SEM-EDS analysis, pentlandite commonly has some cobalt in its structure in some cases being cobalt-pentlandite. This agrees with the Co mainly partitioning into the earlier formed MSS (Dare et al. 2014). Additionally, it could also point to a re-equilibration process that may have caused the diffusion of cobalt from chalcopyrite to pentlandite (Barnes et al. 2006).

Several euhedral pyrite crystals associated with chalcopyrite and being unrelated to pentlandite (Figure 21) may represent primary pyrite. Craig (1973) and Naldrett et al. (1967) showed that pyrite cannot co-exist with pentlandite until 230 ºC to 212 ºC within MSS phases. Consequently, Dare et al. (2011) postulate that either pyrrhotite and pentlandite exsolved from the MSS at 650 ºC to 230 ºC and then pyrite exsolved below 230 ºC or pyrrhotite and pyrite exsolved from 700 ºC to 230 ºC and pentlandite started exsolving below 230 ºC. Considering the idiomorphic nature of some of these pyrite crystals, a late stage formation seems unlikely. Therefore, taking into account this and previous observations in massive and stockwork vein ores (Ahvenjärvi 2015, Fröhlich 2016), it can be argued that during the formation of pyrrhotite and pentlandite at high temperatures, there may have been localized sections with high enough sulfur content for pyrite to form while preventing the generation of pentlandite (Dare et al. 2011). Contrary to previous findings on stockwork sulfides (Fröhlich 2016), the pyrite in the disseminated mineralization seems to not carry cobalt.

From the six samples analysed with FE-SEM-EDS, 27 platinum group mineral grains were found, of which 100 % are tellurides, 73 % belong to the merenskyite-moncheite-melonite solid solution, 23 % are michenerite and 4 % sopcheite. These observations are in line with the PGM speciation noted by Ahvenjärvi (2015) in the massive sulfide ore and Fröhlich (2016) in the stockwork sulfide ore. This re-asserts the homogeneity of the PGM mineralogy in the Sakatti deposit.

The PGM speciation in Sakatti dissemination seems to be similar to the one found in the ultramafic Ni-Cu-PGE Kevitsa deposit (Kiuttu et al. 2010) (Figure 37a,b). The disseminated ore in Kevitsa is dominated by melonite (51 %), followed by merenskyite-moncheite solid solution (26 %), michenerite (13 %) and sperrylite (10 %). Sperrylite has not been observed in Sakatti, which fits with the general low content in As of the deposit (Brownscombe 2015, Fröhlich 2015). The overall predominance of telluride platinum group minerals seems to also be found in other deposits within the Central Lapland Greenstone Belt such as the gold deposit of Mustajärvi (Nykänen and Ojala, 2007). This could point to a regional enrichment in Tellurium of the Central Lapland Greenstone Belt.

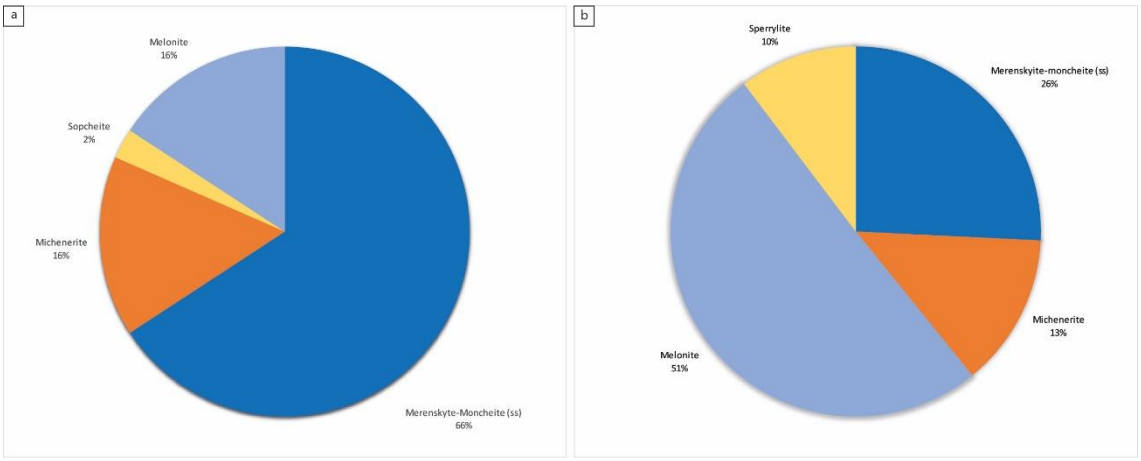

Figure 37. (a) Diagram representing the general PGMs abundancies in Sakatti disseminated ore. (b) Diagram representing the general PGMs abundancies of the Kevitsa deposit, Modified after Kaukonen (2010).

Some PGMs from the merenskyite-moncheite-melonite series (Figure 22) have shown euhedral shapes and in association with chalcopyrite, which makes it plausible to think that they formed in later stages of the crystallization of ISS.

Baddeleyite crystal, 60 by 40 micron was found in the disseminated sample TS41 from the NE-body. U-Pb dating of this mineral may be possible.

The histograms based on the collected X-ray computed tomography data reveal that the section with the largest amount of grains occurs before the described spikes and is characterized by lower X-ray attenuation values (Figures 25, 27, 29). Considering the general mineralogy observed and the density of the sulfides (Table 8), it is suggested that these sections belong to the chalcopyrite. Thus, the consecutive spikes may represent other sulfide or oxide phases with even higher density than the chalcopyrite, such as pyrrhotite, pentlandite, chromite, etc.

4.2. Chemical composition of the disseminated and massive ores.

The disseminated mineralization in the spidergram where all the Sakatti ores are plotted (Figure 32) has been divided into two sections. From Ni to Rh the disseminated ore shows

similar values to the massive ores. From Pt to Cu the trend becomes more similar to the stockwork ore.

Based on Ni/Cu and Pd/Ir ratios (Figure 33a), the Main body massive sulfides (Ahvenjärvi 2015) can be broadly divided into two groups. One with Ni/Cu values above 0.5, which fits the typical values of a layered intrusion and high MgO basalt deposits. The other one with Ni/Cu values below 0.5, with which the disseminated dataset matches, and which does not clearly plot at any standard deposit compositional ratio range. This seems to suggest a compositional link between massive and disseminated sulfides. At Cu/Ir and Ni/Pd diagram (Figure 33b), the disseminated dataset presents Cu/Ir values within the range of the massive ores, however, the Ni/Pd values establish a distinctive trend from the massive and stockwork sulfides. The disseminated ore has a lower Cu/Ir ratio than the stockwork mineralization due to the remarkably low Ir content in the latter. This may indicate that the disseminated samples are formed by a mixture of MSS and ISS.

The Ni vs Cu diagram (Figure 34a) reaffirms that the whole disseminated ore dataset has a Ni content within the range of the values for the massive ore while having fairly constant Cu values that are slightly lower than the ones from stockwork vein ore. The progressive increase of the Cu content in the massive samples and the decrease in Ni abundance in the stockwork sulfides seem to indicate compositional evolution during the crystallization of the system. The Ir vs Pd diagram (Figure 34b) shows that the disseminated ore has distinctive values that separate it from the massive and stockwork ores. With Ir values in the range of the bulk of massive sulfide samples and Pd values similar to the stockwork ore.

A further comparison of the disseminated Cu-rich ore in Sakatti with disseminated mineralizations of other Ni-Cu-PGE deposits (Barnes and Lightfoot, 2005) was done with the help of a spidergram (Figure 32b). Of all the deposits presented here, the disseminated sulfides from Oktabr'sky, Noril'sk-Talnakh seem to have a trend closest to that of the disseminated Sakatti ore. A possible explanation of the similarities of the Sakatti and Oktabr'sky disseminated ores could be the in-situ crystallization of the MSS and ISS, with no migration of ISS away from the MSS.

Additionally, Sakatti disseminated ore shows an average Ni/Cu ratio of 0.17 which is significantly lower than the 0.60 ratio of the Kevitsa disseminated mineralization. The Ni/Pd average ratio in Sakatti is 5320, compared to 19801 in Kevitsa. This indicates that the Ni content in proportion to the Cu and Pd content is higher in the disseminated ore of Kevitsa than in that of Sakatti.

The massive ore from the NE and SW bodies showed a chemical signature almost identical to that of the massive sulfides in the Main body. Therefore, it can be assumed that they are intrinsically related and share a common genesis.

4.3. Fractionation of sulfide liquid during the formation of Sakatti Ni-Cu-(PGE) ore

From the mineralogical point of view, the disseminated ore is widely dominated by chalcopyrite, which is reflected in its geochemical composition. This left the question of how this ore relates to the massive sulfides and stockwork vein sulfides that were classified as the MSS and ISS of the Sakatti deposit respectively (Ahvenjärvi 2015, Fröhlich 2016).

There seems to be a consensus that the ISS got separated from the MSS during the crystallization process (Fröhlich 2016). This is reflected in diagrams like Rh vs Rh/Cu (Figure 36) and their geochemical trends in the spider diagrams (Figure 32a,b). Consequently, as the crystallization progresses, fractionation will lead to the massive ore becoming more enriched in Ni, Co, Os, Ir, Ru and Rh and the stockwork mineralization becoming more depleted in these elements and have higher contents of Pt, Pd, Au and Cu. The disseminated mineralization shares similar enrichments as the massive and stockwork sulfides. This, has led to think that there has not been a separation of the ISS from the MSS during the crystallization process of the disseminated ore.

Nickel is compatible with the MSS throughout the whole crystallization process, and Ir is significantly compatible when MSS is forming. Copper gets enriched in the residual melt until ISS starts crystallizing, while Pd continues to be incompatible and keeps

accumulating in the residual melt. Thus, as the fractionation of the system occurs during crystallization, it is expected that a progressive decrease in the Ni/Cu and Ni/Pd ratios occurs and an increase in the Pd/Ir and Cu/Ir ratios. These evolution trends are reflected by the massive sulfides and stockwork vein ores in the Ni/Cu vs Pd/Ir and Cu/Ir vs Ni/Pd diagrams (Figure 33). In the Ni/Cu vs Pd/Ir diagram, the disseminated ore falls within the area of the most evolved massive samples. In the Cu/Ir vs Ni/Pd diagram, the disseminated mineralization exhibits a similar evolution pattern to that of the stockwork vein ore, but the Ni/Pd ratios stay higher and the overall Cu/Ir is lower. This again could be explained by in-situ crystallization of the MSS and ISS.

Considering that Se is incompatible with MSS and that the sulfur content is directly proportionate to the abundance of sulfide minerals, the massive sulfides are expected to have the highest S/Se ratio and the lowest R-factor. On the other hand, Pt and Pd are incompatible during the whole crystallization process and Se becomes moderately compatible with ISS, so the amounts of these elements will increase as the system evolves. If the concentration of sulfide minerals in relation to silicates decreases, like in the case of the stockwork or disseminated ores, the R-factor will increase. This can be observed in the S/Se vs $(Pt+Pd)_{100\%\ S}$ diagram (Figure 35). According to this diagram, the disseminated ore seems to be significantly fractionated, which fits previous observations, but in this case, the disseminated ore samples all plot as ISS. This could be explained by the low sulfur content of the disseminated ore and the in-situ crystallization of MSS and ISS, which translates to higher Pt, Pd and Se contents than in the massive sulfides. Additionally, the S/Se vs $(Pt+Pd)_{100\%\ S}$ diagram also presents a geochemical dataset from the Oktyabr`sk, Noril'sk-Talnakh, deposit and another one from the McCreedy East deposit (Czamanske et al. 1992, Dare et al. 2011, 2014). The Oktyabr`sk deposit presents a fractionation trend very similar to that of the Sakatti deposit, but, differing in the S/Se and $(Pt+Pd)_{100\%\ S}$, especially the latter. The McCreedy East deposit shows fairly close values and trend to the Sakatti deposit. This suggests a higher similarity between the McCreedy East and Sakatti deposits.

Finally, the Rh vs Rh/Cu diagram (Naldrett et al. 1999) has been used to specifically track the fractionation of a Ni-Cu-PGE magmatic deposit. The disseminated ore samples plot within the most fractionated section of the MSS path line. It seems to start from

compositions similar to the massive sulfides and evolves until the beginning of the formation of ISS. Consequently, this path could fit the evolution of a disseminated ore with no separation of ISS from MSS, leading to compositions that indicate a degree of fractionation in between the massive and stockwork vein ores.

4.4. Effect of post-cumulus processes on the disseminated ore

Even though primary textures and mineralogy are preserved, alteration seems to be widely spread throughout the disseminated samples. This is supported by the S/Se vs $(Pt+Pd)_{100\%\ S}$ diagram (Figure 35), where the Sakatti ore samples plot away from the fractionation line, towards the metamorphism, hydrothermalism and serpentinization area.

Marcasite occurs as the alteration product of pyrrhotite with a pseudomorphic tendency. This alteration has also been observed by Fröhlich (2016). Marcasite could also be present in the massive sulfides and has been categorized as secondary pyrite linked to pyrrhotite (Ahvenjärvi 2015). In many cases, the differentiation between marcasite and pyrite is difficult as they are polymorphs with similar optical properties; however, marcasite has strong anisotropism which was observed in the disseminated sulfides. Pyrrhotite alteration to marcasite or pyrite can be linked to serpentinization but also to hydrothermal conditions with low pH or S(-II) deficient solutions (saturation index << 1000) for marcasite and a saturation index > 1000 for pyrite and temperatures up to 220 ºC (Qian et al. 2011). A deposit zonation has been observed within the disseminated ore, where marcasite becomes more abundant towards the south-east in shallower parts of the Main body, whereas fresh pyrrhotite content seems to decrease (Figure 18). The NE body does not show any conclusive distribution of pyrrhotite and marcasite. The zonation of the marcasite in the Main body may be explained by the higher exposition of shallower sections of the deposit to percolating waters. Considering the high degree of serpentinization affecting the whole deposit, seems likely that this process triggered the formation of marcasite. Nevertheless, the fact that magnetite appears replacing marcasite in some cases could imply the existence of another alteration event.

Pentlandite has been locally altered to violarite and millerite in a pseudomorphic way. Violarite can form by exsolution during the cooling of pentlandite or, more commonly, by oxidation of pentlandite in a supergene zone (Hui et al. 2004). Millerite is known to form in connection with serpentinization, oxidation zones, carbonate veins and sedimentary rocks linked to coals (Pracejus 2015). Millerite has also been observed to partially replace chalcopyrite and in association with bornite. Overall abundance of violarite and millerite increases towards shallower sections within the Main body, being almost absent in the deeper parts towards the north-west (Figure 20). Pentlandite, violarite and millerite can be found in the NE body, with an apparent higher degree of alteration in hole 12MOS8082. Considering the high degree of serpentinization it is suggested that millerite formed due to this alteration process.

The presence of isocubanite could imply that the Sakatti system suffered an increase in temperature and/or pressure after crystallization, such as regional metamorphism, causing the alteration of cubanite to isocubanite (Nenasheva and Kravchenko, 2015).

Bornite and covellite have been found only in four samples, which are approximately aligned in a dip direction that fits with the SE-NW faults 1 and 2 (Figure 21). Combined with the fact that bornite and covellite are a common product of chalcopyrite alteration in supergene environments, this has given rise to the idea of a supergene origin for these phases. Supergene alterations may also trigger the formation of violarite.

A certain degree of remobilization was observed related to PGE. Palladium and to a lesser degree platinum seem to have been leached from the merenskyite-moncheite minerals, whereas Pb and Ag have been incorporated, giving rise to minerals like altaite and hessite (Figure 23, Table 7). The transport of PGE typically occurs as chloride complexes in oxidizing and/or acidic fluids at relatively low temperatures (< 300 ºC) (Fröhlich 2016, Holwell et al. 2017). Nevertheless, the degree of remobilization of Pd and Pt seem to have been low.

The pervasive transformation of silicate into serpentine minerals in addition to the extensive magnetite replacement of minerals like pyrrhotite, marcasite, chalcopyrite, etc. points to serpentinization as the main alteration process that affected this deposit.

Metamorphism may have played an important role in alteration of the Sakatti deposit. The geological formations hosting Sakatti reached temperatures ranging from 400 to 700 ºC and greenschist to amphibolite facies (Philpotts 1989, Tyrväinen 1983). Marcasite may have developed due to a hydrothermal event with low pH or S(-II)-deficient solutions (saturation index << 1000) and temperatures up to 220 ºC (Qian et al. 2011). This fluid could also have caused the minor remobilization of Pd and Pt from the PGM (Holwell et al. 2017, Wood 2002).

4.5. Model for the origin of disseminated ore and its relationship to other ore types of Sakatti

Considering the mineralogy, composition and fractionation, it is suggested that the disseminated ore originated from the same sulfide pool as the massive and stockwork mineralizations but followed a different fractionation path. Based on this, the following tentative genetic model for the disseminated ore is proposed:

After the sulfur saturation of the primary magma occurred, the exsolution of the sulfide melt droplets from the silicate melt was triggered. This lead the chalcophile elements to preferably partition into the immiscible sulfide melt. The transport of the sulfide droplets is controlled by the interaction of the properties of the magmatic flow and gravity. Consequently, a reduction in the force of the magmatic flow could mean that the transport of the sulfide blebs would start to be predominantly controlled by gravity. The preponderance of gravity would allow more efficient percolation, which would simultaneously be reinforced by the coalescence of the sulfide droplets. Ultimately, this could lead to the concentration of the sulfide melt into an area of the system (e.g. faulted section), giving rise to the formation of massive sulfide lenses (Barnes et al. 2017, Naldrett 1973). During crystallization of these massive lenses, separation and even migration of the ISS away from the MSS can occur, leading to the formation of the stockwork ore (Barnes and Lightfoot, 2005). This is an outline of the current hypothesis for the genesis of the massive and stockwork vein ores of the Sakatti deposit. For further details, refer to the studies done by Ahvenjärvi (2015), Fröhlich (2016) and Brownscombe (2013, 2015).

Nevertheless, the disseminated ore seem to have had distinct origin. It is suggested that the disseminated ore was formed as a result of the crystallization of sulfide droplets that did not percolate and instead stayed in the intercumulus phase of the silicates. The crystallization of ISS occurred in situ with the MSS, with no physical separation between these two phases. This would explain the compositional similarities of the disseminated ore with the massive sulfides and the distinct fractionation path that separates it from the stockwork and massive mineralizations. Consequently, it is presumed that the disseminated ore would occur as a cloud surrounding the massive ore and ending below the last massive sulfide lens. Moreover, it is expected the injection into the disseminated ore cloud by the later formed stockwork mineralization. This seems to have been observed in the Main body of the Sakatti deposit. Additionally, the used modelling technique and chosen cut off allowed to distinguish another two disseminated ore zones within the Main body, above and below the major cloud of disseminated ore (Figure 7). No noticeable geochemical differences have been observed between these three disseminated zones. Thus, one possibility could be that these disseminated zones formed by magmatic pulses from the same source. Brittle deformation through faults could also have separated the upper and lower disseminated zones from the main intermediate cloud. The lower dissemination lens may also be indicative of the presence of deeper mineralizations yet to be found.

5. CONCLUDING REMARKS

The disseminated ore has predominant patchy texture with low connectivity and high wettability, which could be attributed to percolation of the sulfides (Barnes et al. 2017). The main primary sulfide phases are chalcopyrite, pyrrhotite and pentlandite. Chalcopyrite forms intergrowths into the pyrrhotite and pentlandite crystals which denotes it´s later stage formation and sulfide migration. The metastable existence of NC pyrrhotite inclusions in the predominantly 4C pyrrhotite may indicate of variations in Fe atomic percentage during crystallization. Primary euhedral pyrite could imply locally elevated sulfur content within the sulfide melt. Cobalt is mainly hosted in pentlandite due to its partitioning into the MSS. The presence of cubanite may imply slow cooling after the metamorphic peak of the system while nickeloan pyrrhotite could still be evidence of

a quick cooling during the crystallization of the magma. All found PGMs are tellurides and bismuth-telluride phases, merenskiyite-moncheite-melonite series minerals being the most abundant.

The disseminated, stockwork and massive ores had the same or very similar melt origin, but their sulfides followed a distinct crystallization paths. Chemical composition of disseminated ore shows certain similarities with the massive sulfides and stockwork mineralization but has followed a different evolution path. The content in Ni, Co, IPGE and Rh are remarkably similar between the disseminated and massive sulfides. Pt, Pd, Au and Cu in the disseminated ore show a trend more alike to the stockwork ore, however, element content have less in common. The disseminated ore low degree of percolation led to the separation from the main sulfide melt pool that later gave origin to the massive and stockwork ores. Thus, the disseminated ore formed in conditions with larger R-factor than the massive and stockwork ores. The massive and stockwork sulfides got relatively isolated from the silicate phases, however, during their formation they kept reacting and re-equilibrating with the residual sulfide melt. The massive sulfides from the NE and SW bodies shows almost identical element distribution as the massive ore in the Main body (Ahvenjärvi 2015), therefore, it is assumed that they have followed the same type of genesis.

The fractionation of the disseminated ore represents a distinctive path that separate it from the massive and stockwork ores. Moreover, the fractionation path of the disseminated sulfides suggests that ISS did not migrate away from the MSS unlike in the case of the formation of the stockwork ore (Ahvenjärvi 2015, Fröhlich 2016).

The disseminated ore show a widespread alteration with different degrees of intensity. Overall, serpentinization seems to be the most pervasive process which is in line with previous studies (Ahvenjärvi 2015, Brownscombe 2015, Fröhlich 2016). The presence of marcasite and the observed remobilization of Pd and Pt away from the PGMs may point to a hydrothermal event with low pH or S(-II) deficient solutions (saturation index << 1000) and temperatures up to 220 ºC (Qian et al. 2011). This is supported by the long metamorphic record of the Central Lapland Greenstone Belt which reached greenschist to amphibolite facies (Philpotts 1989, Tyrväinen 1983). The presence of bornite and

covellite seem to imply that supergene weathering affected Sakatti sulfides at shallow levels, which could also explain the formation of millerite, violarite and may have caused some remobilization of other sulfide phases as well.

6. AKNOWLEDGMENTS

First and foremost, this project would have not been possible without the involvement of the team at Anglo American Sakatti and my supervisor Dr. Petri Peltonen. For this reason, I am profoundly grateful.

On the university side, Dr. Petri Peltonen´s advice and deep knowledge on the matter guided me through the development and conclusion of this project. Moreover, I would like to give special appreciation to the fact that Dr. Peltonen has always been available whenever I had any problems or questions. Furthermore, I have in high appreciation all the university staff and professors that enabled my progress with this project, such as Radoslaw M. Michallik and Aku Heinonen.

On the side of Anglo American Sakatti, I want to thank Outi Ahvenjärvi for acting as a link with the company and for providing me with all the information I needed. Also I want to recognize Janne Siikaluoma for his concise advises that helped me overcome certain obstacles along the way, especially during the selection of my samples. Furthermore, I want to show my appreciation to Jukka Jokela who ultimately made this project happen by approving the proposal and funding for it. I want to also thank Annukka Torvinen for coordinating and supervising that the chemical analysis of my samples were done properly. Finally, a big thank you the rest of the team of geologists and also to the technicians who assisted me during the whole process of sample selection.

I would also like to give a mention to the staff working at GTK. In particular, to Johanson Bo and Jukka Kuva for guiding me through the whole analysis process of my samples and sharing with me their deep knowledge on the subject.

Ultimately, to all my family and friends that have given me support and advise, you have been a cornerstone on this enterprise, thank you.

7. REFERENCES

Ahvenjärvi, O. (2015) Sulfide and platinum group mineralogy of massive sulfide ore in the Sakatti Cu-Ni-PGE deposit. Master thesis University of Oulu.

Anglo American ltd. 2017. Building on firm foundations delivering a sustainable future. Anglo American ltd., annual report.

Anglo American ltd. 2019. Re-imagining mining to improve people. Anglo American ltd., annual report.

Barnes, S.-J., Cox, R. A. & Zientek, M. L. (2006) Platinum-group element, Gold, Silver and Base Metal distribution in compositionally zoned sulfide droplets from the Medvezky Creek Mine, Noril'sk, Russia. Contributions to Mineralogy and Petrology, 152(2), 187-200.

Barnes, S.-J. & Lightfoot, P. C. (2005) Formation of magmatic nickel-sulfide ore deposits and processses affecting their copper and platinum-group element contents. Economic Geology 100th Anniversary, 179-213.

Barnes, S.-J., Melezhik, V. A. & Sokolov, S. V. (2001) The composition and mode of formation of the Pechenga nickel deposits, Kola Peninsula, northwestern Russia. The Canadian Mineralogist, 39(2), 447-471.

Barnes, S.-J., Naldrett, A. & Gorton, M. (1985) The origin of the fractionation of platinum-group elements in terrestrial magmas. Chemical geology, 53(3-4), 303-323.

Barnes, S.-J., Zientek, M. L. & Severson, M. J. (1997) Ni, Cu, Au, and platinum-group element contents of sulphides associated with intraplate magmatism: a synthesis. Canadian Journal of Earth Sciences, 34(4), 337-351.

Barnes, S. J., Mungall, J. E., Le Vaillant, M., Godel, B., Lesher, C. M., Holwell, D., Lightfoot, P. C., Krivolutskaya, N. & Wei, B. (2017) Sulfide-silicate textures in magmatic Ni-Cu-PGE sulfide ore deposits: Disseminated and net-textured ores. American Mineralogist, 102(3), 473-506.

Becker, M., de Villiers, J. & Bradshaw, D. (2010) The Mineralogy and Crystallography of Pyrrhotite from Selected Nickel and PGE Ore Deposits. Economic Geology, 105(5), 1025-1037.

Bertaut, E. (1953) Contribution a l'etude des structures lacunaires: la pyrrhotine. Acta Crystallographica, 6(6), 557-561.

Brownscombe, W., Herrington, R. & Wilkinson, J. (2013) Geochemistry of the Sakatti magmatic Cu-Ni-PGE deposit, northern Finland, Proceedings of the 12th Biennial SGA Meeting on Mineral Deposit Research for a High-Tech World, August.

Brownscombe, W., Ihlenfeld, C., Coppard, J., Hartshorne, C., Klatt, S., Siikaluoma, J. K. & Herrington, R. J. (2015) Chapter 3.7 - The Sakatti Cu-Ni-PGE Sulfide Deposit in Northern Finland A2 - Maier, Wolfgang D, in Lahtinen, R. & O'Brien, H. (eds), Mineral Deposits of FinlandElsevier, 211-252.

CABRI, L. (1981) The platinum-group minerals.

Cawthorn, R. G. & Meyer, F. M. (1993) Petrochemistry of the Okiep copper district basic intrusive bodies, northwestern Cape Province, South Africa. Economic Geology, 88(3), 590-605.

Chai, G. & Naldrett, A. J. (1992) Characteristics of Ni-Cu-PGE mineralization and genesis of the Jinchuan deposit, northwest China. Economic Geology, 87(6), 1475-1495.

Coppard, J. (2014) Discovery history of the Sakatti Cu-Ni-PGE deposit, Finland.

Craig, J. R. (1973) Pyrite-pentlandite assemblages and other low temperature relations in the Fe-Ni-S system. American Journal of Science, 273(A), 496-510.

Croghan, W. & Egeghy, P. P. (2003) Methods of Dealing with Values Below the Limit of Detection using SAS Carry.

Czamanske, G. K., Kunilov, V. E., Zientek, M. L., Cabri, L. J., Likhachev, A. P., Calk, L. C. & Oscarson, R. L. (1992) A proton microprobe study of magmatic sulfide ores from the Noril'sk-Talnakh District, Siberia. The Canadian Mineralogist, 30(2), 249-287.

Dare, S. A., Barnes, S.-J., Prichard, H. M. & Fisher, P. C. (2011) Chalcophile and platinum-group element (PGE) concentrations in the sulfide minerals from the McCreedy East deposit, Sudbury, Canada, and the origin of PGE in pyrite. Mineralium Deposita, 46(4), 381-407.

Dare, S. A., Barnes, S.-J., Prichard, H. M. & Fisher, P. C. (2014) Mineralogy and geochemistry of Cu-rich ores from the McCreedy East Ni-Cu-PGE deposit (Sudbury, Canada): implications for the behavior of platinum group and chalcophile elements at the end of crystallization of a sulfide liquid. Economic Geology, 109(2), 343-366.

De Waal, S. A., Xu, Z., Li, C. & Mouri, H. (2004) Emplacement of viscous mushes in the Jinchuan ultramafic intrusion, western China. The Canadian Mineralogist, 42(2), 371-392.

Distler, V. (1994) Platinum mineralisation of the Noril'sk deposits: Ontario Geological Survey Special Publication 5.

Ebel, D. & Naldrett, A. (1996a) Experimental fractional crystallization of Cu-and Ni-bearing Fe sulfide liquids. Economic Geology, 91, 607-621.

Ebel, D. & Naldrett, A. (1997) Crystallization of sulfide liquids and the interpretation of ore composition. Canadian Journal of Earth Sciences, 34(4), 352-365.

Ebel, D. S. & Naldrett, A. J. (1996b) Fractional crystallization of sulfide ore liquids at high temperature. Economic Geology, 91(3), 607-621.

Eckstrand, O. & Hulbert, L. (1987) Selenium and the source of sulfur in magmatic nickel and platinum deposits [abs.], Geological Association of Canada-Mineralogical Association Canada Program with Abstracts.

Fassel, V. A. & Kniseley, R. N. (1974) Inductively coupled plasma. Optical emission spectroscopy. Analytical Chemistry, 46(13), 1110A-1120a.

Fleet, M. E., Chryssoulis, S. L., Stone, W. E. & Weisener, C. G. (1993) Partitioning of platinum-group elements and Au in the Fe− Ni− Cu− S system: Experiments on the fractional crystallization of sulfide melt. Contributions to Mineralogy and Petrology, 115(1), 36-44.

Fleet, M. E. & Pan, Y. (1994) Fractional crystallization of anhydrous sulfide liquid in the system Fe-Ni-Cu-S, with application to magmatic sulfide deposits. Geochimica et Cosmochimica Acta, 58(16), 3369-3377.

Francis, C. A. & Craig, J. R. (1976) Pyrrhotite; the nA (or 2A, 3C) superstructure reviewed. American Mineralogist, 61(1-2), 21-25.

Fröhlich, F. (2016) Sulfide Vein Mineralization of the Shallow Eastern Stockwork Zone and its Genetic Relation to the Massive Sulfide Mineralization at the Sakatti Cu-Ni-PGE Deposit, Finland. Master thesis Technische Universität Bergakademie Freiberg. Available online: https://www.myendnoteweb.com/EndNoteWeb.html?func=downloadInstallers&cat=download& [Accessed.

Godel, B., Barnes, S.-J. & Maier, W. D. (2006) 3-D distribution of sulphide minerals in the Merensky Reef (Bushveld Complex, South Africa) and the JM Reef (Stillwater Complex, USA) and their relationship to microstructures using X-ray computed tomography. Journal of Petrology, 47(9), 1853-1872.

Halkoaho, T. (2014) Petrology of the Sakatti Ni-Cu-PGE deposit, Sodankylä, Finland.

Hanski, E. & Huhma, H. (2005) Central Lapland greenstone belt, Developments in Precambrian GeologyElsevier, 139-193.

Hawley, J. (1965) Upside-down zoning at frood, Sudbury, Ontario. Economic Geology, 60(3), 529-575.

Herzberg, C. (1992) Depth and degree of melting of komatiites. Journal of Geophysical Research: Solid Earth, 97(B4), 4521-4540.

Hoffman El (2002) Sample Preparation and Bulk Analytical Methods for PGE. In: Cabri LJ (ed) The Geology, Geochemistry, Mineralogy and Mineral Beneficiation of Platinum-Group Elements: CIM Special Volume, pp 1–11

Holwell, D., Adeyemi, Z., Ward, L., Smith, D., Graham, S., McDonald, I. & Smith, J. (2017) Low temperature alteration of magmatic Ni-Cu-PGE sulfides as a source for hydrothermal Ni and PGE ores: A quantitative approach using automated mineralogy. Ore Geology Reviews.

Holwell, D. A. & McDonald, I. (2006) Petrology, geochemistry and the mechanisms determining the distribution of platinum-group element and base metal sulphide mineralisation in the

Platreef at Overysel, northern Bushveld Complex, South Africa. Mineralium Deposita, 41(6), 575.

Hui, W. Y., Tenailleau, C., Pring, A. & Brugger, J. (2004) Experimental study of the transformation of pentlandite/pyrrhotite to violarite, Regolith. Citeseer.

Ihlenfeld C & Collis K (2014) QA/QC Report (2006-14): Sakatti Exploration Project. Anglo American Company Internal Document

Impala, G. (2017) 2017 GEOLOGY & MINERALISATION 3D MODEL UPDATE, SAKATTI PROJECT, FINLAND.

Keays, R. R. (1995) The role of komatiitic and picritic magmatism and S-saturation in the formation of ore deposits. Lithos, 34(1-3), 1-18.

Keays, R. R. & Crocket, J. H. (1970) A study of precious metals in the Sudbury nickel irruptive ores. Economic Geology, 65(4), 438-450.

Kiuttu, J., Ruuska, J. & Yliniemi, L. Advanced and sustainable beneficiation of platinum group metals (PGM) in sulphide poor platinum (PGE) deposits–BEGBE. Final Report. May 2010.

Lehtinen, M., Nurmi, P. A. & Ramo, O. (2005) Precambrian Geology of FinlandElsevier.

Lehtonen, M. (1998) Kittilän vihreäkivialueen geologia: Lapin vulkaniittiprojektin raportti, 140Geologian tutkimuskeskus.

Li, C., Barnes, S.-J., Makovicky, E., Rose-Hansen, J. & Makovicky, M. (1996) Partitioning of Ni, Cu, Ir, Rh, Pt and Pd between monosulfide solid solution and sulfide liquid: effects of composition and temperature. Geochimica et Cosmochimica Acta, 60(7), 1231-1238.

Li, C., Naldrett, A. J., Coats, C. & Johannessen, P. (1992) Platinum, palladium, gold, copper-rich stringers at the Strathcona Mine, Sudbury; their enrichment by fractionation of a sulfide liquid. Economic Geology, 87(6), 1584-1598.

Lightfoot, P. C. & Evans-Lamswood, D. (2015) Structural controls on the primary distribution of mafic–ultramafic intrusions containing Ni–Cu–Co–(PGE) sulfide mineralization in the roots of large igneous provinces. Ore Geology Reviews, 64, 354-386.

Liu, Y. & Brenan, J. M. (2015) Partitioning of platinum-group elements (PGE) and chalcogens (Se, Te, As, Sb, Bi) between monosulfide-solid solution (MSS), intermediate solid solution (ISS) and sulfide liquid at controlled fO2–fS2 conditions. Geochimia et cosmochimica Acta, 159.

Lorand, J. (1993) Comment on'Content and isotopic composition of sulphur in ultramafic xenoliths from central Asia'by DA Ionov, J. Hoefs, KH Wedepohl and U. Wiechert. Earth and planetary science letters, 119, 627-634.

MacLean, W. H. (1969) Liquidus phase relations in the FeS-FeO-Fe 3 O 4-SiO 2 system, and their application in geology. Economic geology, 64(8), 865-884.

Maier, W. D., Lahtinen, R. & O'Brien, H. (2015) Mineral deposits of FinlandElsevier.

Makovicky, E. (2002) Ternary and quaternary phase systems with PGE, Geology, Geochemistry, Mineralogy and Mineral Beneficiation of Platinum-group ElementsCanadian Institute of Mining, Metallurgy and Petroleum, 131-175.

Mavrogenes, J. A. & O'Neill, H. S. C. (1999) The relative effects of pressure, temperature and oxygen fugacity on the solubility of sulfide in mafic magmas. Geochimica et Cosmochimica Acta, 63(7-8), 1173-1180.

McDonough, W. & Sun, S. s. (1995) The composition of the Earth. Chemical Geology, 120, 223-253.

Mungall, J. E. & Naldrett, A. J. (2008) Ore deposits of the platinum-group elements. Elements, 4(4), 253-258.

Mutanen, T. & Huhma, H. (2003) The 3.5 Ga Siurua trondhjemite gneiss in the Archaean Pudasjarvi granulite belt, northern Finland. BULLETIN-GEOLOGICAL SOCIETY OF FINLAND, 75(1/2), 51-68.

Naldrett, A. (1973) Nickel sulfide deposits-their classification and genesis, with special emphasis on deposits of volcanic association. CIM BULLETIN, 66(739), 45-63.

Naldrett, A., Asif, M., Gorbachev, N., Kunilov, V., Fedorenko, V. & Lightfoot, P. (1994a) The composition of the Ni-Cu ores of the Noril'sk region. Ontario Geological Survey, 357-372.

Naldrett, A., Asif, M., Scandl, E., Searcy, T., Morrison, G., Binney, W. & Moore, C. (1999) Platinum-group elements in the Sudbury ores; significance with respect to the origin of different ore zones and to the exploration for footwall orebodies. Economic Geology, 94(2), 185-210.

Naldrett, A., Asif, M., Scoates, R., Eckstrand, O. & Schwann, P. (1994b) Platinum-group elements in Fox River Sill, Manitoba, Canada: implications with respect to influxes of fresh magma and exploration for PGE deposits. Transactions of the Institution of Mining and Metallurgy. Section B. Applied earth science, 101, 10-21.

Naldrett, A., Craig, J. & Kullerud, G. (1967) The central portion of the Fe-Ni-S system and its bearing on pentlandite exsolution in iron-nickel sulfide ores. Economic Geology, 62(6), 826-847.

Naldrett, A. & Duke, J. (1980) Platinum metals magmatic sulfide ores. Science, 208(4451), 1417-1424.

Naldrett, A., Pessaran, A., Asif, M. & Li, C. (1994c) Compositional variation in the Sudbury ores and prediction of the proximity of footwall copper-PGE orebodies, Proceedings, Sudbury-Noril'sk Symposium. Edited by PC Lightfoot and AJ Naldrett. Ontario Geological Survey, Special.

Naldrett, A. J. (2013) Magmatic sulfide deposits: Geology, geochemistry and explorationSpringer Science & Business Media.

Naldrett, A. J., Innes, D., Sowa, J. & Gorton, M. (1982) Compositional variations within and between five Sudbury ore deposits. Economic Geology, 77(6), 1519-1534.

Naldrett, A. J., Li, C. & Ripley, E. M. (2011) Fundamentals of Magmatic Sulfide Deposits, Magmatic Ni-Cu and PGE Deposits: Geology, Geochemistry, and GenesisSociety of Economic Geologists, 0.

Nenasheva, S. & Kravchenko, T. (2015) Composition features of isocubanite and polymorphous modifications of CuFe 2 S 3 compound. Geology of Ore Deposits, 57(7), 626-633.

Nykänen, V. & Ojala, V. J. (2007) Spatial analysis techniques as successful mineral-potential mapping tools for orogenic gold deposits in the northern Fennoscandian Shield, Finland. Natural Resources Research, 16(2), 85-92.

Paktunc, A. D., Hulbert, L. J. & Harris, D. C. (1990) Partitioning of the platinum-group and other trace elements in sulfides from the Bushveld Complex and Canadian occurrences of nickel-copper sulfides. The Canadian Mineralogist, 28(3), 475-488.

Philpotts, A. R. (1989) Petrography of igneous and metamorphic rocksPearson College Div.

Pracejus, B. (2015) The ore minerals under the microscope: an optical guideElsevier.

Pósfai, M., Sharp, T. & Kontny, A. (2000) Pyrrhotite varieties from the 9.1 km deep borehole of the KTB project. American Mineralogist, 85, 1406-1415.

Qian, G., Xia, F., Brugger, J., Skinner, W. M., Bei, J., Chen, G. & Pring, A. (2011) Replacement of pyrrhotite by pyrite and marcasite under hydrothermal conditions up to 220 C: An experimental study of reaction textures and mechanisms. American Mineralogist, 96(11-12), 1878-1893.

Queffurus, M. & Barnes, S.-J. (2015) A review of sulfur to selenium ratios in magmatic nickel–copper and platinum-group element deposits. Ore Geology Reviews, 69, 301-324.

Rastas, P., Huhma, H., Hanski, E., Lehtonen, M., Harkonen, I., Kortelainen, V., Manttari, I. & Paakkola, J. (2001) U-Pb isotopic studies on the Kittila greenstone area, central Lapland, Finland. SPECIAL PAPER-GEOLOGICAL SURVEY OF FINLAND, 95-142.

Robert RVD, Palmer R & Van Wyk e (1971) Concentration of the noble metals by a fire-assay technique using nickel sulphide as the collector. Report NIM, .1371. National Institute for Metallurgy, Johannesburg

Rollinson, H. R. (2014) Using geochemical data: evaluation, presentation, interpretationRoutledge. Economic Geology 96, 145-147.

Rose, A. L. & Brenan, M. J. (2001) Wetting Properties of Fe-Ni-Co-Cu-O-S Melts against Olivine: Implications for Sulfide Melt Mobility.

Simonen, A. (1971) Das finnische Grundgebirge. Geologische Rundschau, 60(4), 1406-1421.

Smith, J. W., Holwell, D. A., McDonald, I. & Boyce, A. J. (2016) The application of S isotopes and S/Se ratios in determining ore-forming processes of magmatic Ni–Cu–PGE sulfide deposits: a cautionary case study from the northern Bushveld Complex. Ore Geology Reviews, 73, 148-174.

Tyrväinen, A. (1983) Sodankylän ja Sattasen kartta-alueiden kalliopeä [Summary: Pre-Quaternary rocks of the Sodankylä and Sattasvaaara map sheet area. Geological Map of Finland 1: 100 000, Explanation to the Maps of Rocks, Sheets 3713 and 3714]. Geol. Surv. Finland, Espoo (in Finnish, English summary).

Verbovšek, T. (2011) A comparison of parameters below the limit of detection in geochemical analyses by substitution methods = Primerjava ocenitev parametrov pod mejo določljivosti pri geokemičnih analizah z metodo nadomeščanja. RMZ - Materials and Geoenvironment, 58, 393-404.

Vokes, F. (1969) A review of the metamorphism of sulphide deposits. Earth-Science Reviews, 5(2), 99-143.

Vuollo, J. & Huhma, H. (2005) Paleoproterozoic mafic dikes in NE Finland, Developments in Precambrian GeologyElsevier, 195-236.

Wang, H. & Salveson, I. (2005) A review on the mineral chemistry of the non-stoichiometric iron sulphide, $Fe_{1-x}S$ ($0 \leq x \leq 0.125$): polymorphs, phase relations and transitions, electronic and magnetic structures. Phase Transitions, 78(7-8), 547-567.

Weihed, P., Arndt, N., Billström, K., Duchesne, J.-C., Eilu, P., Martinsson, O., Papunen, H. & Lahtinen, R. (2005) 8: Precambrian geodynamics and ore formation: The Fennoscandian Shield. Ore Geology Reviews, 27(1-4), 273-322.

Wendlandt, R. F. (1982) Sulfide saturation of basalt and andesite melts at high pressures and temperatures. American Mineralogist, 67(9-10), 877-885.

Wood, S. (2002) The aqueous geochemistry of the platinum-group elements with applications to ore deposits. The geology, geochemistry, mineralogy and mineral beneficiation of platinum-group elements, 54, 211-249.

Zientek, M. L., Likhachev, A., Kunilov, V., Barnes, S.-J., Meier, A. L., Carlson, R., Briggs, P. H., Fries, T., Adrian, B. & Lightfoot, P. (1994) Cumulus processes and the composition of magmatic ore deposits: examples from the Talnakh district, Russia. Ont Geol Surv Spec Publ, 5, 373-392.